Winter 2005

Modeling and Simulation of Photonic Crystal Fibers and Distributed Feedback Photonic Crystal Fiber Lasers

Feng Wu
Old Dominion University

MODELING AND SIMULATION OF PHOTONIC CRYSTAL FIBERS AND DISTRIBUTED FEEDBACK PHOTONIC CRYSTAL FIBER LASERS

by

Feng Wu

B.S.E.E July 1993, Northern Jiaotong University

M.S.E.E. March 1996, Northern Jiaotong University

A Dissertation Submitted to the Faculty of

Old Dominion University in Partial Fulfillment of the

Requirements for the Degree of

DOCTOR OF PHILOSOPHY

ELECTRICAL ENGINEERING

OLD DOMINION UNIVERSITY

December 2005

Approved by:

Sacharia Albin (Director)

John B. Cooper (Member)

K. Vijayan Asari (Member)

Mounir Laroussi (Member)

ABSTRACT

MODELING AND SIMULATION OF PHOTONIC CRYSTAL FIBERS AND DISTRIBUTED FEEDBACK PHOTONIC CRYSTAL FIBER LASERS

Feng Wu

Old Dominion University, 2005

Director: Dr. Sacharia Albin

A photonic crystal fiber (PCF) is comprised of a solid or air core surrounded by periodically arranged air holes running along the length of the fiber, which guides light in a fundamentally new way compared to conventional optical fibers, affecting almost all areas of optics and photonics. To analyze the dispersion and loss properties of PCFs, a two-dimensional (2D) finite-difference frequency-domain (FDFD) method combined with the technique of perfectly matched layer (PML) is developed. The propagation constant and loss can be obtained with accuracies in the orders of $\sim 10^{-6}$ and $\sim 10^{-3}$, respectively.

The Bragg fiber is a kind of PCF with alternate layers surrounding a solid or air core. To improve the performance of the above algorithm, a 1D FDFD method in the cylindrical coordinates is proposed to fully utilize the rotational symmetry property of the Bragg fiber. In addition to improving the accuracy, this method reduces the computation region from 2D to a straight line, significantly relieving the computation burden. A second method, called Galerkin method, is also developed under cylindrical coordinates. The mode fields are expanded using orthogonal Laguerre-Gauss functions; and the method is accurate and stable. However, it cannot do the loss analysis.

For photonic-band-gap-guiding PCFs, the properties of the confined modes are closely related to the band structures of the cladding photonic crystals. Therefore, a third

FDFD method using periodic boundaries is developed in a generalized coordinate system. Various lattice geometries are analyzed in the same manner, and the results are comparable to those obtained by the plane wave expansion method which is commonly used in the literature.

Finally, a theoretical model for analyzing distributed feedback (DFB) PCF lasers has been presented. Two structures are investigated: PCFs with triangular lattice (TPCF) and PCFs made of capillary tube (CPCF). The modeling and simulation of erbium-doped and erbium/ytterbium (Er/Yb) co-doped DFB lasers are aimed at finding suitable PCF geometry to achieve low threshold and high output power. Various steps involved in this model are: 1) the properties of PCFs are analyzed by the FDFD method; 2) the Bragg grating is investigated by coupled mode theory; 3) the coupled wave equations are solved by transfer matrix method; and 4) Er atom is modeled as a three-level medium while energy transfer between Yb and Er atoms is considered for Er/Yb co-doped fiber.

It is found that a CPCF laser with a smaller mode area is useful for lower-threshold applications and both of CPCF and TPCF lasers with larger mode areas are suitable for high-power operation. Simulation results for Er/Yb co-doped DFB PCF lasers have shown lower threshold and much higher output power and efficiency than Er doped lasers. Furthermore, it is found that the two outputs of a DFB PCF laser are identical when the phase shift is located in the middle of the grating. The output power is a function of the position of the phase shift, and one output could be increased by 46% at the expense of the other when the phase shift moves away from the center to an optimum position. This new DFB fiber laser has huge potential in communications, spectroscopy, and sensing applications.

ACKNOWLEDGMENTS

First, I would like to thank my advisor, Dr. Sacharia Albin, for training me to be competent to work in this research field. His guidance, encouragement and patience were invaluable in the completion of this research. I would also like to thank Dr. John Cooper, Dr. Mounir Laroussi, and Dr. Vijayan Asari for being my dissertation committee members by taking time from their busy schedules to help me bring this research to a conclusion.

Second, I would like to acknowledge Dr. Shangping Guo for sharing his experience and knowledge in photonics. I would also like to thank my colleagues, Dr. Arnel C. Lavarias, Dr. Weihai Fu, Dr. Bing Xiao, Mr. Ron Bentley, Mr. Khalid Ikram, Mr. Haider Ali, and Mr. Kurt Peters. It has been a great pleasure for me to work and talk with each of them, and I have learned a lot from them.

I would also thank Dr. Robert Rogowski and the scientists at Non Destructive Evaluation Sciences Branch, NASA Langley Research Center for their support and cooperation on photonic crystal fiber research through NASA-University Photonic Education and Research Consortium (NUPERC).

Finally, I would like to dedicate my work to my parents and my brother in China for their never-ending love. Last but not least, I am most thankful and ever indebted to my wife, Ms. Wei Jing for her sincere support and sacrifice. Without them, I could not have completed the work.

TABLE OF CONTENTS

Page

TABLE OF CONTENTS v

LIST OF TABLES vi

LIST OF FIGURES vii

INTRODUCTION 1
1.1. An overview 1
1.2. Scope of research 10

MODELING OF PHOTONIC CRYSTAL FIBERS 12
2.1. Analysis method of FDFD with PML 12
2.2. Implementation of FDFD method 15
2.3. Conclusion and discussions 26

MODELING OF BRAGG FIBERS 27
3.1. Galerkin method 28
3.2. Why 1D FDFD method? 34
3.3. 1D FDFD formulation 36
3.4. Implementation of 1D FDFD method 41
3.5. Conclusions 48

MODELING OF PHOTONIC BAND GAP MATERIAL 50
4.1. PWM 51
4.2. FDFD formulation 52
4.3. Comparison between FDFD and PWM 56
4.4 Out-of-plane PBGs of the photonic crystal fiber cladding 61
4.5. Summary and discussion 63

MODELING AND SIMULATION OF DISTRIBUTED FEEDBACK PHOTONIC CRYSTAL FIBER LASERS 64
5.1. Model and Theory 64
5.2. Numerical Results 69
5.3. Conclusion and discussion 79

SUMMARY AND CONCLUSION 81

REFERENCES 85

VITA 90

LIST OF TABLES

TABLE PAGE

1. Calculated mode index of the fundamental mode. The accurate value is $1.445395345 + 3.15\times10^{-8}i$ (by multipole method in [41]) 22

2. The complex mode index with a lossy core material 24

3. Normalized propagation constant b for two step-index fibers with low and high index contrast 31

4. Calculated fundamental mode indices of a step-index fiber. The fiber parameters are: $r_0 = 3\mu m$, $\lambda = 1.5\mu m$, core refractive index $n_{co} = 1.45$ and cladding refractive index $n_{cl} = 1$. The analytical solution is 1.4386042. 42

5. Calculated normalized frequency of fundamental mode of graded-index fibers with parabolic-index cores. The fiber parameters are: $r_0 = 2\mu m$, refractive index in the origin $n_{co} = 1.45$ 43

6. Calculated effective indices of TE/hybrid modes in Bragg fibers. The effective indices calculated using Chew's method are $0.891067 + 1.4226\times10^{-8}i$ and $0.805578+1.7392\times10^{-3}i$ for TE_{01} and hybrid modes, respectively. 44

7. Eigen-frequencies for the first five bands of TE wave (k=0) for a triangular lattice with air holes in dielectric materials. 59

8. Parameters used in the simulations for Er-doped PCF lasers. 71

9. Thresholds for DFB CPCF and TPCF lasers ($N_{Er} = 2.6\times10^{25}$ /m^3, $\kappa = 110$ m^{-1}, $\alpha = 0.25$ /m, and the radius of the doped region is a/2.) 71

10. Parameters used in the simulations for Er/Yb co-doped PCF lasers. 72

11. Thresholds for DFB CPCF and TPCF lasers ($\kappa = 110$ m^{-1}) 77

LIST OF FIGURES

FIGURE PAGE

1. Photonic crystal fibers with solid core (a) and air core (b) and microstructured fibers with high numeric aperture (NA) (c) and high nonlinearity (d). The SEM images are taken from Blaze Photonics.....2

2. Schematic diagram to show the cross-section of the Bragg fiber.....7

3. Schematic diagram of a distributed feedback fiber laser. A phase shift is introduced in the grating.....8

4. The PCF under study. A quarter of the PCF is used in calculation, which can obtain the third and fourth mode classes with a 90-degree rotation symmetry.....16

5. The relative error of the calculated complex mode index of the fundamental mode. The y-axis is the relative error of the real and imaginary part of the mode index of the fundamental mode. Note the different scales of the two y-axes.....18

6. The six field components and the discretization of the transverse index profile in the x-y plane. The E and H components are in red and blue colors respectively. The orange line denotes the curved interface across the cells, and the dotted cells show the integration plane for Ex and Ey respectively.....19

7. Calculation of Ex, Ey and Ez using Ampere's law. The orange line denotes the dielectric boundary in the integration plane. From left to right are the integration cells for Ex, Ey and Ez respectively.....20

8. The accuracy and convergence of the complex effective mode index using a more reasonable averaging technique. Note that the scale of the right y-axis is at least an order of magnitude smaller than the corresponding one in Fig. 5.....21

9. The mode field patterns of the fundamental mode (top three) and 2^{nd}-order mode (bottom three) in the degenerate mode class 3 and 4.....23

10. Some spurious cladding modes created by the artificial waveguide between the PML + zero boundary and the air holes. These modes are weak and highly lossy.....25

11. Fields E_ϕ and H_ϕ of TE_{01} and TM_{01} respectively in two standard step index fibers with low and high index contrast (N=100).....32

12. The effective indices n_{eff} of TE modes in a Bragg fiber and the field E_ϕ of TE_{01} mode at λ=1.55μm (N=200). 33

13. Yee's 1D lattice in cylindrical coordinates. (a) For hybrid and TM modes, (b) For hybrid and TE modes. 37

14. Yee's lattice with open boundary. 41

15. Relative error vs. number of grids taken for computation. 42

16. Convergence property for TE_{01} (upper) mode and hybrid mode (m = 1) (bottom) calculation. 45

17. Electric field distribution for TE_{01} in an OmniGuide fiber with a large air core [83]. The radius of the air core is $r = 30a$. The thicknesses of the layers with high and low indices (n_{hi} = 4.6, n_{lo} = 1.6) are $t_{hi} = 0.22a$ and $t_{lo} = 0.78a$; a = 0.434 μm, the wavelength λ = 1.55 μm. The bottom graph shows expanded amplitude to obtain the electric field variation in the periodic cladding. The core is surrounded by 17 layers. 140 grids are taken for each bi-layer. 46

18. Field distributions of hybrid modes m = 1 and m = 4. The parameters of this fiber are: r = 0.475 μm, λ = 1.55 μm, n_{hi} = 4.6, n_{lo} = 1.5, t_{hi} = 0.158 μm, t_{lo} = 0.032 μm [54]. The core is surrounded by 12 bi-layers. 120 grids are taken for each bi-layer. The calculated effective indices are: $0.6004 + 1.370 \times 10^{-3}i$ (m = 1) and $1.0675 + 5.753\times 10^{-2}i$ (m = 4). Computation time is about 8 s on a P4 1.5G computer. 47

19. Dispersion curves for high-index core Bragg fibers with different core index profile. The FDFD and TMM results are overlapped for Δ = 0 which represents the step index core. 48

20. Yee's 2D mesh in general coordinates. The dotted components are at the boundaries. 54

21. The band structure for a 2D square lattice by FDFD (o) and PWM (-). 441 plane waves are used for PWM and mesh resolution is a/80 for FDFD. Upper: TM mode, Bottom: TE mode. 57

22. The calculated band structure of a triangular lattice by FDFD (o) and PWM (-). 441 plane waves are used for PWM and mesh resolution is a/80 for FDFD. Upper: TM, Bottom: TE. 58

23. The convergence of eigen-frequency (the 5^{th} band at k=0) and the computation time vs. the number of grids along each direction. 60

24. The E_z field of a defect mode in a 2D square lattice with alumina rods in air using a 5×5 supercell with the center rod removed. The rods are displayed as black circles. 61

25. Out-of-plane band structure diagram of a triangular photonic crystal with a 70% air-filling ratio. The propagation constant is fixed as βa = 9.0. Refractive index of silica is 1.45 62

26. Schematic diagram of a grating. 65

27. Three-level energy level diagram for Erbium 66

28. Energy level transitions for Er^{3+}/Yb^{3+} systems 67

29. Segmentation diagram for modeling a distributed feedback laser 68

30. Schematic diagrams of the cross section of a CPCF (left) and a TPCF (right). The solid red circles in the center represent the doped region 69

31. The spectrum of the grating (g = 0) with a phase shift π in the middle. 70

32. Output characteristics near the thresholds of Er doped DFB CPCF lasers (left) and TPCF lasers (right). $N_{Er} = 2.6\times10^{25}$ /m^3. The radius of doped region is a/2, and signal propagation loss $\alpha = 0.25$ m^{-1} 71

33. Output power as a function of coupling constant κ for DFB CPCF lasers. A phase shift of π is introduced in the center of the grating. The background signal transmission loss $\alpha = 0$ and 0.25 m^{-1}. Pump power is 100 mW. $N_{Er} = 2.6\times10^{25}$ /m^3, $N_{Yb} = 3.25\times10^{26}$ /m^3 73

34. Output power at two ends of the Bragg grating as a function of the position of the phase shift for DFB CPCF laser with a lattice constant of 3.4 μm. The pump power , the coupling constant, and signal propagation loss are 100 mW, 110 m^{-1}, and 0.25 m^{-1}. $N_{Er} = 2.6\times10^{25}$ /m^3, $N_{Yb} = 3.25\times10^{26}$ /m^3 74

35 Signal intensity distribution within the Bragg grating. The parameters used to calculate this profile are: κ=110 m^{-1}, the pump power = 100 mW, signal propagation loss $\alpha = 0.25$ m^{-1}, and the phase shift of π is located at 2.5 cm. $N_{Er} = 2.6\times10^{25}$ /m^3, $N_{Yb} = 3.25\times10^{26}$ /m^3. 75

36. Output powers as functions of pump powers near the thresholds (signal propagation loss $\alpha = 0.25$ m^{-1}). Left column: DFB CPCF lasers, Right column: DFB TPCF lasers. 78

37. Output powers as functions of pump powers (signal propagation loss α = 0.25 m^{-1}.) Left column: DFB CPCF lasers. Right column: DFB TPCF lasers. 79

CHAPTER I

INTRODUCTION

In this chapter, the background and scope of the research are introduced. In section 1.1, a brief introduction about photonic crystal fiber (PCF) is given first, followed by an overview on the methods for modeling PCFs. Due to the unique symmetry property of Bragg fibers, the modeling methods are different and explored in this section also. In the last part of section 1.1, the development of the distributed feedback (DFB) PCF laser is introduced. In section 1.2, the scope of this research is described.

1.1. An overview

1.1.1 Photonic crystal fiber

With the advent of the photonic crystals or photonic band gap (PBG) materials [1, 2], a new concept in fiber optics called photonic crystal fiber (PCF) has come to the forefront in fiber research. Photonic crystal is an artificial material with periodically arranged structures that allow the researcher to tailor the dielectric constant. Within the photonic crystal, light propagation with certain wavelengths is forbidden, similar to a Faraday cage. The cladding of a PCF consists of periodically arranged air holes running through the whole length of the fiber. Light is confined to a core area which is created for a specific purpose. For example, the core can be an air hole to guide high-power beams or a solid material for an index-guiding PCF. Fig. 1 shows two different confinement techniques, by index difference and PBG, allowed in a PCF. The index-guiding PCF has a solid core as shown in Fig. 1a. The PBG-guiding PCF may have an air core as shown in Fig. 1b.

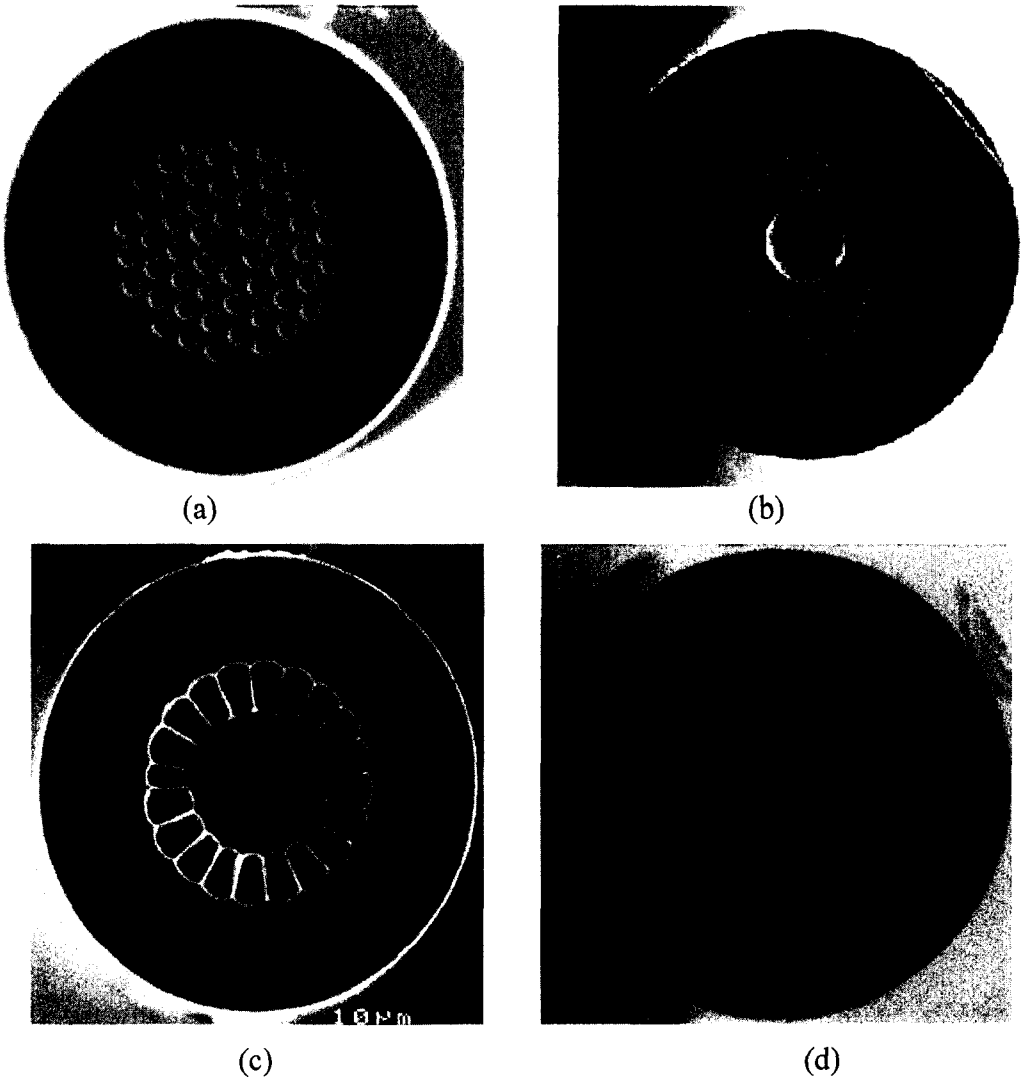

Fig. 1. Photonic crystal fibers with solid core (a) and air core (b) and microstructured fibers with high numeric aperture (NA) (c) and high nonlinearity (d). The SEM images are taken from Blaze Photonics.

The concept of photonic crystal fiber was proposed by Russell et al., and the fiber was fabricated in 1996 [3, 4]. This new fiber is made of single material unlike the conventional fiber in which the core is doped with germanium to get higher refractive index. The light in PCF may still be guided by total internal reflection (TIR) as with conventional step-index fiber; but due to the unique structure of the cladding, the index-guiding PCF has its own unique properties. The light guiding mechanism may also be different than conventional fiber due to the creation of a PBG in cladding area, creating

forbidden wavelength bands. In this case, wavelengths within the PBG will be totally reflected by the cladding and confined in the core.

Because of their new structures, PCFs have several properties that conventional fibers can not provide, for example: 1) endless single-mode [5], 2) ultra-flattened dispersion [6, 7], and 3) super-continuum generation [8, 9]. Air-guiding PCF, where light is guided in the air region [10-13], has opened a new area that attracts more and more researchers. With the development of the PCF, some new types of fibers have been proposed for some special applications as shown in Figs. 1c and 1d. These fibers were made by using a single material which is the same as PCF, but the air regions in the cladding may not be periodically arranged. All of them can be called microstructured fiber (some prefer the name, holey fiber).

1.1.2. PCF Modeling methods

To understand the properties of PCFs and design different PCFs for different applications, we need to model them first. In general, modeling PCFs takes advantage of the fact that the E and/or H field can be decomposed into longitudinal and transverse components in waveguides with invariant index profiles along the z-direction. The field confined to the fiber can be written as:

$$\xi(x,y,z,t) = \{\xi_t(x,y) + \xi_z(x,y)\}\exp[-j(\omega t - \beta z)] \tag{1.1}$$

where ξ denotes E or H field, and the subscripts t and z denote, respectively, the transverse and longitudinal components. β is the propagation constant.

The full-vectorial Helmholtz equations can be obtained by substituting Eq. (1.1) into Maxwell's equations:

$$\left(\nabla_t^2 + k_0^2 n^2 - \beta^2\right)E_t = -\nabla_t\left(E_t \cdot \nabla_t \ln n^2\right) \tag{1.2a}$$

$$\left(\nabla_t^2 + k_0^2 n^2 - \beta^2\right) H_t = \left(\nabla_t \times H_t\right) \times \nabla_t \ln n^2 \tag{1.2b}$$

$$\left(\nabla_t^2 + k_0^2 n^2 - \beta^2\right) E_z = j\beta E_t \cdot \nabla_t \ln n^2 \tag{1.2c}$$

$$\left(\nabla_t^2 + k_0^2 n^2 - \beta^2\right) H_z = \left(\nabla_t H_z + j\beta H_t\right) \cdot \nabla_t \ln n^2 \tag{1.2d}$$

The Helmholtz equations allow us to draw several important conclusions: it is possible to form an eigen-value problem using the transverse E or H components since Eqs. (1.2a-b) only contain the transverse components. However, this is not true for the z-components since they are coupled to the transverse components. When the index change is small and the coupled items on the right-hand side are omitted, (which is the scalar approximation), all four equations become the same, and an eigen-value problem can be formed for any E or H component.

In holey or microstructured fibers, the index contrast of the materials is generally high compared to the convention fiber, hence the scalar wave-analysis methods are not accurate to predict their propagation properties, and a full-vector approach is required. So far, a few full-vector methods have been used to characterize microstructured fibers, such as the plane-wave-expansion method (PWM) [6, 14-17], localized function method [18-21], beam-propagation method [22-25], finite-element method (FEM) [26-31], and finite-difference method (FDM) in time domain [32-37] or frequency domain [38-40]. Specifically, a highly accurate semi-analytical multipole method [41] has been developed to model fibers with circular air hole inclusions. A brief review of these methods is given below.

The PWM for PCFs is an extension of modeling for photonic crystals. It assumes an infinite, periodic index profile and treats the unit cell or supercell by applying the Bloch boundary (periodic boundary) conditions. The eigen-matrix is a full matrix and the

complexity is the same as the PWM for photonic crystals. It is adequate for index-guiding fibers with many periodic air holes in the cladding, however, the artificial periodic boundary condition and supercell approach are not very suitable for many real fiber structures with a finite number of air holes.

The localized function method is based on Galerkin's method and has been widely used for waveguide analysis, both for scalar and vectorial problems. This method applies a set of localized orthogonal functions, such as sine/cosine [42], Laguerre-Gauss [43, 44] (for a one dimensional waveguide), and Hermite-Gauss [16, 18, 19, 21] (for the 2D problem), to approximate the unknown mode fields of the localized modes. When the mode is far away from the cut-off or well-confined, the mode fields can be approximated using tens or hundreds of functions. These methods generally involve integrations, which are computationally intensive, and convergence is generally a problem.

The FEM [26-31] is a powerful numerical tool for waveguide problems. It often combines the beam propagation method (described below) or simply solves the Helmholtz equation in the frequency domain by discretizing the region of interest into triangular cells, which is able to represent fine curved structures by denser cells. Hence, FEM can provide high accuracy, but the complexity of the implementing the algorithm is generally high.

The FDM using Yee's mesh [45] is popular for electromagnetic problems. A compact-2D scheme is often used for waveguides invariant in the propagation direction. In the scheme, the derivatives in the propagation direction are analytically calculated. Compared to FEM, FDM is much easier to implement; yet, it offers a comparable accuracy. The FDM approach includes both a time domain (FDTD) and a frequency

domain (FDFD) method. The compact-2D FDTD [32-37] method solves the eigen-frequency for a given propagation constant, and therefore is unable to process material dispersion. The FDFD approaches include those based on solving the Helmholtz equation [38, 39] or Maxwell's equations [40] directly.

In practical holey fibers with air hole inclusions, the confinement (by either index guiding or PBG guiding) is not perfect due to the finite cladding; hence, the confinement loss is a significant characteristic of microstrucured fiber. It has been calculated using several methods, including the semi-analytical multipole method [41], Fourier expansion method [46], and FEM with anisotropic perfectly matched layers (PMLs) [28]. PWM and Hermite-Gauss methods have not been used for leakage loss calculations.

1.1.3. Bragg fiber Modeling methods

Fig. 2 schematically shows the cross-section of a Bragg fiber. The cladding consists of alternate layers with high and low refractive indices. The Bragg fiber was first analyzed by Yeh et al. [47]. Since then, several numerical approaches have been used to analyze the modal properties in Bragg fibers [47-52], among which, the transfer matrix method (TMM) is most common. It obtains the band gap by searching for the fast increasing solutions [49]. The increasing numerical errors from layer to layer make it difficult to obtain the eigen-modes. In Ref. [50-52], periodic alternate layers were approximated by planar Bragg stacks using an asymptotic approximation of Bessel functions [50-52]; therefore, Bloch theorem can be used to overcome the weakness of transfer matrix method.

Another popular method for analyzing the Bragg fibers is the method of Chew [53] where 2×2 matrices are used rather than 4×4 as in TMM. In both methods, Bessel

functions are used to represent the fields in each homogeneous layer and continuous boundary conditions for the tangential fields are employed to solve the Maxwell's equations. Unfortunately, these methods are not suitable for structures with inhomogeneous layers.

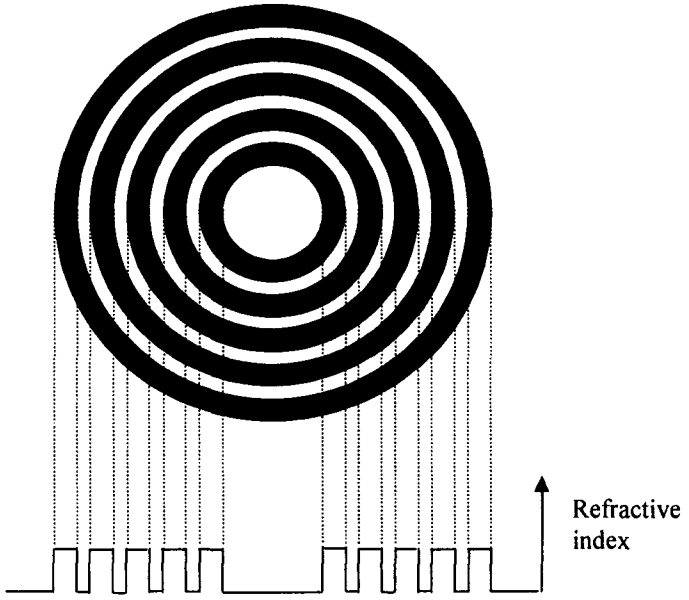

Fig. 2. Schematic diagram to show the cross-section of the Bragg fiber.

The FDTD method was also used to analyze Bragg fibers [54]. A proper initial field is needed to excite the specific modes, and a certain amount of iterations is required to do the Fourier transform, thus making the FDTD analysis tedious and time-consuming.

1.1.4. Distributed feedback PCF lasers

PCF is finding applications in both linear and nonlinear fiber optics fields. One of the most important applications in nonlinear fiber optics is the fiber laser. Continuous-wave (CW) single-frequency lasers are used widely in telecommunication, spectroscopy, and sensing. By introducing Bragg gratings into the fiber core, erbium (Er) doped fiber lasers

are a good alternative to semiconductor lasers. Among these fiber lasers, phase-shifted DFB fiber lasers as shown in Fig. 3 are attractive due to compatibility with current fiber technology, compact size, reliability, and narrow linewidth.

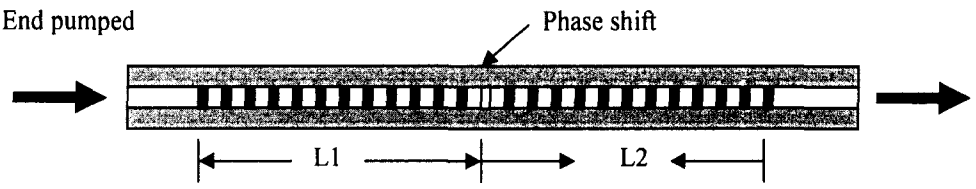

Fig. 3. Schematic diagram of a distributed feedback fiber laser. A phase shift is introduced in the grating.

In recent years, both theory and applications have increased quickly to exploit those properties that cannot be provided by standard step-index fiber. One of them is that PCF, with properly designed parameters, can be single mode at wavelengths from ultraviolet (UV) to far-infrared (FIR) [5]. This property improves the pumping efficiency of the DFB fiber laser.

Conventional DFB fiber lasers are generally pumped by semiconductor lasers at 980 nm. The laser operates at a wavelength in the long-haul fiber's third communication window around 1550 nm. Since the pump propagates in multimode, certain amount of the pump power enters the cladding, while the fiber laser is essentially confined to the core. The overlap of the intensity distributions between pump and signal is poor. For PCF, both the pump and the signal operate in single mode, thus the overlap is highly improved and better pumping efficiency can be achieved.

Another important feature useful to fiber lasers is that the mode area of PCF could be adjusted in a relatively wide range while still ensuring single-mode operation [55]. Fiber

lasers with small mode areas are interesting for low-threshold operation, whereas lasers with large mode area could yield high power.

By incorporating an ytterbium (Yb) doped core into a PCF, the first Yb-doped PCF laser was demonstrated at the University of Bath in 2000 [56]. This proved the huge potential of PCF for fiber laser applications. One year later, a group in Southampton University reported the first mode-locked Yb-doped PCF laser [57]. A Yb-doped fiber laser with double claddings was shown in the same year [58]. The double-cladding design provided efficiencies over 80% and output powers above 1 W. In 2002, an application of PCF in a femtosecond, Yb-fiber laser was demonstrated [59]. This fiber laser utilized the anomalous dispersion of PCF at 1 μm to form solitons. In 2003, a 2.3 m long, air-clad, Yb-doped large-mode-area PCF laser generated an output power up to 80 W with a slope efficiency of 78% [60]. The first experimental report on a distributed Bragg reflector (DBR) PCF laser was presented by J. Canning et al. who employed two-photon 193 nm radiation to fabricate two Bragg gratings into the PCF [61]. Very recently, an Er-doped DFB PCf laser was demonstrated by the same group [62].

To date, there is a lack of numerical models that are capable of optimizing the DFB PCF laser design. Only one paper has proposed a model to simulate DFB PCF lasers [63]. Unfortunately, Er/Yb co-doped fiber lasers were not considered in the paper. Due to the small absorption cross-section of Erbium at 980 nm, a few cm-long fiber does not allow sufficient pump absorption, which consequently leads to low output power for Er-doped DFB lasers. On the other hand, Er/Yb co-doped DFB fiber lasers could obtain much higher output powers owing to the high absorption cross-section of Yb atom at 980 nm.

Thus, Er/Yb co-doping is widely used in fabricating fiber lasers. It is necessary and meaningful to do more work on the modeling and simulation for this new DFB PCF laser.

1.2. Scope of research

The goal of my research is to find a model which is simple and suitable for different types of PCFs. With the model combined with the coupled mode theory, the transfer matrix method, and the gain models for Er and Yb media, DFB PCF fiber lasers are simulated to find proper geometry and parameters for PCFs to achieve low threshold or high output power.

Compared with the other modeling methods discussed in the previous section, the FDFD method is appealing for several reasons: 1) material dispersion and material loss are easy to be incorporated into FDFD, 2) no second order derivatives are required, 3) the method is fast and accurate, mathematically simple and straightforward, 4) all six fields are obtained from the transverse E or H field, 5) different boundaries such as the Bloch boundary (periodic boundary) for PBG calculations [64-66] can be readily applied, and 6) sparse techniques can be used to reduce memory requirement and computation time. In chapter 2, a FDFD method combined with the PML technique is proposed for analyzing the dispersion and loss properties of PCFs.

The general method proposed in chapter 2 for PCFs is not efficient to analyze Bragg fiber due to the unique symmetry property. By fully utilizing the rotational symmetry property, another FDFD method is proposed that is combined with the PML technique in cylindrical coordinates. This method dramatically reduces the computational burden by simplifying the problem from two-dimensional (2D) to one-dimensional (1D). The FDFD method proposed for Bragg fibers is discussed in chapter 3.

Since PBG-guiding PCFs guide light based on PBG effect, a FDFD method in a general coordinate system to calculate the band structures of photonic crystals is proposed. The details are demonstrated in chapter 4.

Finally, the DFB PCF lasers are modeled and simulated in chapter 5. The output characteristics of both Er/Yb co-doped and Er-doped DFB PCF lasers are analyzed by solving the classical coupled-wave equations [67] using the transfer matrix method [68]. The Er medium, in this case, is modeled as a three-level system. For Er/Yb co-doped medium, the energy transfer between Yb and Er atoms is considered

CHAPTER II

MODELING OF PHOTONIC CRYSTAL FIBERS

Photonic crystal fibers have been attracting more and more interests as they offer design flexibility in controlling the mode propagation properties. These fibers have some extraordinary properties, such as endless single mode propagation, special dispersion, and high or low nonlinear effects. Air-guiding fibers such as the air-core photonic band gap fibers or Bragg fibers are also of considerable interest. Reviews of photonic crystal fibers can be found in [69-71] and the references therein.

In this chapter, the compact-2D FDFD approach described in [40] for optical waveguides based on directly solving the Maxwell's equations is employed to include the calculation of mode leakage loss due to the finite cladding. By applying the anisotropic PML layers, both the dispersion and loss properties can be evaluated in a single run. The method preserves all the advantages discussed in the overview section in Chapter I and is simple and straightforward. The curved profile at the media interface is studied carefully to increase both the accuracy and convergence of the complex propagation constant. The analysis method is given in section 2.1; a PCF with a single ring of air holes are numerically analyzed in section 2.2 along with the averaging technique at the media interface. Section 2.3 gives the conclusion and discussions.

2.1. Analysis method of FDFD with PML

The leakage loss of a mode can be represented by the imaginary part of its complex propagation constant. To model the leakage, an open boundary condition has to be used, which produces no reflection at the boundary. The PML is so far the most efficient absorption boundary condition for this purpose. The split-field PML proposed by

Berenger [72] which is often used in FDTD algorithm cannot be applied in frequency domain methods such as the FEM and FDFD methods since it introduces non-Maxwellian equations. The equivalent nonsplit-field anisotropic PML [22, 73-79] has been proposed instead to simulate the open environment in these applications. The Maxwell equations for optical waveguide with anisotropic PML boundaries are expressed as:

$$\begin{aligned} jk_0 s\varepsilon_r E &= \nabla \times H \\ -jk_0 s\mu_r H &= \nabla \times E \end{aligned} \tag{2.1}$$

$$s = \begin{bmatrix} s_y/s_x & & \\ & s_x/s_y & \\ & & s_x s_y \end{bmatrix} \tag{2.2}$$

For exp(-jωt) convention which is used in this chapter:

$$s_x = 1 - \frac{\sigma_x}{j\omega\varepsilon_0}, \quad s_y = 1 - \frac{\sigma_y}{j\omega\varepsilon_0} \tag{2.3}$$

where σ is the conductivity profile.

In the compact-2D scheme for waveguides, the z-derivatives are replaced by analytical expressions using Eq. (1.1), and other derivatives are replaced by finite differences in Yee's mesh. Therefore, the curl equations (2.1) can be expressed in a matrix form:

$$-jk_0 \begin{bmatrix} s_y/s_x\,\varepsilon_{rx} & & \\ & s_x/s_y\,\varepsilon_{ry} & \\ & & s_x s_y \varepsilon_{rz} \end{bmatrix} \begin{bmatrix} E_x \\ E_y \\ E_z \end{bmatrix} = \begin{bmatrix} 0 & -j\beta I & V_y \\ j\beta I & 0 & -V_x \\ -V_y & V_x & 0 \end{bmatrix} \begin{bmatrix} H_x \\ H_y \\ H_z \end{bmatrix} \tag{2.4a}$$

$$jk_0 \begin{bmatrix} s_y/s_x\,\mu_{rx} & & \\ & s_x/s_y\,\mu_{ry} & \\ & & s_x s_y \mu_{rz} \end{bmatrix} \begin{bmatrix} H_x \\ H_y \\ H_z \end{bmatrix} = \begin{bmatrix} 0 & -j\beta I & U_y \\ j\beta I & 0 & -U_x \\ -U_y & U_x & 0 \end{bmatrix} \begin{bmatrix} E_x \\ E_y \\ E_z \end{bmatrix} \tag{2.4b}$$

where the U and V are sparse matrices which are obtained in the same way as in [40, 64] using a zero boundary outside of the PML layers. There is no need to treat PML in a special way as in split-field scheme.

For simplicity, we assume:

$$\varepsilon'_{rx} = s_y / s_x \, \varepsilon_{rx}, \quad \varepsilon'_{ry} = s_x / s_y \, \varepsilon_{ry}, \quad \varepsilon'_{rz} = s_x s_y \varepsilon_{rz} \tag{2.5}$$

and

$$\mu'_{rx} = s_y / s_x \, \mu_{rx}, \quad \mu'_{ry} = s_x / s_y \, \mu_{ry}, \quad \mu'_{rz} = s_x s_y \mu_{rz} \tag{2.6}$$

Substituting Eq. (2.4a) into Eq. (2.4b) and eliminating H_z as in [40], an eigen-value problem can be obtained for H_t:

$$\begin{bmatrix} Q_{xx} & Q_{xy} \\ Q_{yx} & Q_{yy} \end{bmatrix} \begin{bmatrix} H_x \\ H_y \end{bmatrix} = \beta^2 \begin{bmatrix} H_x \\ H_y \end{bmatrix} \tag{2.7}$$

and similarly for E_t:

$$\begin{bmatrix} P_{xx} & P_{xy} \\ P_{yx} & P_{yy} \end{bmatrix} \begin{bmatrix} E_x \\ E_y \end{bmatrix} = \beta^2 \begin{bmatrix} E_x \\ E_y \end{bmatrix} \tag{2.8}$$

where:

$$P_{xx} = \mu'_{ry} V_y \mu'^{-1}_{rz} U_y + U_x \varepsilon'^{-1}_{rz} V_x \varepsilon'_{rx} + k_0^2 \mu'_{ry} \varepsilon'_{rx} + k_0^{-2} U_x \varepsilon'^{-1}_{rz} \{V_x V_y - V_y V_x\} \mu'^{-1}_{rz} U_y \tag{2.9a}$$

$$P_{xy} = -\mu'_{ry} V_y \mu'^{-1}_{rz} U_x + U_x \varepsilon'^{-1}_{rz} V_y \varepsilon'_{ry} + k_0^{-2} U_x \varepsilon'^{-1}_{rz} \{V_y V_x - V_x V_y\} \mu'^{-1}_{rz} U_x \tag{2.9b}$$

$$P_{yx} = -\mu'_{rx} V_x \mu'^{-1}_{rz} U_y + U_y \varepsilon'^{-1}_{rz} V_x \varepsilon'_{rx} + k_0^{-2} U_y \varepsilon'^{-1}_{rz} \{V_x V_y - V_y V_x\} \mu'^{-1}_{rz} U_y \tag{2.9c}$$

$$P_{yy} = \mu'_{rx} V_x \mu'^{-1}_{rz} U_x + k_0^2 \mu'_{rx} \varepsilon'_{ry} + U_y \varepsilon'^{-1}_{rz} V_y \varepsilon'_{ry} + k_0^{-2} U_y \varepsilon'^{-1}_{rz} \{V_y V_x - V_x V_y\} \mu'^{-1}_{rz} U_x \tag{2.9d}$$

and

$$Q_{xx} = \varepsilon'_{ry} U_y \varepsilon'^{-1}_{rz} V_y + V_x \mu'^{-1}_{rz} U_x \mu'_{rx} + k_0^2 \varepsilon'_{ry} \mu'_{rx} + k_0^{-2} V_x \mu'^{-1}_{rz} \{U_x U_y - U_y U_x\} \varepsilon'^{-1}_{rz} V_y \tag{2.10a}$$

$$Q_{xy} = -\varepsilon'_{ry} U_y \varepsilon'^{-1}_{rz} V_x + V_x \mu'^{-1}_{rz} U_y \mu'_{ry} + k_0^{-2} V_x \mu'^{-1}_{rz} \{U_y U_x - U_x U_y\} \varepsilon'^{-1}_{rz} V_x \tag{2.10b}$$

$$Q_{yx} = -\varepsilon'_{rx} U_x \varepsilon'^{-1}_{rz} V_y + V_y \mu'^{-1}_{rz} U_x \mu'_{rx} + k_0^{-2} V_y \mu'^{-1}_{rz} \{U_x U_y - U_y U_x\} \varepsilon'^{-1}_{rz} V_y \tag{2.10c}$$

$$Q_{yy} = \varepsilon'_{rx} U_x \varepsilon'^{-1}_{rz} V_x + k_0^2 \varepsilon'_{rx} \mu'_{ry} + V_y \mu'^{-1}_{rz} U_y \mu'_{ry} + k_0^{-2} V_y \mu'^{-1}_{rz} \{U_y U_x - U_x U_y\} \varepsilon'^{-1}_{rz} V_x \qquad (2.10d)$$

In the absence of PML media, the equations given above are reduced to those obtained in [40]. Hence, we can validate our results by setting the thickness of PML layers to zero.

The waveguide is encompassed by PML layers followed by a layer of perfect electric conductor (PEC) or zero boundaries. The modes leaking out of the fiber will be absorbed efficiently by the PML with very small reflections; hence, the effect of the artificial boundary on the modes in the PCF will be minimized (especially for those well-localized guided modes).

2.2. Implementation of FDFD method

2.2.1 The example for analysis

The PCF example in [41] is used in this chapter since the analytical results using multipole method are available for comparison. The PCF has a single ring of air holes (6 holes) in glass fiber. The parameters used are: the lattice constant a = 6.75μm, the air hole radius r = 2.5μm, and the refractive index of the glass is 1.45. The material dispersion is omitted since it is trivial to include it in a compact-2D FDFD scheme. According to the multipole method, the accurate effective mode index at wavelength 1.45μm would be $1.445395345+3.15\times10^{-8}$i.

This PCF has a symmetry of C_{6v} (six-fold rotation symmetry and at least one plane of reflection symmetry), and the computation region can be reduced using the symmetry properties by applying a combination of PEC and PMC (perfect magnetic conductor) [80]. The PCFs with such symmetry supports eight mode classes. Fig. 4 shows the fiber profile and a quarter of the whole region used for computation of the third and fourth mode

classes, which are degenerate pairs with a 90-degree rotation symmetry including the fundamental mode. Glass material is assumed to extend uniformly to infinity, and PML layers are used outside the computation region with a 2^{nd}-order power law profile. The computation region is chosen to be $1.5a$ along both x and y directions and the thickness of the PML layers is 10% of the thickness of the inside area along x or y direction.

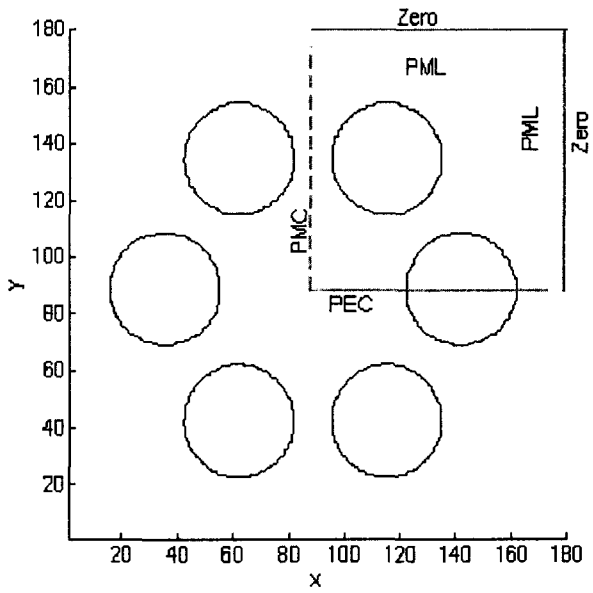

Fig. 4. The PCF under study. A quarter of the PCF is used in calculation, which can obtain the third and fourth mode classes with a 90-degree rotation symmetry.

The computation region is discretized by a 2D Yee's mesh. The curved interface crossing a cell is generally approximated using a staircase scheme or averaged using the effective index scheme. The averaging technique is shown to be very effective in increasing convergence and accuracy as in [40]. Considering two different media in the cell, the average dielectric constant in the cell can be evaluated as:

$$\varepsilon = \varepsilon_a f + \varepsilon_b (1 - f) \tag{2.11}$$

where f is the fraction of the first material ε_a.

By applying the boundaries shown in Fig. 4, we obtained the U and V matrices

$$U_y = \frac{1}{\Delta y}\begin{bmatrix} -1 & 1 & & & & \\ & -1 & 1 & & & \\ & & \ddots & \ddots & & \\ & & & -1 & 1 & \\ & & & & -1 & \\ & & & & & -1 \end{bmatrix}, \quad V_y = \frac{1}{\Delta y}\begin{bmatrix} 1 & -1 & & & & \\ & 1 & -1 & & & \\ & & \ddots & \ddots & & \\ & & & 1 & -1 & \\ & & & & 1 & \\ & & & & & 1 \end{bmatrix}. \tag{2.12}$$

$$U_x = \frac{1}{\Delta x}\begin{bmatrix} -1 & 1 & & & & \\ & \ddots & \ddots & & & \\ & & -1 & 0 & & \\ & & & \ddots & \ddots & \\ & & & & -1 & 0 \\ & & & & & -1 \end{bmatrix}, \quad V_x = \frac{1}{Q_1}\begin{bmatrix} 1 & & & & & \\ -1 & \ddots & & & & \\ & \ddots & 1 & & & \\ & & 0 & 1 & & \\ & & & \ddots & \ddots & \\ & & & & -1 & 1 \end{bmatrix} \tag{2.13}$$

where Δx and Δy are mesh size in x and y directions, respectively.

2.2.2. Convergence property

Fig. 5 shows the relative error of the calculated complex effective mode index of the fundamental mode with different number of grids. The real part of the effective mode index converges quickly to an accuracy of 10^{-5}~10^{-6} even if a coarse mesh (for example, 30×30) is used; the accuracy is sufficient to obtain group velocity dispersion and other parameters. However, the imaginary part converges rather slowly with a relative error in the range of $10^{-1} \sim 10^{-2}$ with almost 30% relative error using a 30×30 mesh. Though it converges to the true value with a fine mesh, the slow convergence is still not satisfactory.

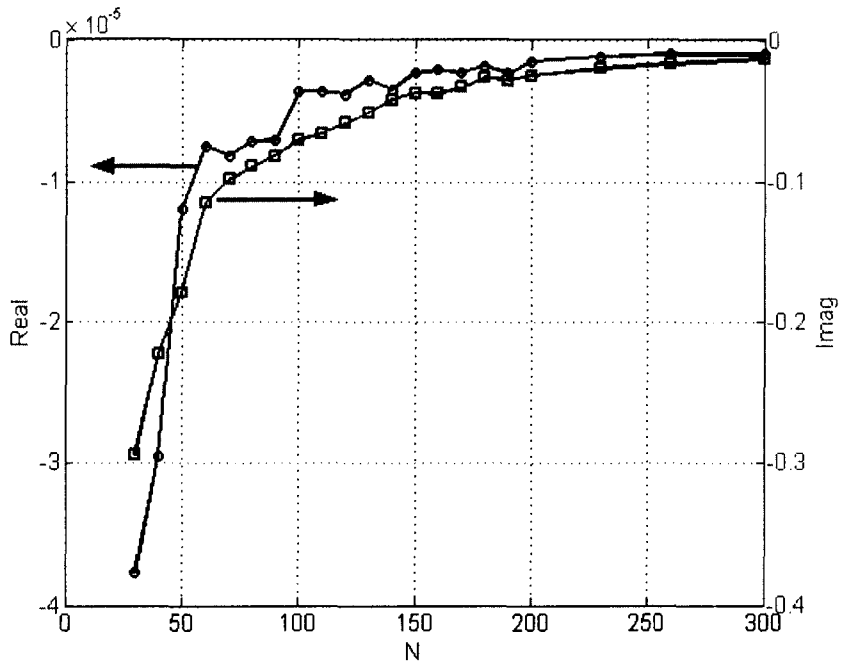

Fig. 5. The relative error of the calculated complex mode index of the fundamental mode. The y-axis is the relative error of the real and imaginary part of the mode index of the fundamental mode. Note the different scales of the two y-axes.

2.2.3. Averaging technique for performance improvement

We found that the slow convergence of the imaginary part is due to the improper averaging technique at the interface of the two dielectric materials. It can be greatly improved using a more reasonable averaging technique at the interface. Our averaging scheme is shown in Fig. 6. ε_{rx}, ε_{ry} and ε_{rz} are the averaged dielectric constant of the cell located at the same position as E_x, E_y and E_z.

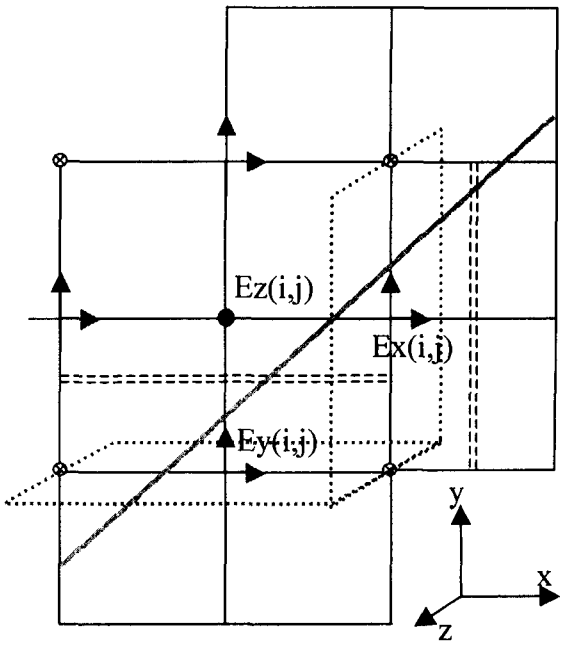

Fig. 6. The six field components and the discretization of the transverse index profile in the x-y plane. The E and H components are in red and blue colors respectively. The orange line denotes the curved interface across the cells, and the dotted cells show the integration plane for Ex and Ey respectively.

First, we check the averaging technique using Ampere's Law (the curl equation):

$$\frac{\partial}{\partial t}\iint_{A_1}\varepsilon_x E_x dydz = \oint_{l_1} H \cdot dl \tag{2.14a}$$

$$\frac{\partial}{\partial t}\iint_{A_2}\varepsilon_y E_y dxdz = \oint_{l_2} H \cdot dl \tag{2.14b}$$

$$\frac{\partial}{\partial t}\iint_{A_3}\varepsilon_z E_z dxdy = \oint_{l_3} H \cdot dl \tag{2.14c}$$

The integration area is the cell formed by the four surrounding H components as shown in Fig.7. It shows the intersection of the curved interface on the integration surface. In each of these surfaces, the E component is tangential to the interface and will be continuous across it, and the average of the E field is used for the value at the cell center. Taking E_z as an example:

$$\frac{\partial}{\partial t}\left(\bar{\varepsilon}_z \bar{E}_z \Delta x \Delta y\right) = \oint_{l_3} H \cdot dl \quad \text{and} \quad \bar{\varepsilon}_z = f\varepsilon_a + (1-f)\varepsilon_b \tag{2.15}$$

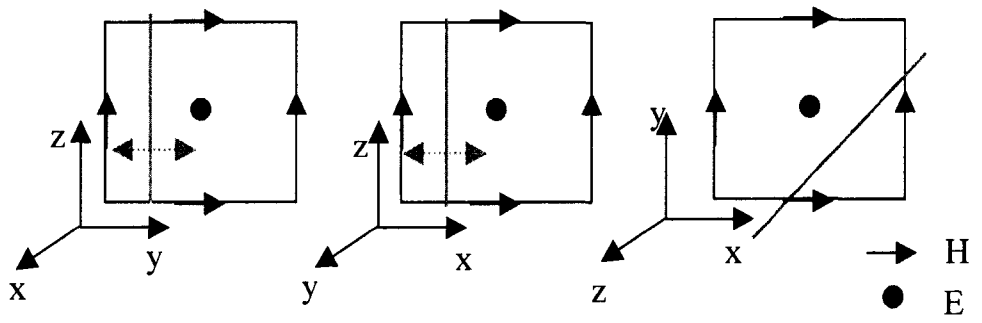

Fig. 7. Calculation of Ex, Ey and Ez using Ampere's law. The orange line denotes the dielectric boundary in the integration plane. From left to right are the integration cells for Ex, Ey and Ez respectively.

For ε_x in yz plane and ε_y in xz plane, the averaging is easy to do since the boundary is parallel to z direction and the integration cell shrinks to a line, which is shown in Fig. 6 as the dotted cells.

E_x and E_y in the xy plane as shown in Fig. 6 are not tangential to the dielectric interface, and therefore will not be continuous across the dielectric boundary. As in Fig. 7, when the integration surface for E_x moves along x in the cell on the xy plane, the interface will shift, and similar is the case for E_y. Since E_x and E_y are the average field values of the cell in xy plane, another average has to be taken and the averaged dielectric values are [37]:

$$\bar{\varepsilon}_x = \left[\frac{1}{\Delta x}\int_x^{x+\Delta x} \frac{1}{\varepsilon_a f(x) + \varepsilon_b (1-f(x))} dx\right]^{-1} \tag{2.16}$$

$$\bar{\varepsilon}_y = \left[\frac{1}{\Delta y}\int_y^{y+\Delta y} \frac{1}{\varepsilon_a f(y) + \varepsilon_b (1-f(y))} dy\right]^{-1} \tag{2.17}$$

The average rule described in Eqs. (2.11, 2.16-2.17) could also be derived as the classical rules for the evaluation of effective dielectric constants as described in Milton's

book [81]. The integration can be approximated well using a denser subcell mesh along x or y as the two dashed lines shown in Fig. 6. The same averaging procedure can be applied to magnetic materials with a profile of $\mu_r(r)$ and our FDFD algorithm is also applicable for these materials.

Since our averaging technique (Eqs. (2.15-2.17)) satisfies Ampere's Law everywhere across the boundary, we introduced it to reduce the possible spurious modes by finite difference scheme. Surprisingly, it is found to be very effective to improve the accuracy and convergence of the imaginary part. The same fiber is calculated again with this averaging technique and the results are shown in Fig. 8 and Table 1.

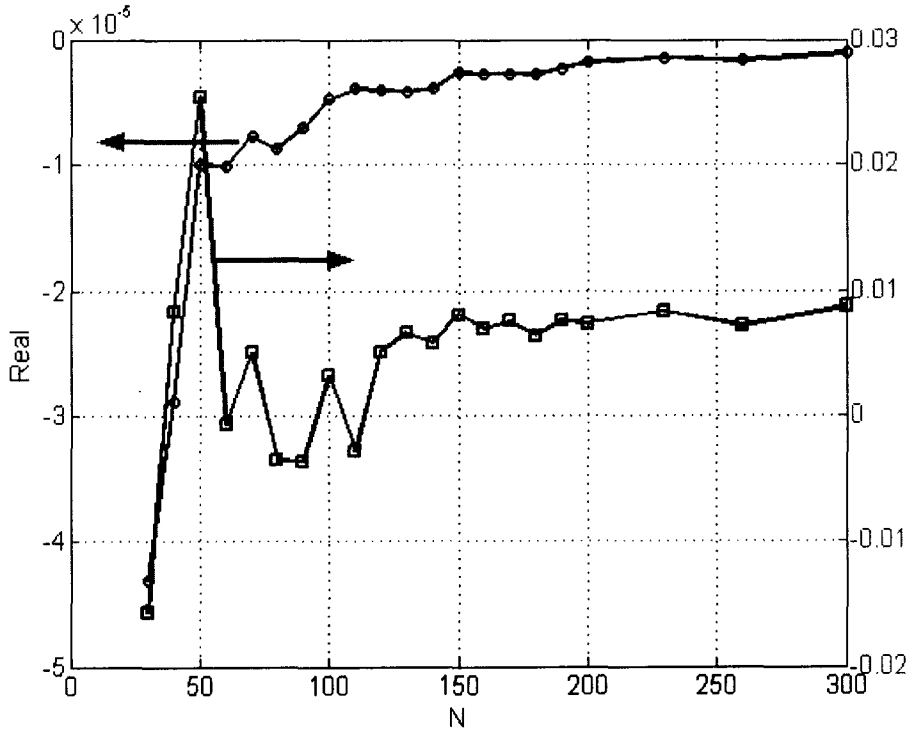

Fig. 8. The accuracy and convergence of the complex effective mode index using a more reasonable averaging technique. Note that the scale of the right y-axis is at least an order of magnitude smaller than the corresponding one in Fig. 5.

The convergence and accuracy of the real part shown in the Fig. 8 are similar to those in Fig. 5 which was obtained using the previous averaging technique. However, the convergence and the accuracy of the imaginary part are increased at least by one order of magnitude, with an error of 2% for a very coarse 30×30 mesh. The accuracy can be 10^{-3} for a moderately fine mesh.

Table 1. Calculated mode index of the fundamental mode. The accurate value is $1.445395345 + 3.15\times10^{-8}i$ (by multipole method in [41])

N	Real	Imaginary	N	Real	Imaginary
30	1.4453331	3.101×10^{-8}	140	1.4453896	3.169×10^{-8}
40	1.4453537	3.176×10^{-8}	150	1.4453915	3.176×10^{-8}
50	1.4453810	3.230×10^{-8}	160	1.4453914	3.172×10^{-8}
60	1.4453807	3.148×10^{-8}	170	1.4453914	3.174×10^{-8}
70	1.4453841	3.166×10^{-8}	180	1.4453913	3.170×10^{-8}
80	1.4453827	3.139×10^{-8}	190	1.4453920	3.174×10^{-8}
90	1.4453852	3.139×10^{-8}	200	1.4453927	3.173×10^{-8}
100	1.4453884	3.160×10^{-8}	230	1.4453932	3.177×10^{-8}
110	1.4453897	3.141×10^{-8}	260	1.4453929	3.173×10^{-8}
120	1.4453895	3.166×10^{-8}	300	1.4453937	3.178×10^{-8}
130	1.4453894	3.171×10^{-8}			

The converged imaginary part is still 1% larger than the accurate value, and it is due to the finite computation region. We have also varied the computation region to 1.8a and

2.0a, and the systematic error has been found reduced at the cost of increased computation.

2.2.4. Mode field

Fig. 9 shows the calculated fundamental mode and 2nd-order mode of the mode class 3 and 4 in the holey fiber. These modes are well confined by the single ring of the air holes and show the symmetries as discussed above. Once H_x and H_y (E_x and E_y) are solved, the other components can be obtained directly using Eqs. (2.4a-b).

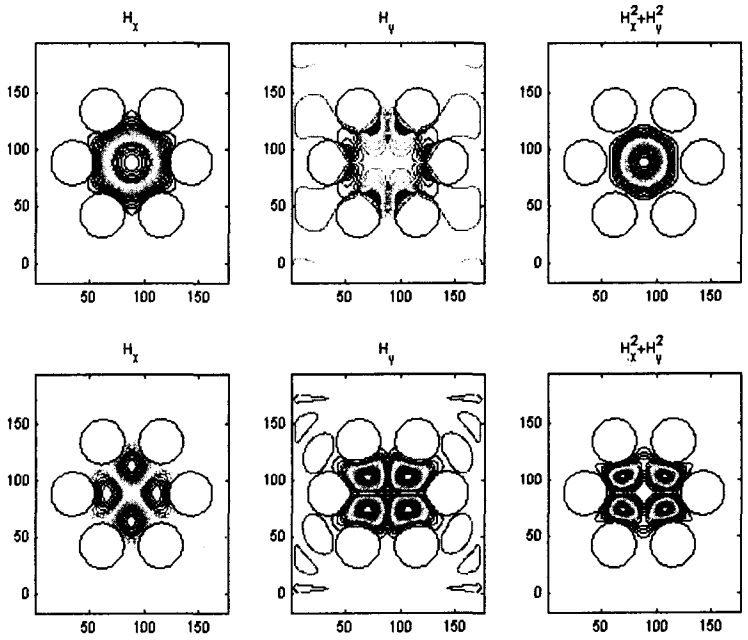

Fig. 9. The mode field patterns of the fundamental mode (top three) and 2nd-order mode (bottom three) in the degenerate mode class 3 and 4.

2.2.5. Effect of dispersive and lossy/gain materials

The effect of dispersive material on the group velocity dispersion can be easily obtained by any algorithm including this method that solves eigen-value problems for the mode propagation constants at a given wavelength. This is achieved by replacing the

dielectric constant with a wavelength dependent one. In addition, the total dispersion can be estimated using the sum of material dispersion and waveguide dispersion.

The propagation loss/gain induced by lossy/gain media is also of interest in a waveguide since it is important for long haul transmission or laser applications. The compact-2D FDFD method is also capable of solving it, and no additional work is needed except that the real dielectric constant is replaced with a complex one whose imaginary part represents the loss/gain of the media; the calculated propagation constant would reflect the material loss. To separate the leakage loss from the material loss/gain, the PML layers are removed, leaving only the zero boundaries outside the computation region. The material loss in PCF has been analyzed in [82] using the Hermite-Gauss method and here we just verify their results for a standard fiber (a=2.2μm, cladding index=1.458, core index=$1.475+in_i$ and λ=1.55μm). The results are shown in Table 2. Our FDFD is in excellent agreement with the localized function methods.

Table 2. The complex mode index with a lossy core material

n_i	10^{-5}	10^{-3}	10^{-2}
Scalar [82]	$1.465045+7.4331\times10^{-6}i$	$1.465037+7.4294\times10^{-4}i$	$1.464308+7.6918\times10^{-3}i$
Vectorial [82]	$1.464993+7.3805\times10^{-6}i$	$1.464985+7.3835\times10^{-4}i$	$1.464256+7.6446\times10^{-3}i$
FDFD	$1.464981+7.3752\times10^{-6}i$	$1.464972+7.3782\times10^{-4}i$	$1.464241+7.6398\times10^{-3}i$

2.2.6. Spurious modes

One problem encountered in our method is the introduction of spurious modes. It is known that some spurious modes are from the lack of tangential continuity for the finite difference of the curved dielectric boundaries [37]. However, we did not observe such

kind of spurious modes using our proper averaging technique. A major cause of the spurious modes in our method is the cladding modes due to the zero boundary or PML outside. Since the PML and zero boundary still reflect a very small part of energy back to the inside region, an artificial waveguide between the boundary and the air holes is formed. These modes are easily identified as spurious since they have much higher leakage loss. Fig. 10 shows the mode patterns of some spurious cladding modes obtained in our calculation. These modes are confined between the boundary and air holes and have very small power portions in the core region.

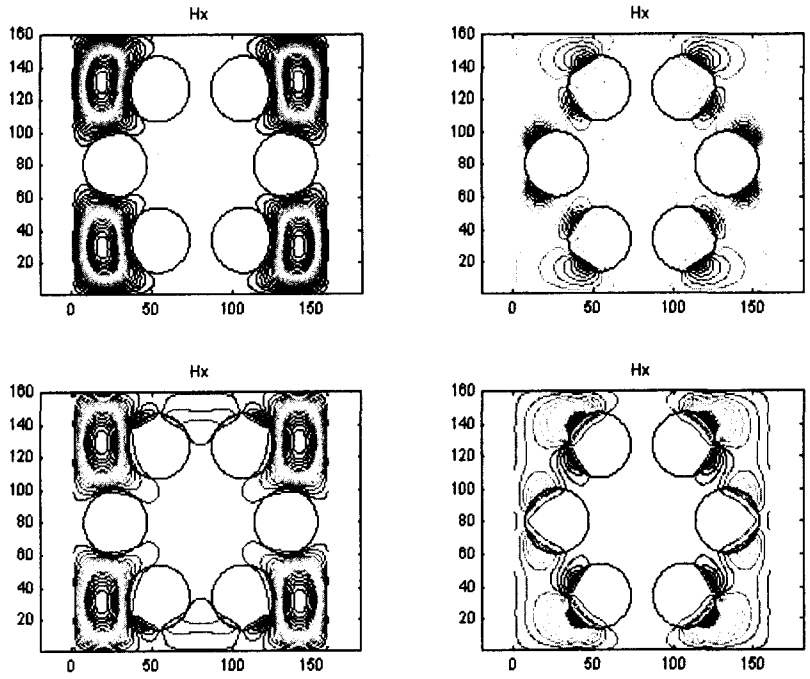

Fig. 10. Some spurious cladding modes created by the artificial waveguide between the PML + zero boundary and the air holes. These modes are weak and highly lossy.

2.3. Conclusion and discussions

In conclusion, we have used the compact-2D FDFD algorithm based on the direct solution of Maxwell's equations to analyze leakage loss by introducing the anisotropic PML layers. It is found that the curved interface should be averaged according to Ampere's Law in order to achieve a high accuracy and fast convergence in both the dispersion and leakage loss. Spurious modes are generated in the cladding area due to the artificial waveguide between the absorption boundary and the air holes. This method is highly accurate both for loss and propagation constant analysis; and both material dispersion and material loss can easily be incorporated into it.

This method is generally applicable for both index-guiding and band-gap-guiding PCFs, and not limited to PCF. But, its drawback should be pointed out that the dimension of matrices in this method is $N^2 \times N^2$, therefore the computation burden dramatically increases for large computation region. This situation happens when we investigate the loss property with the number of rings of air holes. However, the computation cost can be greatly reduced for certain type of PCF, e.g. the Bragg fiber which has circular symmetry.

CHAPTER III

MODELING OF BRAGG FIBERS

Confined modes in Bragg fibers were first analyzed by Yeh et al. [47]. Recently, these fibers have attracted much interest because of their extraordinary properties [48-52]. Low loss and tailorable dispersion have been achieved in the case of air-core Bragg fiber [54, 83]. High power guiding is possible with reduced nonlinear effects [84]. These fibers can support a truly single mode in a low-index air-core, leading to reduced absorption loss, material dispersion and nonlinear effects [48]. The guiding of light in the low-index core is due to the photonic band gap produced by the periodic cladding, instead of the total internal reflection.

To date, there is no report about using localized function method to analyze the Bragg fibers under cylindrical coordinates. This inspired us to investigate a Galerkin method suitable for this purpose. In section 3.1, we propose a full vectorial Galerkin method to treat Bragg fibers or any circular symmetric fibers with arbitrary index profile. However, we found it cannot fully solve all the problems on Bragg fibers, e.g. the loss due to the finite number of alternating cladding layers. Therefore, following the same way in the previous chapter, we study the FDFD method again for Bragg fibers under the cylinder coordinates. The details of this FDFD method are presented in section 3.2. In section 3.3, standard step index and parabolic graded-index fibers are used first to verify the validity of this method. Subsequently, losses and field distributions of several air-core Bragg fibers are analyzed and compared with the results obtained by Chew's method and TMM method; it is followed by dispersion analysis of high index core Bragg fibers with different core-index profiles. Section 3.4 provides the conclusions of the chapter.

3.1. Galerkin method

The Galerkin method is stable and accurate, which makes use of a set of orthogonal functions to approximate the guiding modes. In Ref. [85-88], the Galerkin method is used to solve the scalar wave equation for circular fibers with low index contrast. When index contrast is high, a full-vector treatment is needed.

3.1.1. Formulation

The full-vector Helmholtz wave equations for transverse fields under cylindrical coordinate can be expressed as [89]:

$$\nabla_t^2 E_r - \frac{2}{r^2}\frac{\partial E_\phi}{\partial \phi} + \frac{\partial}{\partial r}\left\{E_r \frac{d\ln n^2}{dr}\right\} - \frac{E_r}{r^2} + \left\{k_0^2 n^2 - \beta^2\right\}E_r = 0 \tag{3.1a}$$

$$\nabla_t^2 E_\phi + \frac{1}{r}\left\{\frac{d\ln n^2}{dr} + \frac{2}{r}\right\}\frac{\partial E_r}{\partial \phi} - \frac{E_\phi}{r^2} + \left\{k_0^2 n^2 - \beta^2\right\}E_\phi = 0 \tag{3.1b}$$

$$\nabla_t^2 H_r - \frac{2}{r^2}\frac{\partial H_\phi}{\partial \phi} - \frac{H_r}{r^2} + \left\{k_0^2 n^2 - \beta^2\right\}H_r = 0 \tag{3.1c}$$

$$\nabla_t^2 H_\phi - \frac{1}{r}\frac{d\ln n^2}{dr}\frac{\partial}{\partial r}\left(rH_\phi\right) + \frac{1}{r}\left\{\frac{d\ln n^2}{dr^2} + \frac{2}{r}\right\}\frac{\partial H_r}{\partial \phi} - \frac{H_\phi}{r^2} + \left\{k_0^2 n^2 - \beta^2\right\}H_\phi = 0 \tag{3.1d}$$

Guiding modes in circular symmetric fibers are classified as TE, TM, HE and EH modes. Equations given above can be simplified for TE and TM modes since they have only (H_z, H_r, E_ϕ) and (E_z, E_r, H_ϕ) components respectively. The hybrid HE and EH modes are not considered here.

For TE modes, $E_\phi(r,\phi) = f(r)$ and Eq. (3.1b) becomes:

$$\frac{d^2 f}{dr^2} + \frac{1}{r}\frac{df}{dr} + \left(k_0^2 n^2 - \beta^2 - \frac{1}{r^2}\right)f = 0 \tag{3.2}$$

For TM modes, $H_\phi(r,\phi) = g(r)$ and Eq. (3.1d) becomes:

$$\frac{d^2g}{dr^2}+\frac{1}{r}\frac{dg}{dr}+\left(k_0^2n^2-\beta^2-\frac{1}{r^2}\right)g-\frac{d\ln n^2}{dr}\left(\frac{dg}{dr}+\frac{1}{r}g\right)=0 \tag{3.3}$$

The fiber is assumed to have an infinite uniform cladding, where all fields of guiding modes vanish in the region far away from the core. Since all fields of guiding modes are finite everywhere and zero when $r\to\infty$, the mode fields can be approximated using a set of decaying orthogonal functions. This method is similar to Fourier transformation of the field, and our task here is to find the coefficients of each harmonic.

We assume that the core radius is a (from the origin to the cladding), and the core includes all microstructures. The index profile of the fiber is n(r). The refractive indices of the core and cladding are n_{co} and n_{cl} (n_{co} could be chosen arbitrarily if the core has micro-structures).

We define a dimensionless parameter:

$$x=\sigma r^2/a^2, \tag{3.4}$$

where σ is an arbitrary positive number, which affects the convergence, accuracy and computation time. In our computation, σ is chosen to be a. Also, we define normalized profile function h(r), V number and normalized propagation constant b:

$$h(r)=\frac{n^2(r)-n_{cl}^2}{n_{co}^2-n_{cl}^2},\ V^2=k_0^2a^2\left(n_{co}^2-n_{cl}^2\right),\ b=\frac{(\beta/k_0)^2-n_{cl}^2}{n_{co}^2-n_{cl}^2} \tag{3.5}$$

V^2 could be negative if n_{co} is chosen to be less than n_{cl}. h(r) is always zero in the cladding region. Inserting both Eqs. (3.4) and (3.5) into Eqs. (3.2) and (3.3), we get:

$$x\frac{d^2f}{dx^2}+\frac{df}{dx}+\frac{1}{4}\left\{\frac{V^2h-V^2b}{\sigma}-\frac{1}{x}\right\}f=0 \tag{3.6}$$

$$x\frac{d^2g}{dx}+\frac{dg}{dx}+\frac{1}{4}\left\{\frac{V^2h-V^2b}{\sigma}-\frac{1}{x}\right\}g-\frac{d\ln n^2}{dx}\left\{x\frac{dg}{dx}+\frac{1}{2}g\right\}=0 \tag{3.7}$$

Expanding the mode fields using orthogonal m^{th} order (m=1 for TE/TM modes) associated Laguerre-Gauss functions [90],

$$f(x)=\sum_{i=0}^{N-1}a_i\varphi_i(x),\ g(x)=\sum_{i=0}^{N-1}b_i\varphi_i(x) \tag{3.8}$$

where φ(x) is the Laguerre-Gauss function, N is the number of Laguerre-Gauss functions used.

Using the derivative and recurrence relation of Laguerre functions, Eq. (3.6) becomes:

$$\frac{\sigma}{V^2}\sum_{i=0}^{N-1}a_i[x-2(1+2i+m)]\varphi_i(x)+\sum_{i=0}^{N-1}a_i h\left(\sqrt{x/\sigma}\right)\varphi_i(x)=b\sum_{i=0}^{N-1}a_i\varphi_i(x) \tag{3.9}$$

Multiplying both sides of Eq. (3.9) by $\varphi_j(x)$ and integrating in the whole space from 0 to ∞, Eq. (3.9) forms a standard eigen-value problem **[M][A]=b[A]**, where **[A]** is the coefficient vector and **[M]** is a square matrix with a dimension of $N\times N$.

The infinite integration can be evaluated analytically using the orthogonality of Laguerre-Gauss functions. We only need to calculate the finite integration of $\int_0^{\sigma}h\varphi_i\varphi_j dx$.

For TE mode, $[\mathbf{M}]=[\mathbf{M}_1]+[\mathbf{N}_1]$, and the matrix elements are given as below:

$$M_1(i,i)=-\frac{\sigma}{V^2}[(2i+m+1)] \tag{3.10}$$

$$M_1(i+1,i)=-\frac{\sigma}{V^2}\sqrt{(i+1)(i+m+1)} \tag{3.11}$$

$$M_1(i-1,i)=-\frac{\sigma}{V^2}\sqrt{i(i+m)} \tag{3.12}$$

$$N_1(i,j)=\int_0^{\sigma}h\left(\sqrt{x/\sigma}\right)\varphi_i\varphi_j dx \tag{3.13}$$

For TM modes, the term in Eq. (3.7) relating to $d\ln n^2/dx$ will become a finite integration from 0 to σ. For step-index profiles, the integration becomes summations at the interfaces. In that case, $[\mathbf{M}]=[\mathbf{M}_1]+[\mathbf{N}_1]+[\mathbf{N}_2]$, and $[\mathbf{N}_2]$ is given as below:

$$N_2(i,j)=-\frac{4\sigma}{V^2}\sum_{x_j}\Delta\ln n^2\left\{\frac{2i+m+1-x}{2}\varphi_i-\sqrt{i(i+m)}\varphi_{i-1}\right\}\varphi_j\Big|_{x=x_j} \tag{3.14}$$

where x_j indicates the locations of interfaces where index changes abruptly, and $\Delta\ln n^2$ is the difference of $\ln n^2$ at the interfaces.

3.1.2. Step-index fibers

First, we verify our method using standard step-index fibers since their analytical solutions are available [89]. For a fiber with low index contrast, we use these parameters: n_{co}= 1.455556, n_{cl}=1.450745, a=4.0μm, λ=1.0μm. For a fiber with high index contrast, these parameters are used: n_{co}=2.0, n_{cl}=1.0, a=4.0μm, λ=1.0μm. The values of normalized propagation constants *b* as defined in Eq. (3.5) obtained by both analytical and Galerkin methods (N=100) are listed in Table 3.

Table 3. Normalized propagation constant b for two step-index fibers with low and high index contrast.

	Analytical	Galerkin	Relative error
TE: Low index constrast	0.169538	0.169553	8.8476×10^{-5}
TE: High index contrast	0.992596	0.992488	-1.0881×10^{-4}
TM: Low index contrast	0.168882	0.168958	4.5002×10^{-4}
TM: High index contrast	0.992341	0.992313	-2.8216×10^{-5}

As seen from the table, the Galerkin method gives quite accurate normalized propagation constants. A larger N gives more accurate results, but there is a tradeoff

between the accuracy and computation time. The fields obtained by Galerkin and analytical methods are shown in Fig. 11 for both TE and TM modes and they also have an excellent agreement with the analytical results.

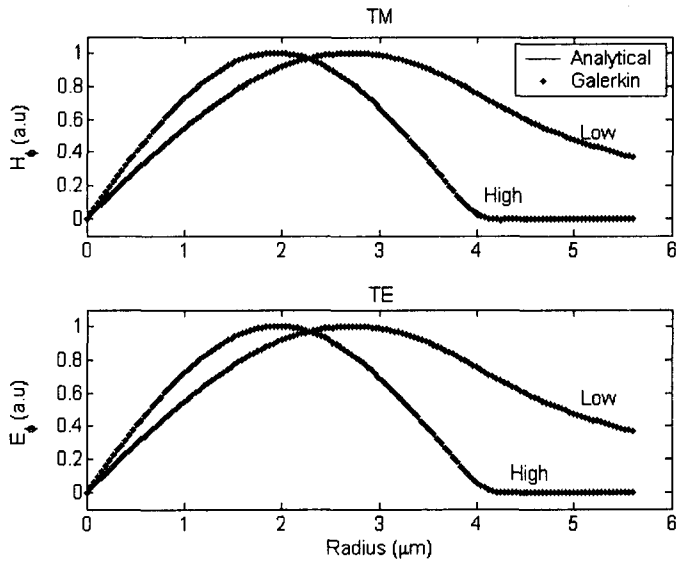

Fig. 11. Fields E_ϕ and H_ϕ of TE_{01} and TM_{01} respectively in two standard step index fibers with low and high index contrast (N=100).

3.1.3. Bragg fibers

Second, we apply our method to analyze the Bragg fiber discussed in Ref.[51]. It has an air core with a radius of 1.0μm, and the cladding consists of periodic alternate layers, with indices n_1=3.0 and n_2=1.5, thicknesses l_1=0.130μm and l_2=0.265μm. The effective indices of confined modes of the Bragg structure are in the range of [0,1]. In our calculation, the core includes the air hole and several periods of alternate layers. An imaginary cladding with a refractive index close to zero outside the core is added to terminate the alternate layers and form an index-guiding waveguide for modes with n_{eff}>0. The true Bragg modes are little affected since the fields are close to zero at the

imaginary cladding and they decay inside it. In Fig. 12, the dispersion curves for TE modes and the mode field E_ϕ of TE_{01} at 1.55μm are shown with 8 periods of alternate layers. Both the dispersion curves and the mode field agree well with the results in Ref. [51] obtained by asymptotic method. The radiation modes as shown in Fig. 12 exist since they are confined by the imaginary cladding. When the number of layers increases in a fiber with microstructures, it generally takes more time to analyze since a larger N is required to reach convergence. The total calculation time is about 5 minutes for N~200 on a PIII 500MHz computer for this example.

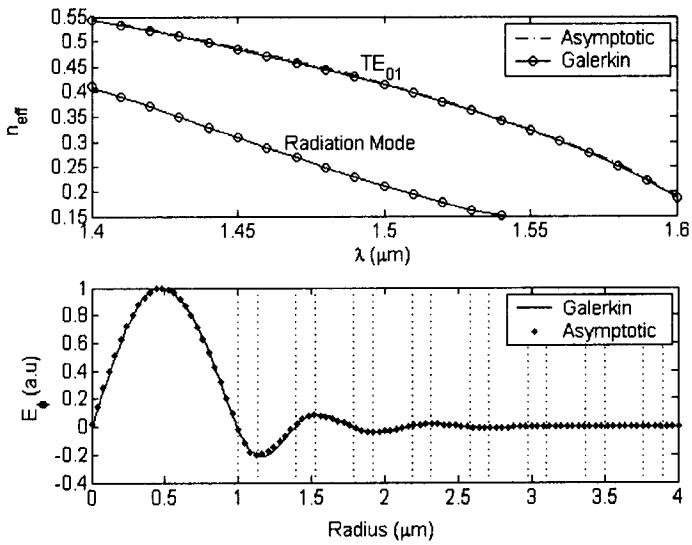

Fig. 12. The effective indices n_{eff} of TE modes in a Bragg fiber and the field E_ϕ of TE_{01} mode at λ=1.55μm (N=200).

In conclusion, we have developed a full vectorial approach based on Galerkin method to solve circular symmetric fibers with arbitrary index profiles, including the Bragg fibers. Excellent agreement is achieved for both simple geometry (step-index fiber) and complex geometry (Bragg fibers). The dimension of the matrices involved in the

calculation is N×N other than $N^2 \times N^2$ in the FDFD method described in the previous chapter. This reduces the memory requirement. However, on the other hand, to achieve high accuracy for a Bragg fiber with a large number of layers, a large N is needed. Although the important modes in Bragg fibers are TE modes, the solution of EH and HE modes should be included in the future for complete analysis.

3.2. Why 1D FDFD method?

The Galerkin method shown in the last section is accurate on dispersion analysis, but it does not provide any information on the loss property of a Bragg fiber. To include the loss analysis and overcome the drawbacks of TMM mentioned in the overview section in Chapter I, I propose a FDFD method combining the PML technique in the following sections. It is based on solving eigen-value problems which is similar to that shown in the last chapter. It is suitable for Bragg fibers with arbitrary index profiles. Compared to FDTD method, the FDFD method does not require the initial fields and time iterations. Material absorption and dispersion can be introduced easily into the FDFD method. Moreover, a batch of modes can be analyzed in a single run.

The FDFD method has been shown to be as a mode solver with high accuracy and efficiency for photonic crystal fiber characterization in Chapter II. It is also efficient for band gap structure analysis [66, 91] which will be shown in Chapter IV. However, for circular waveguides with radially dependent indices, the 2D FDFD method is not efficient. Especially for Bragg fibers, the 2D FDFD method requires huge memory to deal with a moderate computation region. By employing the symmetry property in cylindrical coordinates, the mode analysis for the Bragg fiber can be reduced to a quasi-1D problem that can be solved more efficiently and accurately. In Ref. [92], Su et. al.

proposed another finite difference method to calculate the propagation constants and cutoff frequencies of optical fibers with arbitrary permittivity profiles. An outgoing cylindrical wave was exploited as boundary in the outer homogeneous cladding just as in the case of TMM and Chew's method. In the inner region, the vectorial wave equations were discretized in the equally spaced grids. A matrix equation was obtained for the fields on those grids. The final coefficient matrix is a function of propagation constant or wavelength, and the matrix equation is not in eigenvalue form. Therefore, an iterative search for zeros is needed to get the propagation constants for given wavelength or the wavelengths for given propagation constant.

To analyze the loss property, several different open boundary conditions are used in numerical calculations: outgoing wave in the uniform cladding [44, 53, 92], transparent boundary condition [93], and perfectly matched layer (PML) technique [94-96]. Anisotropic PML technique [79] has been introduce to full vetorial 2D modal solvers based on finite element method [94] and FDFD method [95] in Cartesian coordiants. In Ref [96], a PML layer with constant conductivity was applied around a step index fiber. With the complex coordinates stretching method [74, 78], the complex propagation constants could be calculated by solving the characteristic equations under complex cylindrical coordinates. But it has the same limitation as TMM and Chew's method. In the following sections, we introduce the anisotropic PML into 1D FDFD method in cylindrical coordinates to deal with arbitrary dielectric constant profiles. The loss due to the finite number of Bragg layers is analyzed without additional algorithm complexity by doing the finite differences directly in complex coordinates.

3.3. 1D FDFD formulation

Let us consider the rotational symmetry of the waveguide with dielectric profile $\varepsilon_r = \varepsilon_r(r)$. All the guiding modes have the form of $\xi = \xi(r)\exp[j(m\phi + \beta z - \omega t)]$. ($\xi$ is any component of the electric or magnetic field: E_r, E_ϕ, E_z, H_r, H_ϕ and H_z, m is the angular quantum number, β is the propagation constant, and ε_r is the relative dielectric constant which is radially dependent.) The Maxwell's curl equations in cylindrical coordinates can be expressed as:

$$-jk_0\varepsilon_r e_r = jmh_z - j\beta h_\phi \tag{3.15a}$$

$$-jk_0\varepsilon_r e_\phi = -r\frac{\partial h_z}{\partial r} + j\beta h_r \tag{3.15b}$$

$$-jk_0\varepsilon_r e_z = \frac{1}{r}\frac{\partial h_\phi}{\partial r} - \frac{jm}{r^2}h_r \tag{3.15c}$$

$$jk_0 h_r = jme_z - j\beta e_\phi \tag{3.15d}$$

$$jk_0 h_\phi = -r\frac{\partial e_z}{\partial r} + j\beta e_r \tag{3.15e}$$

$$jk_0 h_z = \frac{1}{r}\frac{\partial e_\phi}{\partial r} - \frac{jm}{r^2}e_r \tag{3.15f}$$

and

$$e_r = rE_r(r)\Big/\sqrt{\mu_0/\varepsilon_0}\,,\ e_\phi = rE_\phi(r)\Big/\sqrt{\mu_0/\varepsilon_0}\,,\ e_z = E_z(r)\Big/\sqrt{\mu_0/\varepsilon_0} \tag{3.16a}$$

$$h_r = rH_r(r)\,,\ h_\phi = rH_\phi(r)\,,\ h_z = H_z(r) \tag{3.16b}$$

where $\sqrt{\mu_0/\varepsilon_0}$ is the free space impedance and k_0 is the wave number in free space.

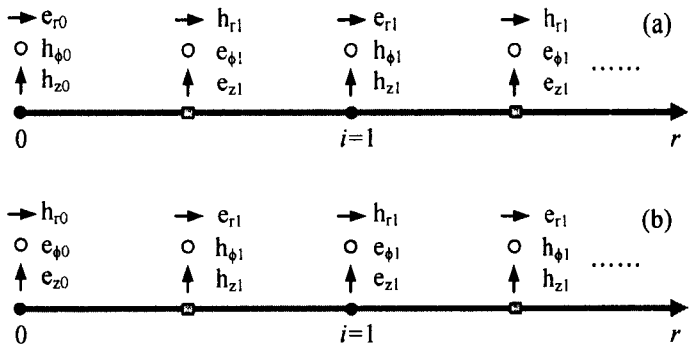

Fig. 13. Yee's 1D lattice in cylindrical coordinates. (a) For hybrid and TM modes, (b) For hybrid and TE modes.

The Eqs. (3.15a) – (3.15f) can be discretized by using 1-D Yee-cell as shown in Fig. 13a to yield:

$$-jk_0\varepsilon_{rr}(i)e_{rr}(i) = jmh_z(i) - j\beta h_\phi(i) \tag{3.17a}$$

$$-jk_0\varepsilon_{r\phi}(i)e_\phi(i) = -\frac{r_i}{\Delta}[h_z(i) - h_z(i-1)] + j\beta h_r(i) \tag{3.17b}$$

$$-jk_0\varepsilon_{rz}(i)e_z(i) = \frac{1}{r_i\Delta}[h_\phi(i) - h_\phi(i-1)] - \frac{jm}{r_i^2}h_r(i) \tag{3.17c}$$

$$jk_0h_r(i) = jme_z(i) - j\beta e_\phi(i) \tag{3.17d}$$

$$jk_0h_\phi(i) = -\frac{r_{i+0.5}}{\Delta}[e_z(i+1) - e_z(i)] + j\beta e_r(i) \tag{3.17e}$$

$$jk_0h_z(i) = \frac{1}{r_{i+0.5}\Delta}[e_\phi(i+1) - e_\phi(i)] - \frac{jm}{r_{i+0.5}^2}e_r(i) \tag{3.17f}$$

where $r_i = (i-0.5)\Delta$, and Δ is the cell size.

Writing Eqs. (3.17a) – (3.17f) in matrix form, we get

$$\begin{bmatrix} e_r \\ e_\phi \\ e_z \end{bmatrix} = -\frac{1}{jk_0}\begin{bmatrix} \varepsilon_{rr}^{-1} & 0 & 0 \\ 0 & \varepsilon_{r\phi}^{-1} & 0 \\ 0 & 0 & \varepsilon_{rz}^{-1} \end{bmatrix}\begin{bmatrix} 0 & -j\beta I & jmI \\ j\beta I & 0 & -V_z \\ -jm\Phi & V_\phi & 0 \end{bmatrix}\begin{bmatrix} h_r \\ h_\phi \\ h_z \end{bmatrix} \tag{3.18a}$$

$$\begin{bmatrix} h_r \\ h_\phi \\ h_z \end{bmatrix} = \frac{1}{jk_0} \begin{bmatrix} 0 & -j\beta I & jmI \\ j\beta I & 0 & -U_z \\ -jm\Theta & U_\phi & 0 \end{bmatrix} \begin{bmatrix} e_r \\ e_\phi \\ e_z \end{bmatrix} \tag{3.18b}$$

where I is the square identity matrix. All other matrices will be explained later when we discuss the applied boundary conditions.

After some algebraic operation, we obtain the eigen-value problems for transverse fields:

$$\begin{bmatrix} Q_{rr} & Q_{r\phi} \\ Q_{\phi r} & Q_{\phi\phi} \end{bmatrix} \begin{bmatrix} h_r \\ jh_\phi \end{bmatrix} = \beta^2 \begin{bmatrix} h_r \\ jh_\phi \end{bmatrix} \tag{3.19a}$$

$$\begin{bmatrix} P_{rr} & P_{r\phi} \\ P_{\phi r} & P_{\phi\phi} \end{bmatrix} \begin{bmatrix} e_r \\ je_\phi \end{bmatrix} = \beta^2 \begin{bmatrix} e_r \\ je_\phi \end{bmatrix} \tag{3.19b}$$

where:

$$Q_{rr} = k_0^2\varepsilon_{r\phi} - m^2\varepsilon_{r\phi}\varepsilon_{rz}^{-1}\Phi + V_zU_\phi - m^2k_0^{-2}V_zU_\phi\varepsilon_{rz}^{-1}\Phi + m^2k_0^{-2}V_z\Theta U_z\varepsilon_{rz}^{-1}\Phi \tag{3.20a}$$

$$Q_{\phi\phi} = k_0^2\varepsilon_{rr} + \varepsilon_{rr}U_z\varepsilon_{rz}^{-1}V_\phi - m^2\Theta + m^2k_0^{-2}U_\phi\varepsilon_{rz}^{-1}V_\phi - m^2k_0^{-2}\Theta U_z\varepsilon_{rz}^{-1}V_\phi \tag{3.20b}$$

$$Q_{r\phi} = -m\varepsilon_{r\phi}\varepsilon_{rz}^{-1}V_\phi - mk_0^{-2}V_zU_\phi\varepsilon_{rz}^{-1}V_\phi + mV_z\Theta + mk_0^{-2}V_z\Theta U_z\varepsilon_{rz}^{-1}V_\phi \tag{3.20c}$$

$$Q_{\phi r} = m\varepsilon_{rr}U_z\varepsilon_{rz}^{-1}\Phi - m^3k_0^{-2}\Theta U_z\varepsilon_{rz}^{-1}\Phi - mU_\phi + m^3k_0^{-2}U_\phi\varepsilon_{rz}^{-1}\Phi \tag{3.20d}$$

$$P_{rr} = k_0^2\varepsilon_{rr} - m^2\Theta + U_z\varepsilon_{rz}^{-1}V_\phi\varepsilon_{rr} - m^2k_0^{-2}U_z\varepsilon_{rz}^{-1}V_\phi\Theta + m^2k_0^{-2}U_z\varepsilon_{rz}^{-1}\Phi V_z\Theta \tag{3.20e}$$

$$P_{\phi\phi} = k_0^2\varepsilon_{r\phi} + V_zU_\phi - m^2\varepsilon_{rz}^{-1}\Phi\varepsilon_{r\phi} + m^2k_0^{-2}\varepsilon_{rz}^{-1}V_\phi U_\phi - m^2k_0^{-2}\varepsilon_{rz}^{-1}\Phi V_zU_\phi \tag{3.20f}$$

$$P_{r\phi} = -mU_\phi - mk_0^{-2}U_z\varepsilon_{rz}^{-1}V_\phi U_\phi + mU_z\varepsilon_{rz}^{-1}\Phi\varepsilon_{r\phi} + mk_0^{-2}U_z\varepsilon_{rz}^{-1}\Phi V_zU_\phi \tag{3.20g}$$

$$P_{\phi r} = mV_z\Theta - m\varepsilon_{rz}^{-1}V_\phi\varepsilon_{rr} + m^3k_0^{-2}\varepsilon_{rz}^{-1}V_\phi\Theta - m^3k_0^{-2}\varepsilon_{rz}^{-1}\Phi V_z\Theta \tag{3.20h}$$

3.3.1. Boundary at r = 0

For hybrid modes (m≠0), according to the definitions in Eqs. (3.16), all four transverse components (e_r, e_ϕ, h_r, and h_ϕ) vanish at r = 0. Also from Eqs. (3.15a) and

(3.15d), h_z and e_z must be zero at the same point. Therefore, all the six components satisfy the zero boundary conditions at r = 0.

For TM (TE) modes (m=0), only h_ϕ, e_r, and e_z (e_ϕ, h_r, and h_z) need be considered. The transverse components (h_ϕ of TM and e_ϕ of TE modes) vanish. Again from Eqs. (3.15a) and (3.15d), the z components (e_z of TM and h_z of TE mode) could have nonzero values at the origin. Therefore, the lattice should be arranged in such a way that the transverse components are located at r = 0 to satisfy the zero boundary conditions. The lattice in Fig. 13a is suitable for TM mode analysis. In order to analyze TE mode, half a cell should be shifted to let e_ϕ be located at r = 0 as shown in Fig 13b. The equations for P and Q for the TE modes can be obtained by doing the exchanges: U↔V and Θ↔Φ in Eqs. (3.22). Obviously, for m=0, the Eqs. (3.19a) and (3.19b) are reduced to:

$$Q_{\phi\phi} h_\phi = \beta^2 h_\phi, \quad P_{\phi\phi} e_\phi = \beta^2 e_\phi \tag{3.21}$$

for TM and TE modes.

The point at r=0 is treated as a boundary in this method, hence the nonzero components at r=0 cannot be calculated. However, they can be readily evaluated by Gauss's law using the values of neighboring components [97, 98].

3.3.2. Closed boundary condition and effective index media

We can simply close the computation region with a perfectly conducting wall. Those matrices with dimension of N×N in Eqs. (3.18a) and (3.18b) are defined as follows (N is the total number of cells.):

$$\Phi = R_l^{-2}, \quad V_z = R_l V, \quad V_\phi = R_l^{-1} V \tag{3.22a}$$

$$\Theta = R_{l+0.5}^{-2}, \quad U_z = R_{l+0.5} U, \quad U_\phi = R_{l+0.5}^{-1} U \tag{3.22b}$$

where,

$$R_I(i,j) = r_i \delta_{ij},\ R_{I+0.5}(i,j) = r_{i+0.5}\delta_{ij}$$

$$U(i,j) = \frac{1}{\Delta}\left(\delta_{i,j-1} - \delta_{ij}\right),\ V(i,j) = \frac{1}{\Delta}\left(\delta_{ij} - \delta_{i,j+1}\right). \tag{3.22c}$$

The permittivity matrices are diagonal:

$$\varepsilon_{rrij} = \varepsilon_{rr}(i)\delta_{ij},\ \varepsilon_{r\phi_{ij}} = \varepsilon_{r\phi}(i)\delta_{ij},\ \varepsilon_{rzij} = \varepsilon_{rz}(i)\delta_{ij} \tag{3.22d}.$$

For a cell including two different materials with dielectric constants ε_a and ε_b, the effective permittivity is calculated as $\varepsilon = f_a \times \varepsilon_a + (1-f_a) \times \varepsilon_b$ for tangential components e_ϕ and e_z and $\varepsilon = \varepsilon_a \times \varepsilon_b / [f_a \times \varepsilon_b + (1-f_a) \times \varepsilon_a]$ for normal component e_r according to the effective-medium theory [99], where f_a is the filling ratio.

3.3.3. Open boundary

To analyze the leakage loss of Bragg fiber, an anisotropic PML layer [79] is used to absorb all the outgoing radiation. The PML boundary was applied in cylindrical coordinates as in Ref. [98]. Here, to keep the formula general for both the closed and open boundary conditions, we use the complex coordinate stretching method [74, 78] by defining a complex radial variable

$$\tilde{r} = \int_0^r s_r(r')dr' = \begin{cases} r & r \le r_p \\ r + i\alpha \dfrac{(r - r_p)^{n+1}}{(n+1)r_m^n} & r > r_p \end{cases}, \tag{3.23}$$

where, α is the attenuation coefficient, r_m is thickness of PML layer, and r_p is the location of the interface between the inner region and the PML layer as shown in Fig. 14. We found that stable loss values are achieved when the attenuation coefficient α is bigger than 100. In the other extreme, α can not be too big as it can cause significant reflection. For the examples followed in this chapter, 16 PML layers are used along with $\alpha = 200$ and $n = 3$.

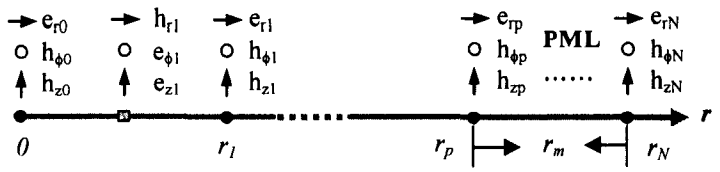

Fig. 14. Yee's lattice with open boundary.

All the formula for the closed boundary condition can be used for the open boundary condition as well by substituting r to $\tilde{r}$, and $\Delta_i = \tilde{r}_{i+0.5} - \tilde{r}_{i-0.5}$ for Eqs (3.17b-3.17c) and $\Delta_i = \tilde{r}_{i+1} - \tilde{r}_i$ for Eqs. (3.17e-3.17f).

3.4. Implementation of 1D FDFD method

3.4.1. Standard step index and graded-index fibers

First, the 1D-FDFD method is verified in the case of standard step index fiber, which has analytical result. The fiber parameters are the same as in Ref. [40]: core radius r_0 = 3μm, wavelength λ = 1.5μm, core refractive index n_{co} = 1.45 and cladding refractive index n_{cl} = 1. The computing region is $2r_0$. The effective index of fundamental mode is calculated as listed in Table 4. Using the same numbers of grids, the current method provides better results than those calculated by the other methods [40]. This is because analytical calculation is used for the derivatives in the azimuthal direction. The error comes only from the difference approximation in the radial direction. Fig. 15 shows the convergence property of this algorithm. The relative error of the order of 10^{-7} is achieved when the 140 grids are taken in the computing region.

Table 4. Calculated fundamental mode indices of a step-index fiber. The fiber parameters are: r_0 = 3μm, λ = 1.5μm, core refractive index n_{co} = 1.45 and cladding refractive index n_{cl} = 1. The analytical solution is 1.4386042.

Number of grids in computing region	Effective index (Current work)
30	1.4385851
60	1.4385982
120	1.4386026
240	1.4386038
480	1.4386041

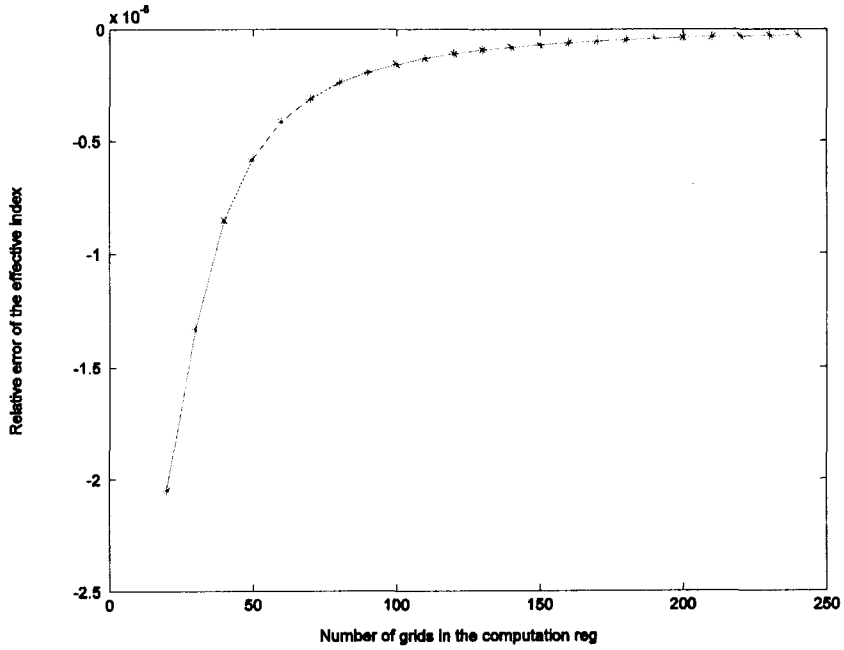

Fig. 15. Relative error vs. number of grids taken for computation.

To clarify the validity of this method to inhomogeneous index profile, we analyze a graded-index fiber with parabolic-index core: core radius r_0 = 2μm, the refractive index at the origin n_{co} = 1.45. The refractive-index distribution is given by

$$n^2(r) = \begin{cases} n_{co}^2\left[1 - 2\Delta(r/r_0)^2\right] & r \le a \\ n_{co}^2(1 - 2\Delta) & r > a \end{cases} \tag{3.24}$$

where, 2Δ =0.01 is taken for the example. The computing region is $10r_0$, and 100 points are sampled in each r_0. The calculated normalized propagation constants of the fundamental modes are in good agreement with the first-order perturbation solutions of the vector wave equation [100] as shown in table 5. V is the normalized frequency. Meanwhile, the scalar wave approximation provides appreciable errors in the low frequency region.

Table 5. Calculated normalized propagation constant of fundamental mode of graded-index fibers with parabolic-index cores. The fiber parameters are: r_0 = 2μm, refractive index in the origin n_{co} = 1.45.

V	Current work	First order perturbation vectorial solutions*	Exact scalar solutions*
2.0	0.150453	0.1505	0.2687
3.0	0.362329	0.3623	0.4025
4.0	0.506563	0.5066	0.5183
5.0	0.601524	0.6015	0.6051
6.0	0.666942	0.6669	0.6682

* The data in these two columns are taken from reference [100].

All the calculations are done in seconds on a P4 1.5GHz Pentium 4 computer. It is clear that those N×N matrices greatly reduce the computation time compared to $N^2 \times N^2$ matrices used in 2D FDFD method.

3.4.2. Air-core Bragg fibers

Next we apply the FDFD method to analyze air-core Bragg fibers that guide light due to the photonic band gap mechanism. We use the following parameters: an air core with a radius of 1.3278μm, and 16 pairs of high/low index materials. The indices of the

materials are 1.49 and 1.17, the corresponding thicknesses are 0.2133 μm and 0.346 μm. This fiber has been investigated in Ref. [101] using Chew's method [53].

The calculated effective indices and convergence with the number of grids in each thinner layer are shown in Table 6 and Fig. 16. The relative errors of the real part and the imaginary part of the effective index are of the order of 10^{-6} and 10^{-3} respectively, when 60 grids are taken for each thinner layer. Also shown in Table 6 are the calculation times on a P4 1.5G computer using this FDFD method. The N×N matrices in Eqs. (3.19) & (3.20) greatly relieve the memory burden as compared to 2D FDFD method for Bragg fiber analysis. The sparse matrix can further reduce memory requirements in the analysis of structures with large dimensions.

Table 6. Calculated effective indices of TE/hybrid modes in Bragg fibers. The effective indices calculated using Chew's method are $0.891067 + 1.4226\times10^{-8}i$ and $0.805578+1.7392\times10^{-3}i$ for TE_{01} and hybrid modes, respectively.

N*	Effective index of TE_{01} (m = 0)			Effective index of hybrid mode (m = 1)		
	Real	Imaginary	Execution time	Real	Imaginary	Execution time
15	0.891117	1.4432×10^{-8}	1.7 s	0.805781	1.7207×10^{-3}	2.3 s
20	0.891093	1.4328×10^{-8}	2.5 s	0.805672	1.7261×10^{-3}	2.6 s
30	0.891080	1.4278×10^{-8}	5.1 s	0.805623	1.7322×10^{-3}	5.2 s
60	0.891070	1.4236×10^{-8}	18.1 s	0.805583	1.7375×10^{-3}	18.8 s

* N: Number of grids in each thinner layer.

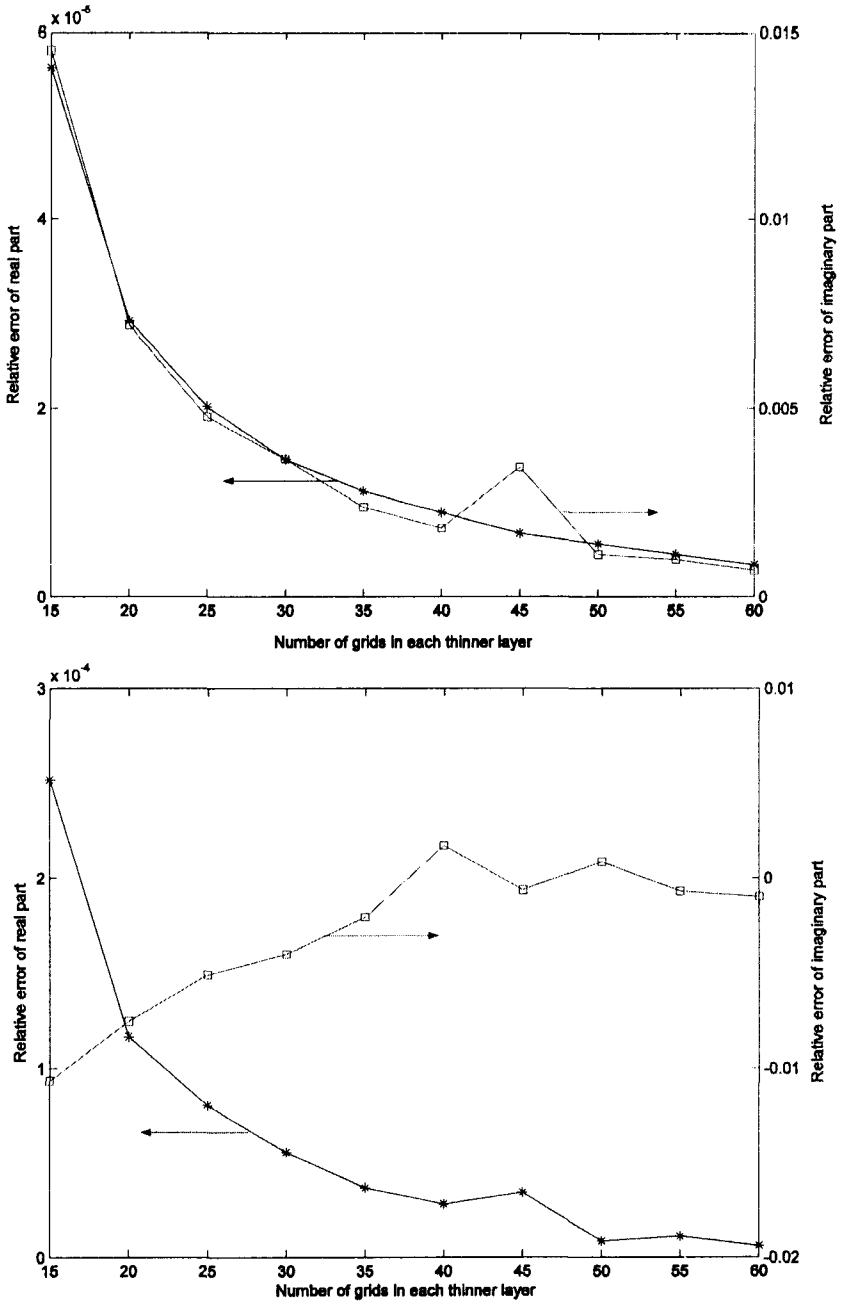

Fig. 16. Convergence property for TE_{01} (upper) mode and hybrid mode (m = 1) (bottom) calculation.

When an effective index (propagation constant) is obtained as an eigen-value, the field distribution can be deduced from the corresponding eigen-vector. As a second example, Fig. 17 shows the normalized field distribution of TE_{01} mode for the Ominiguide fiber [83]. The FDFD results agree very well with those obtained by the

transfer matrix method [44]. In Fig. 18, the normalized field distributions of hybrid modes (m = 1 and m = 4) are shown for a third Bragg fiber [54]. Both curves match the TMM results well. The mode corresponding to m = 4 has much larger oscillatory amplitude in the cladding compared to the m=1 mode. Hence, the leakage loss of the m = 4 mode is high and only the m = 1 mode will be guided farther in the fiber. Also, the effective index of the hybrid mode (m = 4) is higher than 1, implying that it is a surface mode. The field decays in both the air core and the cladding regions as shown in Fig. 18.

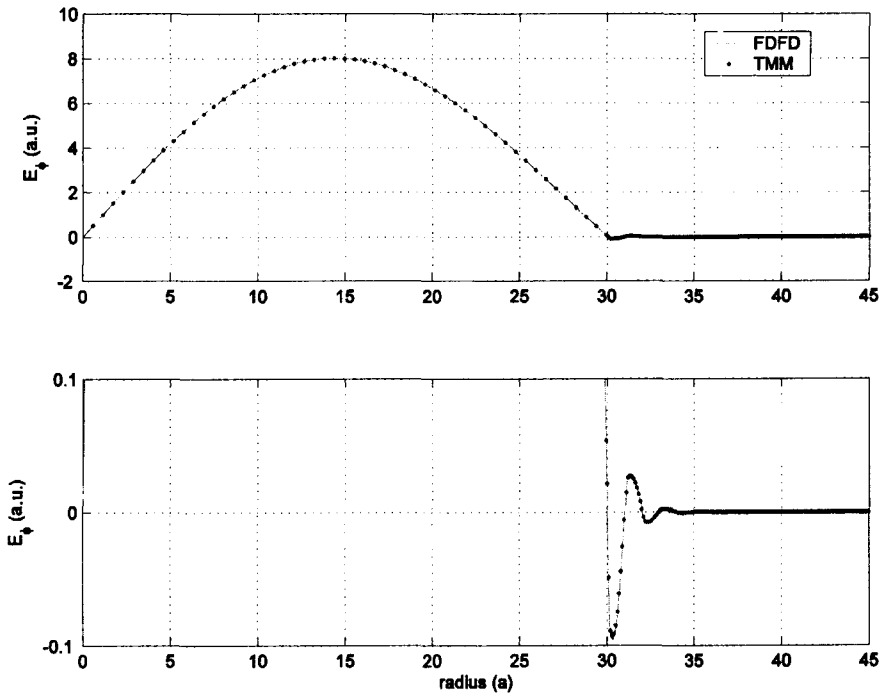

Fig. 17. Electric field distribution for TE_{01} in an OmniGuide fiber with a large air core [83]. The radius of the air core is $r = 30a$. The thicknesses of the layers with high and low indices ($n_{hi} = 4.6$, $n_{lo} = 1.6$) are $t_{hi} = 0.22a$ and $t_{lo} = 0.78a$; $a = 0.434$ μm, the wavelength $\lambda = 1.55$ μm. The bottom graph shows expanded amplitude to obtain the electric field variation in the periodic cladding. The core is surrounded by 17 layers. 140 grids are taken for each bi-layer.

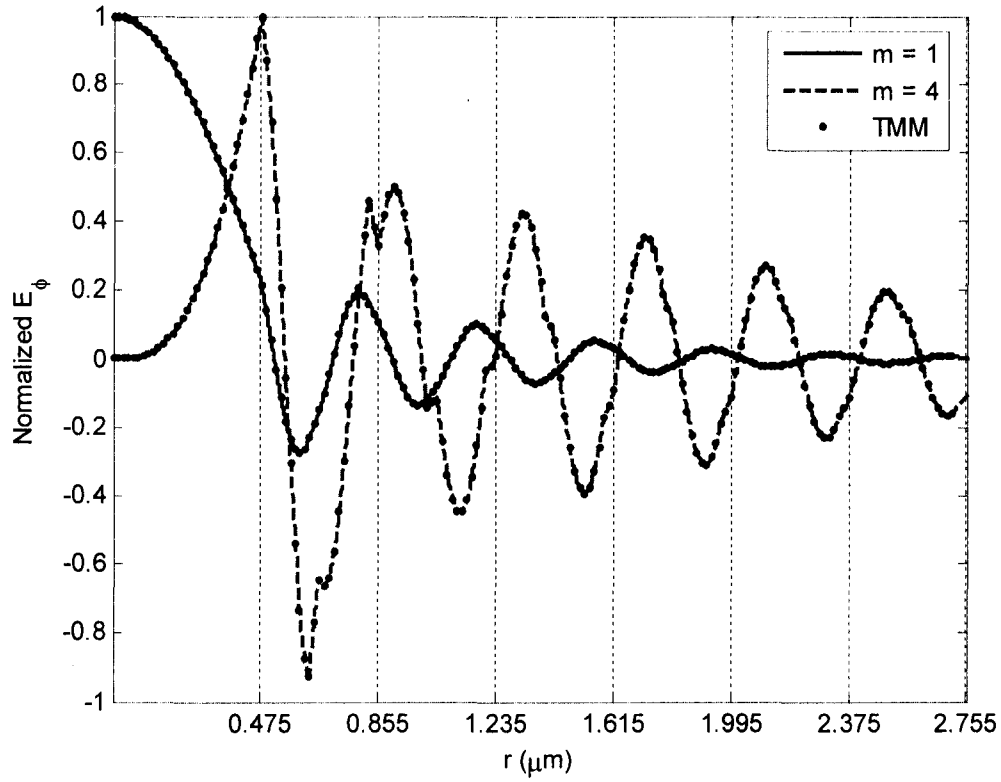

Fig. 18. Field distributions of hybrid modes m = 1 and m = 4. The parameters of this fiber are: r = 0.475 μm, λ = 1.55 μm, n_{hi} = 4.6, n_{lo} = 1.5, t_{hi} = 0.158 μm, t_{lo} = 0.032 μm [54]. The core is surrounded by 12 bi-layers. 120 grids are taken for each bi-layer. The calculated effective indices are: $0.6004 + 1.370 \times 10^{-3}i$ (m = 1) and $1.0675 + 5.753\times 10^{-2}i$ (m = 4). Computation time is about 8 s on a P4 1.5G computer.

3.4.3. High index-core Bragg fibers

Next, this method is used to analyze high-index core Bragg fibers with a number of different core index profiles. We choose the same parameters of the air-core OminiGuide fiber for the Bragg reflection layers. However, the core radius is reduced to $2a$ to expel all the higher TE modes out of the band gap except TE_{01}. The refractive index of the core has the profile

$$n(r) = n_{co}[1-(r/r_0)^{\alpha}\Delta] \tag{3.25}$$

where, r_0 (=$2a$) is the core radius, Δ is the relative index difference within the core and the refractive index at the origin n_{co} = 1.45. Fig. 19 shows the dispersion curves for

different values of Δ and α. For homogeneous core index, the FDFD and TMM results are identical as shown by the top curve in Fig. 19. When Δ increases, the dispersion curves move downward because the reduced average refractive index forces the dispersion curve to move away from the dielectric band. The same situation occurs when α changes from 2 to 1 corresponding to change in index profile from parabolic to linear. These results demonstrate a way to manipulate the dispersion curve of Bragg fibers by using different core index profiles.

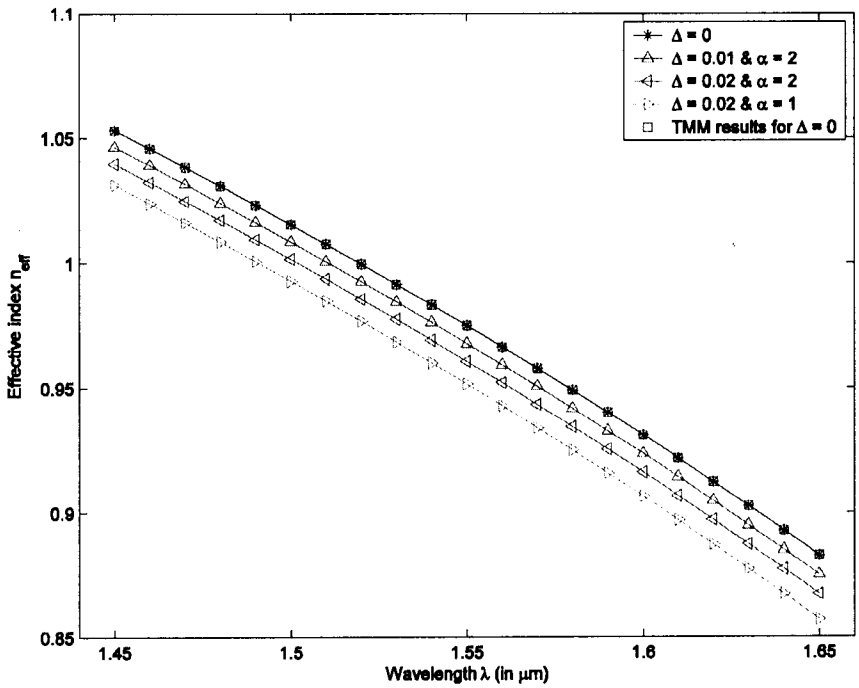

Fig. 19. Dispersion curves for high-index core Bragg fibers with different core index profile. The FDFD and TMM results are overlapped for Δ = 0 which represents the step index core.

3.5. Conclusions

In summary, we presented a Galerkin method and a FDFD method for Bragg fiber analysis. Although the Galerkin method is not suitable for loss analysis, both methods are accurate for dispersion analysis. Specially, instead of using $N^2 \times N^2$ matrices as in 2D

FDFD method, our 1-D FDFD method requires only N×N matrices. Hence, it is much more efficient to analyze the guiding mode propagation characteristics in circular waveguides, especially Bragg fibers that have radially dependent dielectric profiles. In the azimuthal direction, an analytical form is used for the derivatives in Maxwell's equations instead of the difference approximation. Hence, this method could provide slightly higher accuracy than the 2D method. The numerical examples shown in the paper verify that the compact 1D FDFD method using PML technique is accurate and suitable for propagation and loss analysis of Bragg fiber with finite number of layers.

CHAPTER IV

MODELING OF PHOTONIC BAND GAP MATERIAL

To fully understand the properties of a PBG-guiding PCF, the PBG structures of the PCF cladding needs to be determined first. PBG materials and devices have been under intense research for over a decade following the seminal papers [2, 102]. There are several methods for band structure analysis, such as the plane wave method (PWM) [103-105] and the FDTD [106-109] method. The PWM is able to provide complete and accurate information. However, the algorithm complexity is $O(N^3)$ and the computation is heavy for large problems. The order-N method based on FDTD can effectively reduce computation. It solves the Maxwell's equations within the unit cell in time-domain by applying an initial field that covers all the possible symmetries; the eigen-modes are identified as the spectral peaks from the Fourier transform of the time-variant fields. The drawback of this method is that the accuracy depends on the number of iterations. There is also a possibility of losing true eigen-mode if the corresponding peak is too small, or resolution is too low. Moreover, spurious modes may arise from spectral noise. The FDFD method has been proposed for optical waveguide analysis [38-40], which is accurate and stable. In this chapter, it is shown that this technique can be applied in photonic band gap analysis and it is worth noting that an FDFD approach using Helmholtz equation has been shown in [66].

In the first section, the standard PWM still widely used to date is introduced. Then the FDFD algorithm under generalized coordinate system is derived and applied on 2D photonic crystals with two different geometries in the second section. The accuracy, convergence, and computation time in the FDFD method are compared with those

obtained by PWM in section 4.3. In section 4.4, the out-of-plane band structure of the cladding of the photonic crystal fiber is analyzed.

4.1. PWM

The master equation widely used for PWM is for magnetic field:

$$\nabla \times \frac{1}{\varepsilon(r)} \nabla \times \vec{H}(r) = \frac{\omega^2}{c^2} \vec{H}(r) \tag{4.1}$$

This is a standard eigen-value equation $\Theta \vec{H} = \Lambda \vec{H}$ with Hermitian operator $\Theta = \nabla \times \frac{1}{\varepsilon} \nabla \times$ and eigen-value $\Lambda = \omega^2 / c^2$. For photonic crystals, the permittivity is a periodic function:

$$\varepsilon(r) = \varepsilon(r + R_l) \tag{4.2}$$

where:

$$R_l = l_1 \vec{a}_1 + l_2 \vec{a}_2 + l_3 \vec{a}_3 \tag{4.3}$$

where l_1, l_2, l_3 are integers, and $\vec{a}_1, \vec{a}_2, \vec{a}_3$ are the basis vectors in the primitive space. By applying the transverse condition

$$\nabla \bullet \vec{H}(r) = 0 \tag{4.4}$$

and Bloch theorem, we can express the H field by a modulated function:

$$\begin{aligned} \vec{H}(r) &= \sum_{\lambda=1,2} e^{i\vec{k}\bullet\vec{r}} u(r) \hat{e}_{k,\lambda} \\ u(r) &= u(r + R_l) \end{aligned} \tag{4.5}$$

where *u(r)* is a periodic function with the same period as the permittivity function, and $\hat{e}_{k,1}$ and $\hat{e}_{k,2}$ are unit vectors perpendicular to the vector $\vec{k}$ and orthogonal to each other. Taking Fourier transforms, we obtain

$$\frac{1}{\varepsilon}(r) = \sum_{\vec{G}_i} \varepsilon^{-1}(\vec{G}_i) e^{i\vec{G}_i \bullet \vec{r}} \tag{4.6}$$

$$\vec{H}(r) = \sum_{\vec{G}_i,\lambda} h(\vec{G}_i,\lambda)\hat{e}_\lambda e^{j(\vec{k}+\vec{G}_i)\vec{r}} \tag{4.7}$$

where $\varepsilon^{-1}(\vec{G}_i)$ and $h(\vec{G}_i,\lambda)$ are coefficients corresponding to $\vec{G}_i$:

$$\vec{G}_i = h_1\vec{b}_1 + h_2\vec{b}_2 + h_3\vec{b}_3 \tag{4.8}$$

where b_1, b_2, b_3 are basis vectors in the reciprocal space; h_1, h_2, h_3 are integers

$$\vec{b}_1 = 2\pi\frac{\vec{a}_2\times\vec{a}_3}{\vec{a}_1\bullet\vec{a}_2\times\vec{a}_3}, \hat{b}_2 = 2\pi\frac{\vec{a}_3\times\vec{a}_1}{\vec{a}_1\bullet\vec{a}_2\times\vec{a}_3}, \hat{b}_3 = 2\pi\frac{\vec{a}_1\times\vec{a}_2}{\vec{a}_1\bullet\vec{a}_2\times\vec{a}_3} \tag{4.9}$$

Substituting Eqs. (4.6) and (4.7) into the master Eq. (4.1), we get an eigen-value equation in an algebraic form

$$\sum_{G'}\left|\vec{k}+\vec{G}\right|\left|\vec{k}+\vec{G}'\right|\varepsilon^{-1}(\vec{G}-\vec{G}')\begin{bmatrix}\hat{e}_2\bullet\hat{e}_2' & -\hat{e}_2\bullet\hat{e}_1'\\ -\hat{e}_1\bullet\hat{e}_2' & \hat{e}_1\bullet\hat{e}_1'\end{bmatrix}\begin{bmatrix}h_1'\\ h_2'\end{bmatrix} = \frac{\omega^2}{c^2}\begin{bmatrix}h_1\\ h_2\end{bmatrix}. \tag{4.10}$$

In two-dimensional photonic crystal, *k* vector is confined in the transverse (x-y) plane, the $\hat{e}_1(\hat{e}_1')$ is always perpendicular to $\hat{e}_2'(\hat{e}_2)$, therefore, the h1 and h2 components in Eq. (4.10) decoupled into two separate sets corresponding to TM and TE modes. The corresponding eigen-value Eqs are reduced from Eq. (4.10):

TM:
$$\sum_{G'}\left|\vec{k}+\vec{G}\right|\left|\vec{k}+\vec{G}'\right|\varepsilon^{-1}(\vec{G}-\vec{G}')h_1(\vec{G}') = \frac{\omega^2}{c^2}h_1(\vec{G}) \tag{4.11}$$

TE:
$$\sum_{G'}(\vec{k}+\vec{G})\bullet(\vec{k}+\vec{G}')\varepsilon^{-1}(\vec{G}-\vec{G}')h_2(\vec{G}') = \frac{\omega^2}{c^2}h_2(\vec{G}). \tag{4.12}$$

4.2. FDFD formulation

We consider nonconductive materials under generalized coordinates denoted by three unit basis vectors $u_q(x,y,z)$ (q = 1, 2, 3). The Maxwell's curl equations in complex form can be expressed as [109, 110]:

$$\nabla_q\times\hat{H} = jk_0\hat{\varepsilon}(r)\hat{E} \quad \nabla_q\times\hat{E} = -jk_0\hat{\mu}(r)\hat{H}, \tag{4.13}$$

and the renormalized fields are:

$$\hat{E}_i = Q_i\sqrt{\varepsilon_0/\mu_0}E_i \qquad \hat{H}_i = Q_i H_i\,, \tag{4.14}$$

where k_0 is the wave vector in free space, Q_i's are the grid size along each direction. The $\hat{\varepsilon}$ and $\hat{\mu}$ are respectively the effective relative permitivity and permeability constants which are 3×3 tensors under the generalized coordinate system:

$$\hat{\varepsilon}_{ij}(r) = \varepsilon_{ri}(r)g_{ij}\left|u_1\cdot u_2\times u_3\right|\frac{Q_1Q_2Q_3}{Q_iQ_jQ_0} \qquad \hat{\mu}_{ij}(r) = \mu_{ri}(r)g_{ij}\left|u_1\cdot u_2\times u_3\right|\frac{Q_1Q_2Q_3}{Q_iQ_jQ_0}\,. \tag{4.15}$$

Q_0 is a constant introduced to be roughly equal to Qi's; $|u_1\cdot u_2\times u_3|$ is the volume of the unit cell, ε_{ri} (μ_{ri}) is the relative dielectric constant (the relative permeability constant) at the position where the electric field $\hat{E}_i$ (the magnetic field $\hat{H}_i$) is located. $\boldsymbol{g}$ is the metric tensor that can be obtained using the three unit vectors,

$$g^{-1} = \begin{bmatrix} u_1\cdot u_1 & u_1\cdot u_2 & u_1\cdot u_3 \\ u_2\cdot u_1 & u_2\cdot u_2 & u_2\cdot u_3 \\ u_3\cdot u_1 & u_3\cdot u_2 & u_3\cdot u_3 \end{bmatrix} \tag{4.16}$$

and the length in generalized coordinate can be calculated using:

$$\left|r^2\right| = \vec{r}^{\,T}\left[g^{-1}\right]\vec{r} \tag{4.17}$$

We use Yee's mesh [45] and finite difference to replace the derivates in Maxwell's curl equations [109, 110] and formulate them in matrix form using the approach described in [40]:

$$jk_0\begin{bmatrix}\hat{E}_1\\ \hat{E}_2\\ \hat{E}_3\end{bmatrix} = \begin{bmatrix}\varepsilon_{11}^{-1} & \varepsilon_{12}^{-1} & \varepsilon_{13}^{-1}\\ \varepsilon_{21}^{-1} & \varepsilon_{22}^{-1} & \varepsilon_{23}^{-1}\\ \varepsilon_{31}^{-1} & \varepsilon_{32}^{-1} & \varepsilon_{33}^{-1}\end{bmatrix}\begin{bmatrix}0 & -U_3 & U_2\\ U_3 & 0 & -U_1\\ -U_2 & U_1 & 0\end{bmatrix}\begin{bmatrix}\hat{H}_1\\ \hat{H}_2\\ \hat{H}_3\end{bmatrix}, \tag{4.18}$$

$$-jk_0\begin{bmatrix}\hat{H}_1\\ \hat{H}_2\\ \hat{H}_3\end{bmatrix} = \begin{bmatrix}\mu_{11}^{-1} & \mu_{12}^{-1} & \mu_{13}^{-1}\\ \mu_{21}^{-1} & \mu_{22}^{-1} & \mu_{23}^{-1}\\ \mu_{31}^{-1} & \mu_{32}^{-1} & \mu_{33}^{-1}\end{bmatrix}\begin{bmatrix}0 & -V_3 & V_2\\ V_3 & 0 & -V_1\\ -V_2 & V_1 & 0\end{bmatrix}\begin{bmatrix}\hat{E}_1\\ \hat{E}_2\\ \hat{E}_3\end{bmatrix}, \tag{4.19}$$

where U_i and V_i are coefficient matrices formed according to the boundary conditions, and they are proportional to $1/Q_i$.

An eigen-value problem in frequency-domain is formed for either $\hat{E}$ or $\hat{H}$ by eliminating $\hat{H}$ or $\hat{E}$ in Eqs. (4.18-4.19). For a given wave vector k, all the referred components outside the unit cell boundary can be obtained using Bloch's periodic boundary condition:

$$\hat{H}(r+R_l)=\exp(ik\cdot R_l)\hat{H}(r)\quad \hat{E}(r+R_l)=\exp(ik\cdot R_l)\hat{E}(r), \tag{4.20}$$

where R_l can be an arbitrary lattice vector, and here it is limited in the unit cell or supercell.

Two-dimensional cases

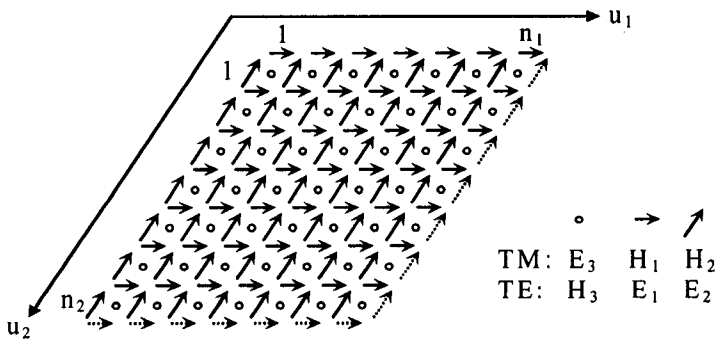

Fig. 20. Yee's 2D mesh in general coordinates. The dotted components are at the boundaries.

A 2D Yee's mesh under generalized coordinate system is shown in Fig. 20 for both TE and TM modes. E and H are arranged along two basis vectors u_1 and u_2; u_3 is coincident with the z direction. Since Q_3 is infinite, U_3 and V_3 in the equation (4.18-4.19) are zero, and simple eigen-equations can be obtained. The lattice vector R_l in Eq. (4.20) is chosen to be $a_q u_q$, and a_q is the dimension of the unit cell or supercell along direction q.

For TM modes, the eigen-equation is shown as follows:

$$k_0^2 \hat{E}_z = \varepsilon_{33}^{-1}\left\{U_1\left(\mu_{21}^{-1}V_2 - \mu_{22}^{-1}V_1\right) - U_2\left(\mu_{11}^{-1}V_2 - \mu_{12}^{-1}V_1\right)\right\}\hat{E}_z . \tag{4.21}$$

The fields E and H in the two dimensional grids are arranged row by row into column vectors. Subsequently the Bloch boundary conditions are applied to get the matrices U and V:

$$U_1 = \frac{1}{Q_1}\begin{bmatrix} -1 & 1 & & & & & & & \\ & \ddots & \ddots & & & & & & \\ u_x & & -1 & 0 & & & & & \\ & & & \ddots & \ddots & & & & \\ & & u_x & & -1 & 0 & & & \\ & & & & & -1 & \ddots & & \\ & & & & & & \ddots & 1 & \\ & & & & & u_x & & -1 & \end{bmatrix}, \quad V_1 = \frac{1}{Q_1}\begin{bmatrix} 1 & & v_x & & & & & & \\ -1 & \ddots & & & & & & & \\ & \ddots & 1 & & & & & & \\ & & 0 & 1 & & v_x & & & \\ & & & \ddots & \ddots & & & & \\ & & & & 0 & 1 & & v_x & \\ & & & & & \ddots & \ddots & & \\ & & & & & & -1 & 1 & \end{bmatrix} \tag{4.22}$$

where

$$u_x = \exp(ik \cdot a_1 u_1), \; v_x = -\exp(-ik \cdot a_1 u_1) \tag{4.23}$$

$$U_2 = \frac{1}{Q_2}\begin{bmatrix} -1 & & 1 & & & & & \\ & -1 & & 1 & & & & \\ & & \ddots & & \ddots & & & \\ & & & \ddots & & \ddots & & \\ & & & & -1 & & 1 & \\ u_y & & & & & -1 & & \\ & \ddots & & & & & \ddots & \\ & & u_y & & & & & -1 \end{bmatrix}, \quad V_2 = \frac{1}{Q_2}\begin{bmatrix} 1 & & -1 & & & & & \\ & 1 & & -1 & & & & \\ & & \ddots & & \ddots & & & \\ & & & \ddots & & \ddots & & \\ & & & & 1 & & -1 & \\ v_y & & & & & 1 & & \\ & \ddots & & & & & \ddots & \\ & & v_y & & & & & 1 \end{bmatrix} \tag{4.24}$$

where

$$u_y = \exp(ik \cdot a_2 u_2), \; v_y = -\exp(-ik \cdot a_2 u_2) \tag{4.25}$$

For TE modes, the eigen-equation is:

$$k_0^2 \hat{H}_z = \mu_{33}^{-1}\left\{V_1\left(\varepsilon_{21}^{-1}U_2 - \varepsilon_{22}^{-1}U_1\right) - V_2\left(\varepsilon_{11}^{-1}U_2 - \varepsilon_{12}^{-1}U_1\right)\right\}\hat{H}_z . \tag{4.26}$$

The U and V matrices for TE mode are similar to those for TM modes and can be obtained by doing the exchange $U_1 \Leftrightarrow V_1$ and $U_2 \Leftrightarrow V_2$ in the equations (4.22-4.25) for TM modes.

According to Eq. (4.21), only ε_{33}^{-1} is involved in TM mode. ε_r is located at the same point as E_3, so no averaging is needed for ε_{r3}. For TE mode, the ε_r is half a grid away from E_1 and E_2 and the averaging is needed for ε_{r1} and ε_{r2}. The periodicity of ε_r is applied for those grids outside the boundary.

4.3. Comparison between FDFD and PWM

4.3.1 Examples for 2D band gap

All matrices involved are sparse; hence we can apply sparse matrix techniques to save computation time and memory. We implemented the algorithm using MATLAB since it provides convenient tools for sparse matrix operation with minimal programming efforts. Here we show a few numerical examples using our FDFD method and compare against the PWM using the program similar to that in Ref. [111]. The first example is a 2D square lattice with dielectric alumina rods in air: ε_a=8.9, ε_b=1.0 and radius of the rod R=0.20a (a is the lattice constant). The second example is a 2D triangular lattice with air holes in dielectric GaAs materials: ε_a=1.0, ε_b=13.0 and hole radius R=0.20a. For the square lattice u_1=[1 0 0], u_2=[0 1 0], and u_3=[0 0 1] and the metric [g] is a 3x3 identity matrix. For the triangular lattice, u_1=[1 0 0], u_2=[0 1/2 $\sqrt{3}/2$], and u_3=[0 0 1] and [g] is calculated by Eq. (4.4). We used sub-cell averaging techniques to smooth the transition at the interface and Eq. (4.5) is used for the rod profile transformation. The details of discretization and transformation of the cylindrical rod are shown in Ref. [111].

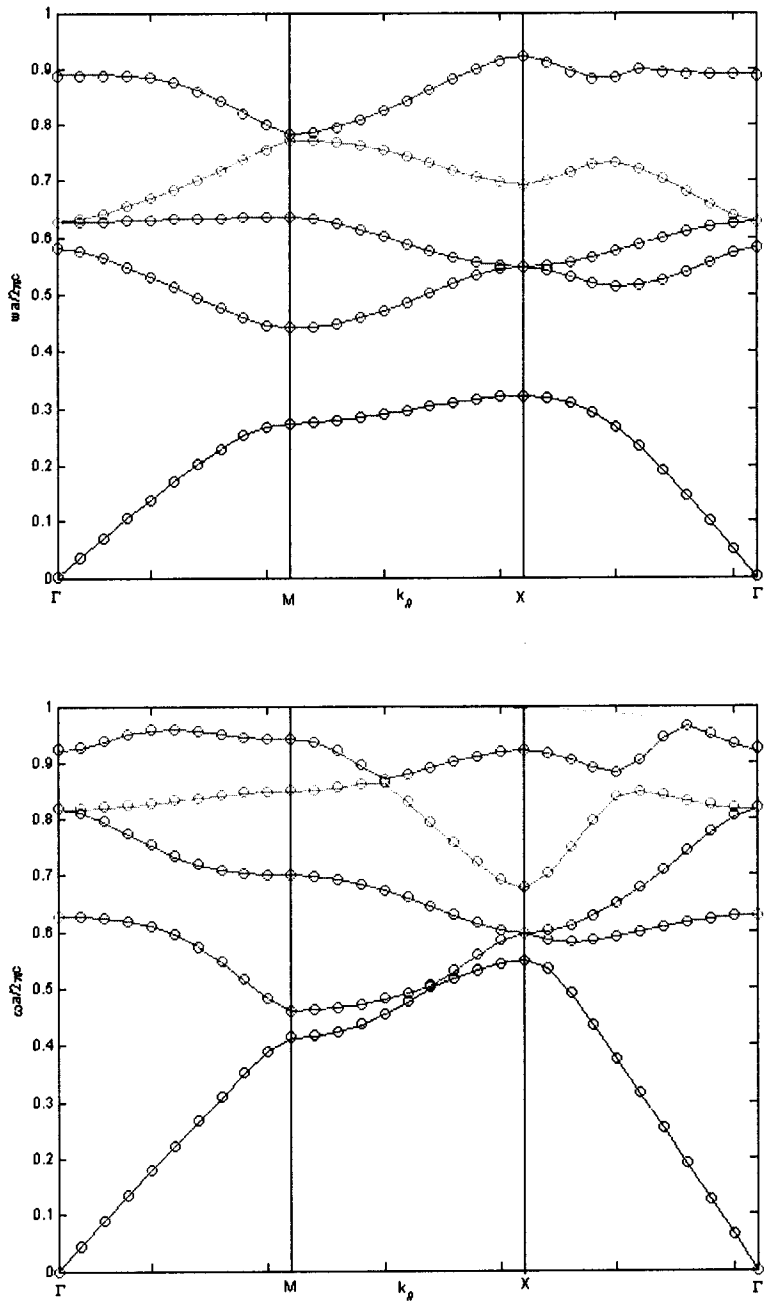

Fig.21. The band structure for a 2D square lattice by FDFD (o) and PWM (-). 441 plane waves are used for PWM and mesh resolution is a/80 for FDFD. Upper: TM mode, Bottom: TE mode.

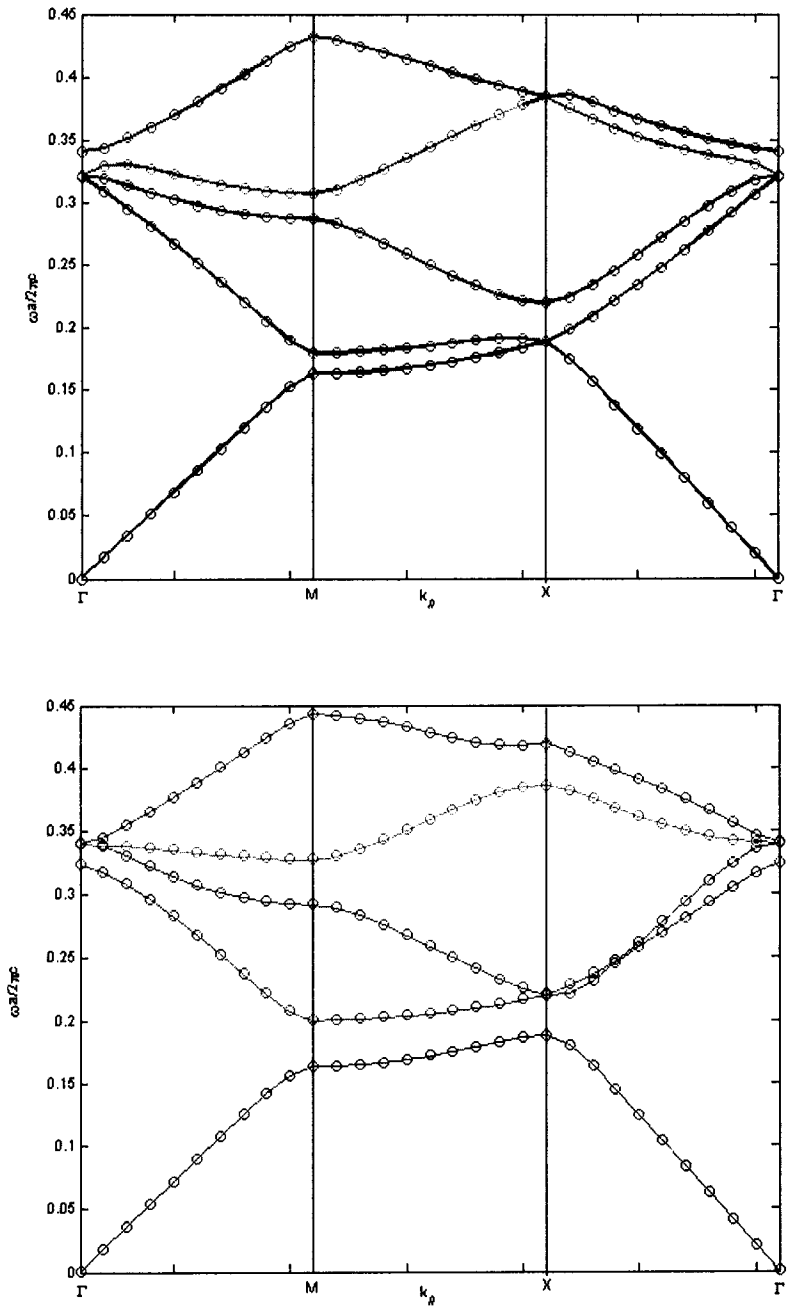

Fig. 22. The calculated band structure of a triangular lattice by FDFD (o) and PWM (-). 441 plane waves are used for PWM and mesh resolution is a/80 for FDFD. Upper: TM, Bottom: TE.

The TE/TM band gap for 2D square lattice and triangular lattice of the above examples are shown in Figs. 21 and 22, respectively. The FDFD results are indicated by 'o' and PWM results are plotted as solid lines. The results from the two methods show excellent agreements.

In Table 7 we list the first five bands at k=0 for the 2D triangular lattice shown above using the two methods in order to compare their accuracy and computation time. The computation time is measured on a 2.4GHz mobile Celeron® notebook with 256MB memory. From the Table we see that FDFD can reach the same accuracy as PWM in a shorter time.

Table 7. Eigen-frequencies for the first five bands of TE wave (k=0) for a triangular lattice with air holes in dielectric materials.

Band No:	1	2	3	4	5	Time (s)
PWM 441^1	0	0.3240	0.3398	0.3399	0.3414	47.84
PWM 625^1	0	0.3240	0.3399	0.3399	0.3414	105.66
PWM 961^1	0	0.3240	0.3400	0.3400	0.3414	256.36
FDFD 40^2	0	0.3237	0.3395	0.3400	0.3418	3.29
FDFD 80^2	0	0.3240	0.3400	0.3402	0.3416	11.68
FDFD 120^2	0	0.3240	0.3400	0.3402	0.3415	33.18
FDFD 160^2	0	0.3240	0.3401	0.3402	0.3414	86.09

1: The number of plane waves, 2: the number of grids along each direction.

4.3.2 Convergence property

A convergence curve for the eigen-frequency of band 5 at k=0 is shown in Fig. 23 versus the number of grids used along each direction. The computation time is also

presented in the figure. The eigen-values converge to the accurate value at a moderate mesh size, for example, a/80. The computation time is highly dependent on the memory available on the computer. When the unit cell or supercell has symmetry properties, computation time could be saved by using part of the unit cell under proper boundary conditions [80].

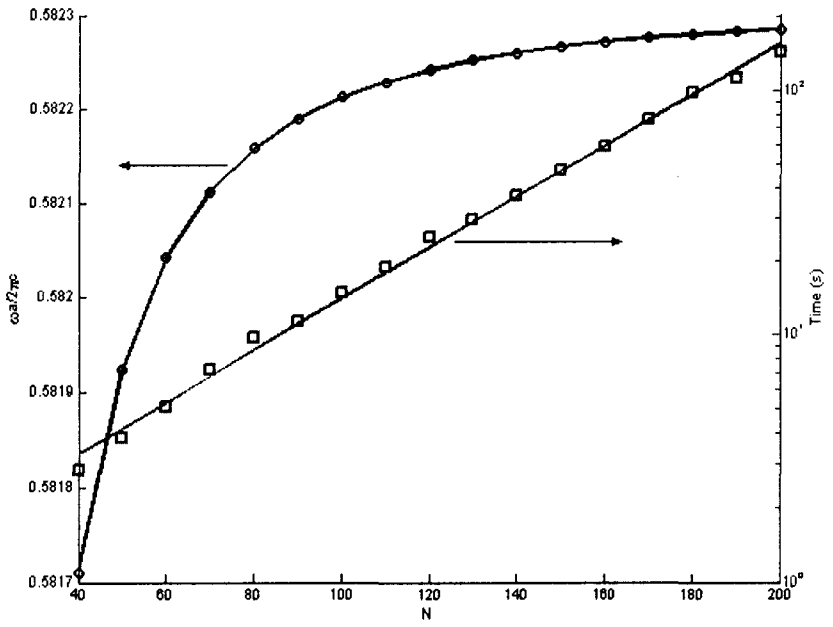

Fig. 23. The convergence of eigen-frequency (the 5th band at k=0) and the computation time vs. the number of grids along each direction.

4.3.3 Defect mode

Next, we show a defect mode analysis using FDFD for the 2D square lattice of alumina rods in air as in the first example. A 5×5 supercell is selected and 200 grids are used along each direction. In this case, only the defect frequency is of interest since the band gap information is already known. Therefore we only have to find a certain number of eigen-frequencies of interest and the computation time is effectively reduced. The

eigen-frequency obtained by FDFD is 0.3930. The mode field is shown in Fig. 24. Both results agree well with those by PWM and FDTD [111, 112].

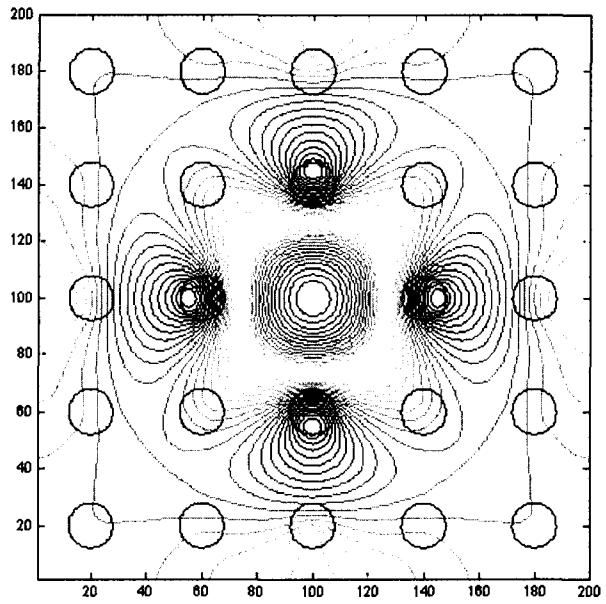

Fig. 24. The E_z field of a defect mode in a 2D square lattice with alumina rods in air using a 5×5 supercell with the center rod removed. The rods are displayed as black circles.

4.4 Out-of-plane PBGs of the photonic crystal fiber cladding

Silica is the most widely used material to fabricate PCFs. The refractive index of silica is ~1.45 which can not provide enough index contrast with air to form an in-plane band gap. However, it does have out-of-plane band gap under certain range of propagation constant β. To analyze the out-of-plane band gap structure of the photonic crystal fiber, Eq. (4.10) should be employed for PWM. Also, we can not use Eqs. (4.21) and (4.26). Because U_3 and V_3 are not zero now but $U_3 = V_3 = j\beta I$ (I is the identity matix), the Maxwell's Eqs. (4.18-4.19) do not de-coupled. We can still use the mesh shown in

Fig. 20, but the problem becomes to a pseudo 3D one. For this purpose, we rewrite the Maxwell's Eqs. here again

$$jk_0\begin{bmatrix}\hat{E}_1\\ \hat{E}_2\\ \hat{E}_3\end{bmatrix}=\begin{bmatrix}\varepsilon_{11}^{-1} & \varepsilon_{12}^{-1} & 0\\ \varepsilon_{21}^{-1} & \varepsilon_{22}^{-1} & 0\\ 0 & 0 & \varepsilon_{33}^{-1}\end{bmatrix}\begin{bmatrix}0 & -j\beta I & U_2\\ j\beta I & 0 & -U_1\\ -U_2 & U_1 & 0\end{bmatrix}\begin{bmatrix}\hat{H}_1\\ \hat{H}_2\\ \hat{H}_3\end{bmatrix}, \tag{4.27}$$

$$-jk_0\begin{bmatrix}\hat{H}_1\\ \hat{H}_2\\ \hat{H}_3\end{bmatrix}=\begin{bmatrix}\mu_{11}^{-1} & \mu_{12}^{-1} & 0\\ \mu_{21}^{-1} & \mu_{22}^{-1} & 0\\ 0 & 0 & \mu_{33}^{-1}\end{bmatrix}\begin{bmatrix}0 & -j\beta I & V_2\\ j\beta I & 0 & -V_1\\ -V_2 & V_1 & 0\end{bmatrix}\begin{bmatrix}\hat{E}_1\\ \hat{E}_2\\ \hat{E}_3\end{bmatrix}. \tag{4.28}$$

We can easily obtain the eigen-value equations by substituting Eq. (4.28) into (4.27) or vise versa.

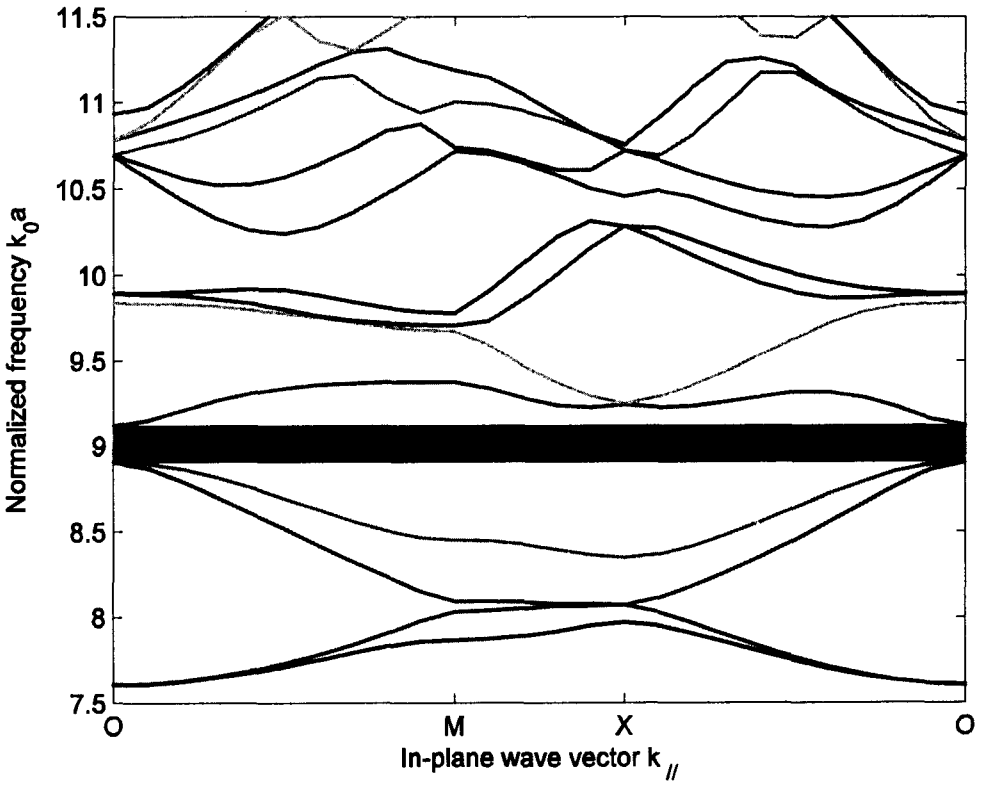

Fig. 25. Out-of-plane band structure diagram of a triangular photonic crystal with a 70% air-filling ratio. The propagation constant is fixed as βa = 9.0. Refractive index of silica is 1.45.

Fig. 25 shows an out-of-plane band structure for the cladding of a photonic crystal fiber with a triangular lattice. The filling ratio for this fiber is 70%. There is gap opened at around a normalized frequency $k_0a = 9.0$. This gap overlaps the air line $\beta/k_0 = 1$ which means the light can be guided in an air core. This result agree well with the published one [17].

4.5. Summary and discussion

In summary, a FDFD method for photonic band gap calculations is developed. This method is able to provide complete and accurate information about the band structure of a photonic crystal. The results of 2D TE/TM modes for two different geometries are compared with those obtained using plane wave method, and excellent agreement is achieved. By using a generalized coordinate system, various lattice geometries can be analyzed in the same manner. Moreover, out-of-plane band structure of the cladding photonic crystal of the photonic crystal fiber is analyzed. For this case, the general eigen-value equations should be used. With the band structure information combined with the propagation characteristics which can be analyzed by the methods described in the previous chapters, the design and analysis of PBG-guiding PCFs can be fulfilled without difficulty.

CHAPTER V

MODELING AND SIMULATION OF DISTRIBUTED FEEDBACK PHOTONIC CRYSTAL FIBER LASERS

In previous chapters, several models are proposed to analyze the propagation properties of PCFs. The FDFD method combined with PML technique can solve almost all linear problems of PCFs, such as dispersion and loss properties. In this chapter, a nonlinear device, DFB PCF laser, is discussed.

The chapter is organized as follows to simulate DFB PCF lasers. The formulas for Er-doped and Er/Yb co-doped DFB PCF laser are introduced in section 5.1. In section 5.2, the properties of Er-doped DFB PCF lasers near the thresholds are analyzed, followed by the numerical results for the Er/Yb co-doped PCF lasers. Section 5.3 concludes the chapter.

5.1. Model and Theory

The model presented here is developed based on Ref. [63]. This model investigates the output characteristics of DFB PCF lasers using FDFD method presented in the previous chapters, coupled-mode theory [13], the transfer-matrix approach [14], and gain models for Er and Er/Yb media. The electric field distribution is calculated using FDFD method. The coupled-mode theory is utilized to analyze the Bragg Grating, and transfer matrix method is employed to solve the coupled wave equations. The gain model of the Er medium uses a 3-level system and takes the transverse mode intensity distribution of the pump and signal into account. For Er/Yb co-doped medium, an energy transfer mechanism between Yb^{3+} and Er^{3+} is added into the gain model.

5.1.1. Coupled mode theory and transfer matrix method

In a DFB PCF laser, distributed feedback is realized by inscribing a Bragg grating into the PCF. A phase shift is introduced into the grating for single wavelength output. To describe the behavior of the fiber Bragg grating (FBG), the well-known coupled-mode equations are employed [67]:

$$\frac{dE_+}{dz} = \kappa \exp[j(2\Delta\beta z - \phi)]E_- + \frac{g}{2}E_+ \tag{5.1}$$

$$\frac{dE_-}{dz} = \kappa \exp[-j(2\Delta\beta z - \phi)]E_+ - \frac{g}{2}E_- \tag{5.2}$$

where, E_+ and E_- are the forward and backward electric field, respectively, g is the gain, ϕ is the phase of the grating, and κ the coupling constant (modulation strength) .

$$\Delta\beta = \beta - \beta_B,\ \beta_B = \frac{\pi}{\Lambda_g} \tag{5.3}$$

where, β is the propagation constant, and Λ_g is the period of the Bragg grating.

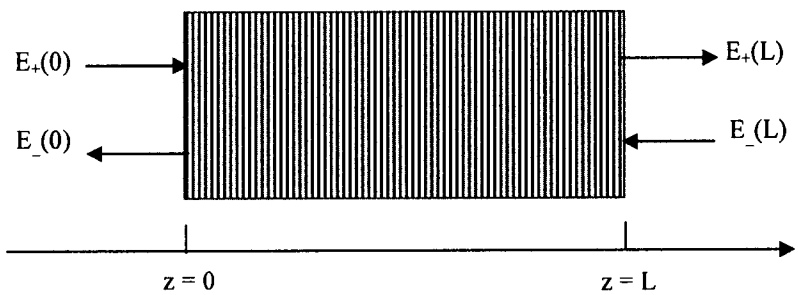

Fig. 26. Schematic diagram of a grating.

To solve the coupled mode equations, we use the transfer matrix method [68]. For a uniform grating shown in Fig. 26, we have

$$\begin{pmatrix} E_+(0) \\ E_-(0) \end{pmatrix} = [F]\begin{pmatrix} E_+(L) \\ E_-(L) \end{pmatrix} \tag{5.4}$$

The elements of the F matrix are given as follows:

$$F_{11} = [\cosh(\gamma L) + i\,{}^{\Delta\beta'}\!/_{\gamma}\sinh(\gamma L)]\exp(i\beta_B L) \tag{5.5a}$$

$$F_{12} = -{}^{\kappa}\!/_{\gamma}\sinh(\gamma L)\exp[-i(\beta_B L + \phi)] \tag{5.5b}$$

$$F_{21} = -{}^{\kappa}\!/_{\gamma}\sinh(\gamma L)\exp[i(\beta_B L + \phi)] \tag{5.5c}$$

$$F_{22} = [\cosh(\gamma L) - i\,{}^{\Delta\beta'}\!/_{\gamma}\sinh(\gamma L)]\exp(-i\beta_B L) \tag{5.5d}$$

where

$$\Delta\beta' = \Delta\beta + ig, \gamma^2 = \kappa^2 - (\Delta\beta')^2 \tag{5.6}$$

and ϕ is the phase of the grating at position z = 0.

5.1.2. Gain model

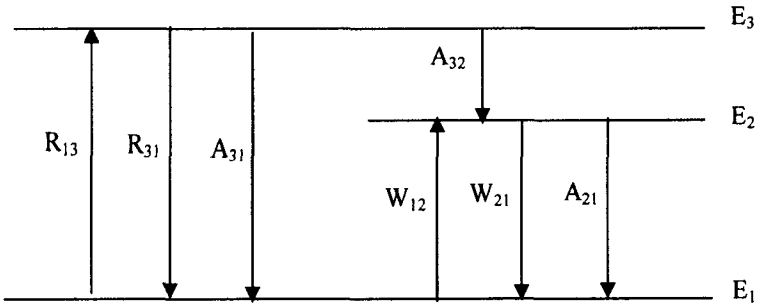

Fig. 27. Three-level energy level diagram for Erbium.

Er atom is modeled as a three-level medium as shown in Fig. 27. E_1 is the ground level and E_2 is the upper level of the laser. Starting from the rate equations, we can get:

$$X = \frac{N_2}{N} = \frac{R_{13}\tau + W_{12}\tau}{1 + R_{13}\tau + W_{12}\tau + W_{21}\tau} \tag{5.7}$$

$$g_s = \int \rho(r) f_s(r)\left[X(r)\sigma_{e,s} - (1 - X(r))\sigma_{a,s}\right]d^2 r - \alpha_s \tag{5.8}$$

$$g_p = -\int \rho(r) f_p(r)(1 - X(r))\sigma_{a,p} d^2 r - \alpha_p \tag{5.9}$$

$$f_i(r) = \frac{\varepsilon_r(r)|E(r)|^2}{\int \varepsilon_r(r)|E(r)|^2 d^2r} \tag{5.10}$$

where, g_s and g_p are the effective gains for signal and pump per unit length, respectively. α_s and α_p are the background loss in the fiber. ρ is the erbium concentration. X is the inversion factor, and f is normalized field intensity distribution in the fiber. σ_e and σ_a are the emission and absorption cross-sections.

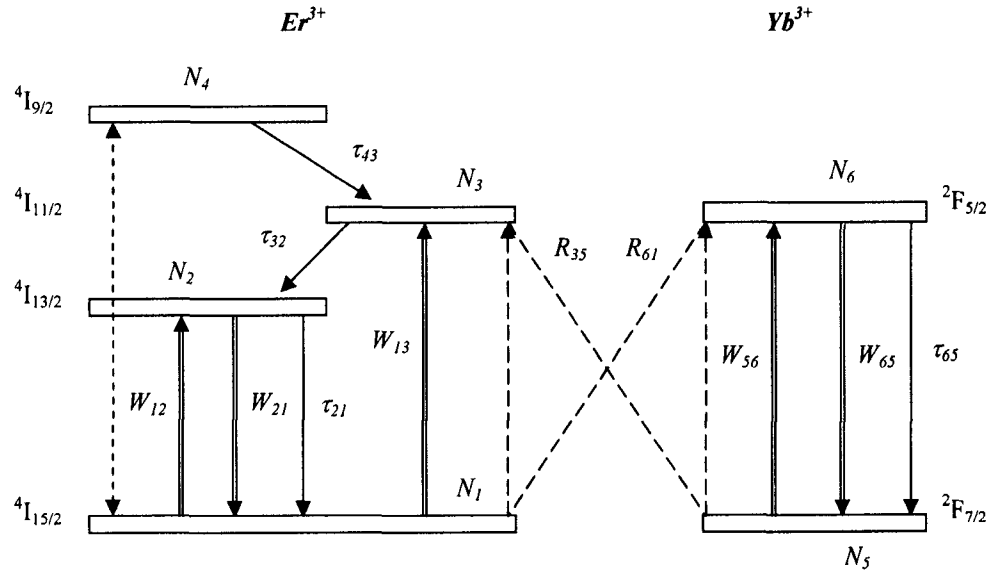

Fig. 28. Energy level transitions for Er^{3+}/Yb^{3+} systems.

To model Er/Yb co-doped medium, we need consider the energy transfer between the Yb and Er atoms as shown in Fig. 28 [113]. The effective gains are given by

$$g_s(z) = \int N_{Er} f_s(r)\left[\sigma_{21}\hat{N}_2 - \sigma_{12}(1-\hat{N}_2)\right] d^2r - \alpha_s \tag{5.11}$$

$$\begin{aligned} g_p(z) = {} & \int N_{Yb} f_p(r)\left[\sigma_{65}\hat{N}_6 - \sigma_{56}(1-\hat{N}_6)\right] d^2r \\ & - \int N_{Er} f_p(r)\sigma_{13}(1-\hat{N}_2)\, d^2r - \alpha_p \end{aligned} \tag{5.12}$$

$$\hat{N}_2 = \left(1 + \frac{1/\tau_{21} + W_{21}}{W_{12} + W_{13} + R_{61}N_{Yb}\hat{N}_6}\right)^{-1} \tag{5.13}$$

$$\hat{N}_6 = \left(1 + \frac{1/\tau_{65} + W_{65} + R_{61} N_{Er}(1 - \hat{N}_2)}{W_{56}}\right)^{-1} \tag{5.14}$$

where, N_{Er} and N_{Yb} are the Er and Yb concentrations.

5.1.3 Numerical method

In the grating region, the pump propagates through without reflection, and the pump power follows

$$\frac{dP_p}{dz} = g_p P_p \tag{5.15}$$

Meanwhile the signal is governed by Eqs (5.1) and (5.2). Since the transfer matrix method [67] used to solve these equations is valid only for a uniform grating, the whole grating is divided into several shorter ones. Each short grating is approximated by a uniform grating with constant κ, γ, g and ϕ as shown in Fig. 29. The transfer matrix method is applied for each of them. An initial guess solution is set to output $E_+(L)$ and zero to $E_-(L)$, then the output is adjusted during the repeating calculation cycles until the boundary condition, $E_+(0) = 0$, is satisfied.

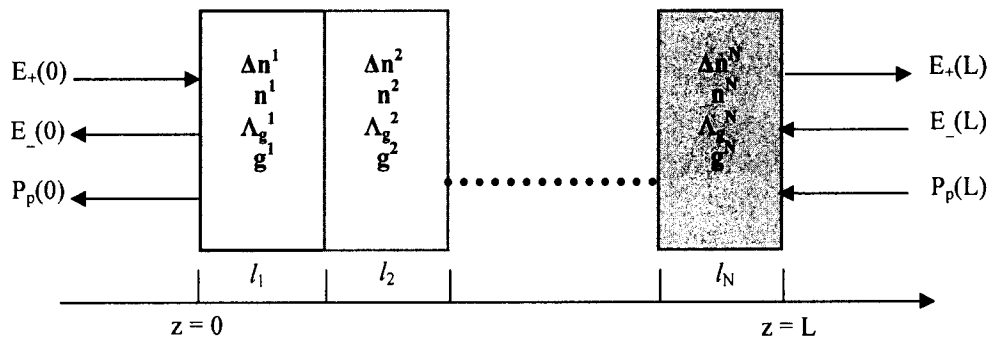

Fig. 29. Segmentation diagram for modeling a distributed feedback laser.

5.2. Numerical Results

Based on the model, our algorithm is realized using Matlab®. We verify the algorithm by calculating the output characteristics of DFB TPCF lasers with the same parameters used in Ref [63], and similar results are obtained. We then analyze the output characteristics both for Er doped and Er/Yb co-doped DFB CPCF lasers.

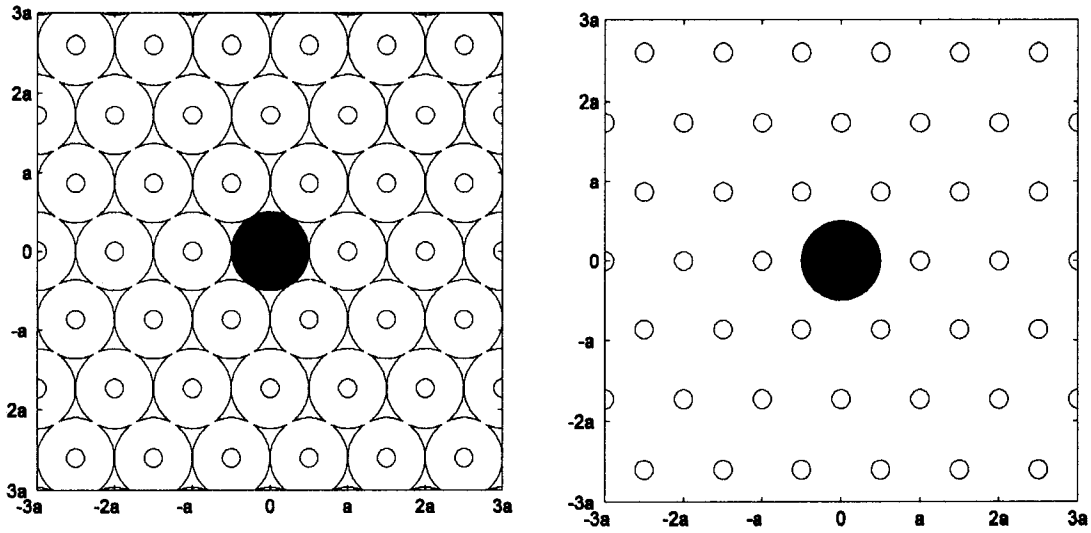

Fig. 30. Schematic diagrams of the cross section of a CPCF (left) and a TPCF (right). The solid red circles in the center represent the doped region.

The geometries of a CPCF and a TPCF are shown in Fig. 30. The red solid circles are the doped region. The ratio between the air hole diameter and the lattice constant d/a is 0.23. The refractive index of the silica was chosen to be 1.45. Lattice constants of 3.4, 5.4, and 7.6 μm, were chosen to ensure both CPCFs and TPCFs work in single mode for both pump and signal wavelengths.

For lasers analyzed in this chapter, we assume that the period of the grating is chosen such that the detuning $\Delta\beta$ is zero. A typical spectrum of the grating without amplification

is shown in Fig.31. The sharp transmission peak located at $\Delta\beta = 0$ inside the reflection band is the lasing wavelength.

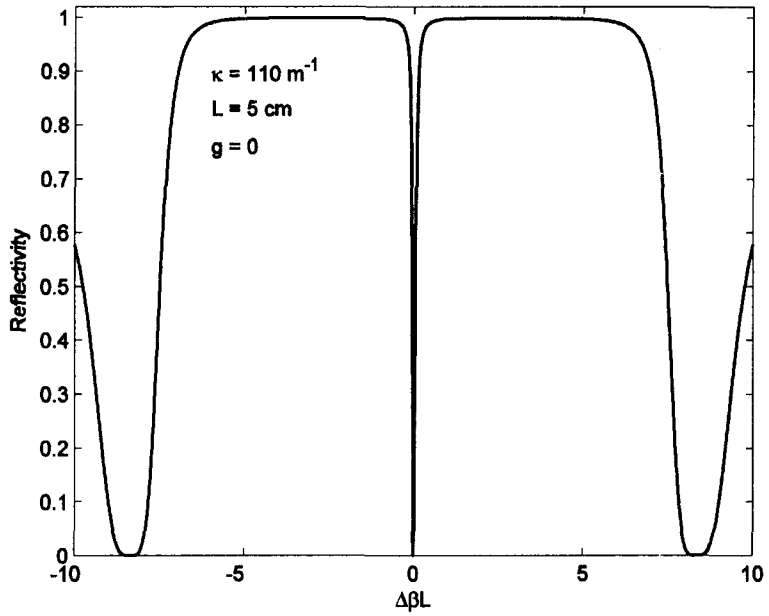

Fig. 31. The spectrum of the grating (g = 0) with a phase shift π in the middle.

5.2.1. Er doped DFB PCF lasers

For Er doped DFB lasers, a three-level gain model as shown in Fig. 27 [63] is used. The outputs near the thresholds are shown in Fig. 32 as functions of the pump power. The parameters used in the simulation are listed in Table 8. The comparison of the thresholds between CPCF and TPCF lasers is shown in Table 9. The threshold increases with the lattice constant due to the increased number of doped atoms which absorb more power to reach population inversion. An exception is the laser using TPCF with lattice constant of 3.4 μm. This laser has higher threshold than that with lattice constant of 5.4 μm. This is because of the propagation loss. Furthermore, the comparison between TPCF and CPCF lasers with same lattice constant shows that DFB lasers using CPCF have lower threshold

than TPCF lasers. This is due to the better confinement in the CPCF which is achieved by the extra interstitial air regions.

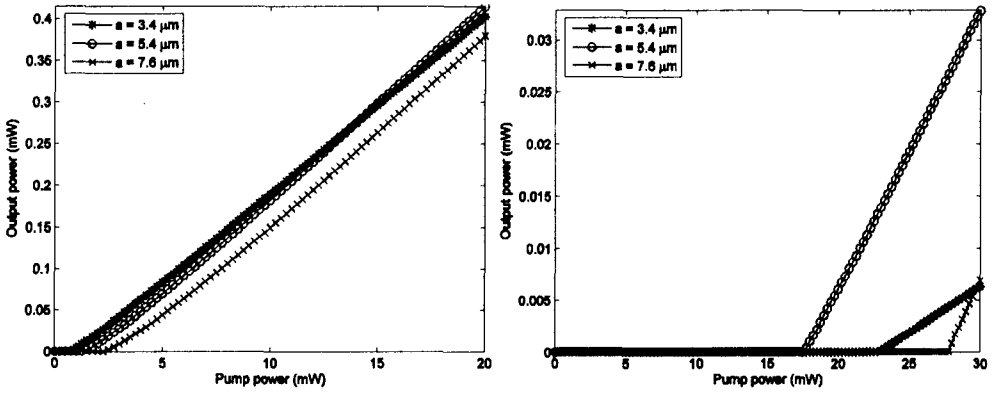

Fig. 32. Output characteristics near the thresholds of Er doped DFB CPCF lasers (left) and TPCF lasers (right). $N_{Er} = 2.6\times10^{25}$ /m^3. The radius of doped region is a/2, and signal propagation loss $\alpha = 0.25$ m^{-1}.

Table 8. Parameters used in the simulations for Er-doped PCF lasers.

Parameter	Value
σ_a : Er absorption cross section at 1560 nm	2.0×10^{-25} m^2
σ_e : Er emission cross section at 1560 nm	2.6×10^{-25} m^2
σ_{13} : Er absorption cross section at 980 nm	2.0×10^{-25} m^2 [114]
τ_{21} : Er spontaneous emission lifetime	11 ms [113, 114]

Table 9. Thresholds for DFB CPCF and TPCF lasers ($N_{Er} = 2.6\times10^{25}$ /m^3, $\kappa = 110$ m^{-1}, $\alpha = 0.25$ /m, and the radius of the doped region is a/2.)

	CPCF			TPCF		
Lattice constant a (μm)	3.4	5.4	7.6	3.4	5.4	7.6
Threshold (mW)	0.7	1.3	2.3	23.0	17.7	27.8

Based on these results, it is found that the CPCF with a small mode area is useful for low threshold DFB fiber laser. The slope efficiency of DFB CPCF laser is very poor (~2%) near the threshold while TPCF is even worse due to the poorer intensity confinement. Er/Yb co-doped lasers have much better slope efficiencies.

5.2.2. Er/Yb co-doped DFB PCF lasers

To improve the performance of the DFB PCF laser, obviously, Er/Yb co-doping is an effective way. According to published experimental results, the ratio N_{Yb}/N_{Er} should be in the range of 10 – 20 to ensure an efficient energy transfer from Yb^{3+} to Er^{3+} [114]. The parameters employed in the simulation are list in table 10.

Table 10. Parameters used in the simulations for Er/Yb co-doped PCF lasers.

Parameter	Value
σ_{12} : Er absorption cross section at 1560 nm	2.0×10^{-25} m^2
σ_{21} : Er emission cross section at 1560 nm	2.6×10^{-25} m^2
σ_{13} : Er absorption cross section at 980 nm	2.0×10^{-25} m^2 [114]
τ_{21} : Er spontaneous emission lifetime	11 ms [113, 114]
σ_{56} : Yb absorption cross section	2.0×10^{-25} m^2 [114]
σ_{65} : Yb emission cross section	5.0×10^{-25} m^2 [114]
τ_{65} : Yb spontaneous emission lifetime	1.5 ms [114]
R_{61} : cross-correlation coefficient	5.0×10^{-21} m^3/s [114]

a. Output power vs. coupling constant κ

The dependence of output power on coupling constant κ is calculated with and without background signal transmission loss. The results are shown in Fig. 33. The pump power is fixed at 100 mW in the calculation. In the case of loss, there is an optimal coupling constant where the output power reaches maximum for a fixed pump power. If the coupling constant is higher than this optimum, the output decreases. On the other hand, the output increases monotonically without loss when κ changes from ~80 m^{-1} to 200 m^{-1}. These results are similar to those of DFB TPCF lasers in Ref [63]. Based on these results, we choose a coupling constant of 110 m^{-1} for the following calculations.

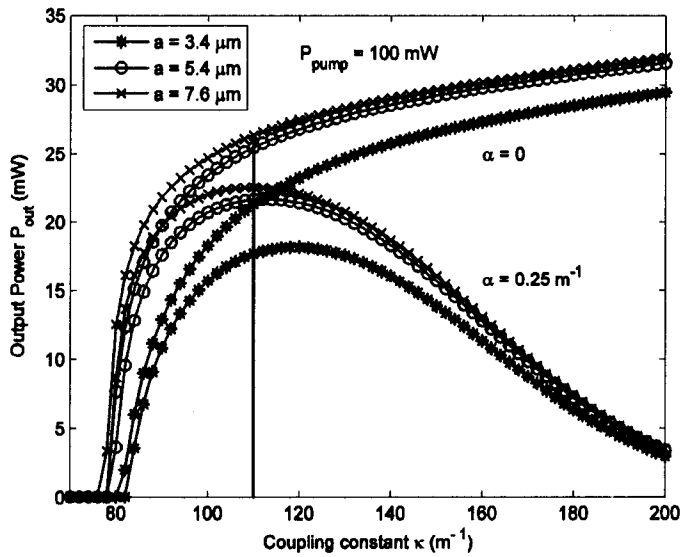

Fig. 33. Output power as a function of coupling constant κ for DFB CPCF lasers. A phase shift of π is introduced in the center of the grating. The background signal transmission loss α = 0 and 0.25 m^{-1}. Pump power is 100 mW. $N_{Er} = 2.6\times10^{25}$ /m^3, $N_{Yb} = 3.25\times10^{26}$ /m^3.

c. Output power vs. the phase shift position

Due to the configuration of the DFB fiber laser, both ends of the Bragg grating should have outputs. The results are shown in Fig. 34. The two outputs are identical if the

phase shift is located in the middle of the grating. And they are symmetric with the position of the phase shift relative to the middle of the grating. In most applications, we only need one output. Therefore, to increase one while suppressing another is important to obtain higher output power. The output power is not the highest when the phase shift is in the middle. The maximal output occurs when the phase shift moves away from the center to an optimal position. The output power could be improved by ~46% under the parameters shown in Fig. 34. This result is calculated for DFB CPCF laser with 3.4μm lattice constant using pump power of 100 mW and coupling constant of 110 m^{-1}.

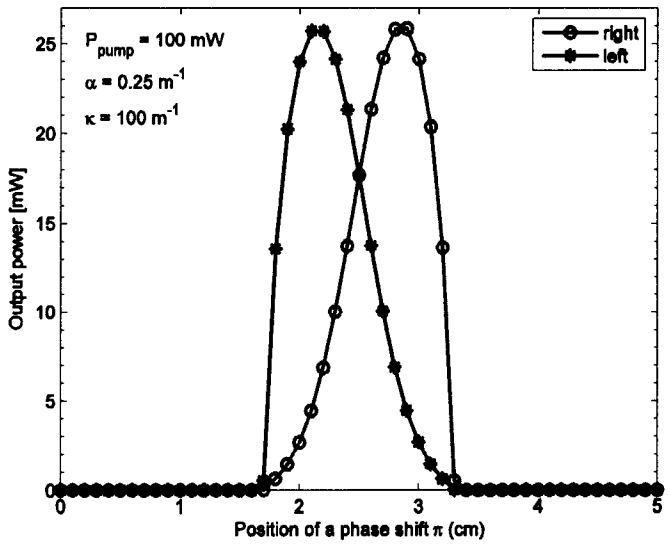

Fig. 34. Output power at two ends of the Bragg grating as a function of the position of the phase shift for DFB CPCF laser with a lattice constant of 3.4 μm. The pump power , the coupling constant, and signal propagation loss are 100 mW, 110 m^{-1}, and 0.25 m^{-1}. $N_{Er} = 2.6\times10^{25}$ /m^3, $N_{Yb} = 3.25\times10^{26}$ /m^3.

d. Intensity distribution within the Bragg grating

In DFB semiconductor lasers, the nonuniform intensity distribution is an important problem because it can lead to single mode instability through spatial hole burning effects [115]. The same situation will occur in DFB fiber laser. A sharp intensity peak located in

the vicinity of the phase shift has been experimentally proven using a green fluorescence scanning technique [116]. The simulation result as shown in Fig. 35 agrees with the experimental result very well. This nonuniform intensity distribution will degrade the laser performance. Chirped DFB structure is preferred to reduce this peak [117, 118]. Another solution is to distribute the phase shift into several locations other than totally in a single place.

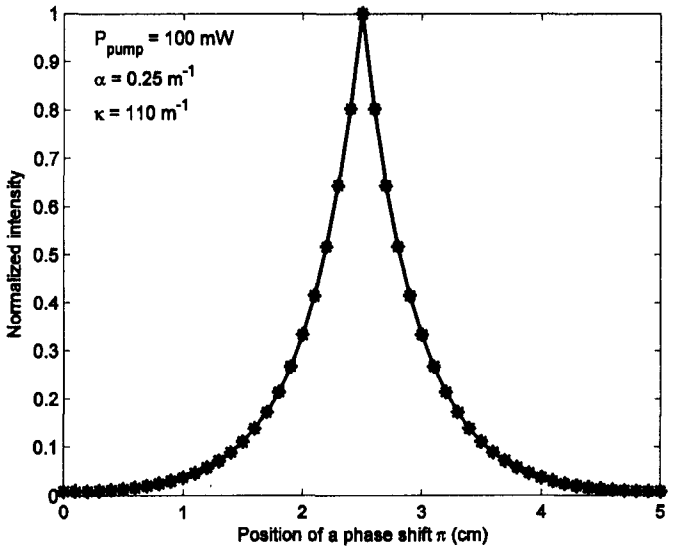

Fig. 35 Signal intensity distribution within the Bragg grating. The parameters used to calculate this profile are: κ=110 m^{-1}, the pump power = 100 mW, signal propagation loss α = 0.25 m^{-1}, and the phase shift of π is located at 2.5 cm. $N_{Er} = 2.6\times10^{25}$ /m^3, $N_{Yb} = 3.25\times10^{26}$ /m^3.

e. Output vs. pump power

Figs. 36 and 37 show the outputs as functions of the pump power. The coupling constant κ is chosen as 110 m^{-1} and the ratio of N_{Yb}/N_{Er} kept as 12.5. The output characteristics near the thresholds are shown in Fig. 36 and Table 11. It is found that CPCF has lower thresholds than TPCF. Fig. 37 demonstrates the output characteristics for pump power ranging from 0 to 600 mW. For both CPCF and TPCF lasers, the

saturation effect is obvious for fibers with smaller lattice constants. Furthermore, lasers using PCF with smaller lattice constants have higher output power near the threshold.

Eventually, lasers using PCF with larger lattice constants will catch up and have higher output power with the increase of the pump power. By increasing the doping concentration, the threshold increases. This means that more power is needed to achieve population inversion for higher concentration. The saturation is reduced with the higher doping concentration also. The output curve of laser with smaller lattice constant is closer to that of laser with larger lattice constant by increasing the doping concentration. The DFB laser using CPCF with lattice constant of 7.6 μm has the highest output power using high pump power (~120, ~160, and ~180 mW under 600 mW pump for three different doping concentrations) because of the largest doped region and better intensity confinement in the doped region than the TPCF laser. The slope efficiency far away from the threshold also increases with the doping concentrations. Based on these results, it's obvious that the PCF laser with smaller mode area is suitable for low threshold application while the PCF laser with larger mode area is better for high power application.

Throughout this subsection, a phase shift of π is introduced in the center of the grating for all the lasers. The total output power should be doubled by adding two identical outputs together. For single output application, this output can be improved by shifting the position of the phase shift according to Fig. 34.

Table 11. Thresholds for DFB CPCF and TPCF lasers ($\kappa = 110\ m^{-1}$).

	CPCF			TPCF		
Lattice constant (μm)	3.4	5.4	7.6	3.4	5.4	7.6
Radii of the doped region (μm)	1.7	2.7	3.8	1.7	2.7	3.8
Signal intensity confined in the doped region	85.7%	96.4%	98.7%	35.1%	46.1%	49.9%
Pump intensity confined in the doped region	96.5%	99.1%	99.7%	46.1%	50.9%	53.6%
Threshold (mW) $N_{Er} = 3.0\times10^{25}\ /m^3$ $N_{Yb} = 3.75\times10^{26}\ /m^3$	0.2	0.4	0.7	0.2	0.4	0.8
Threshold (mW) $N_{Er} = 4.0\times10^{25}\ /m^3$ $N_{Yb} = 5.0\times10^{26}\ /m^3$	0.3	0.6	1	0.2	0.5	0.8
Threshold (mW) $N_{Er} = 5.0\times10^{25}\ /m^3$ $N_{Yb} = 6.25\times10^{26}\ /m^3$	0.4	0.9	1.6	0.2	0.5	0.9
Slope efficiency (%)	20-30			10-35		

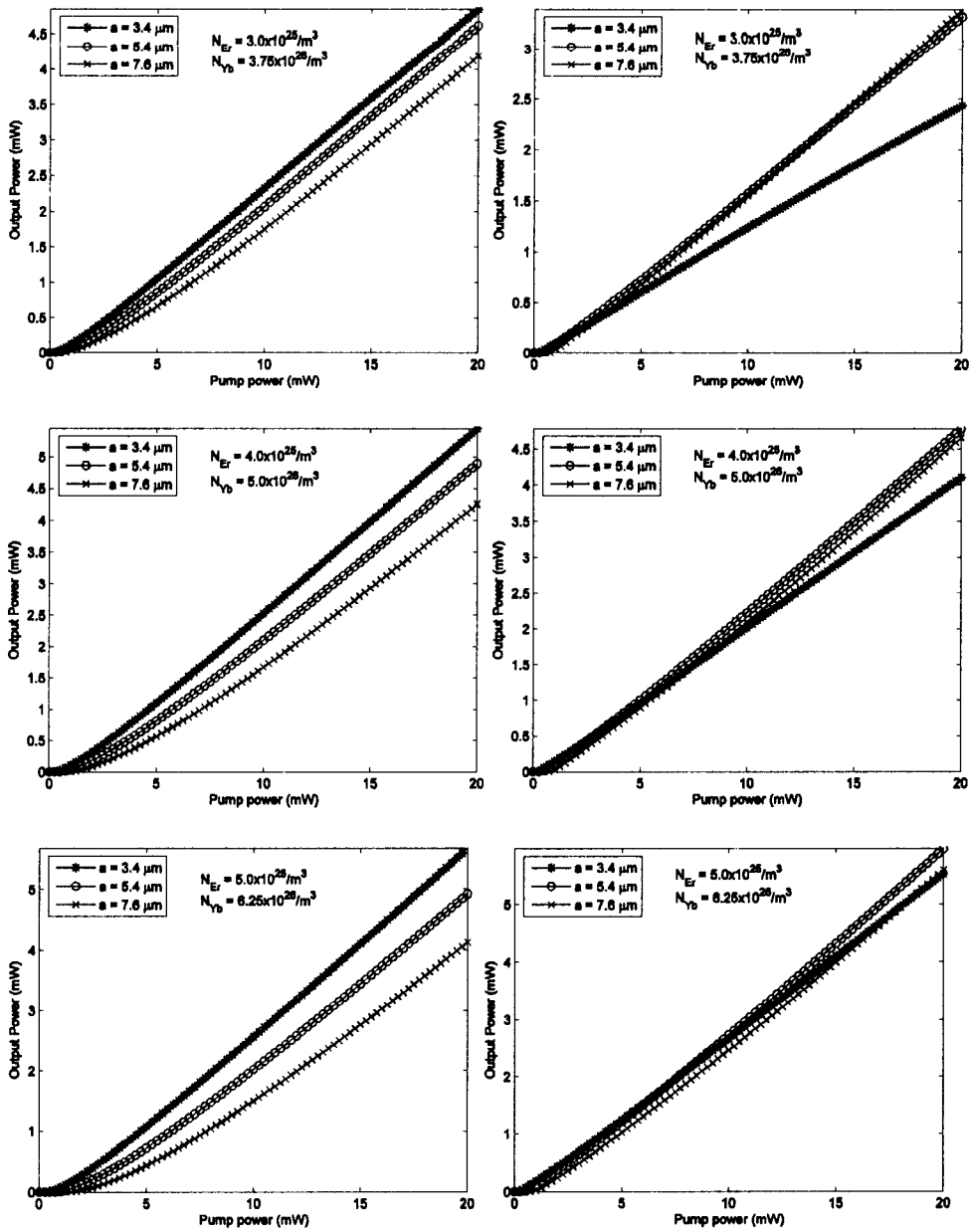

Fig. 36. Output powers as functions of pump powers near the thresholds (signal propagation loss α = 0.25 m^{-1}). Left column: DFB CPCF lasers, Right column: DFB TPCF lasers.

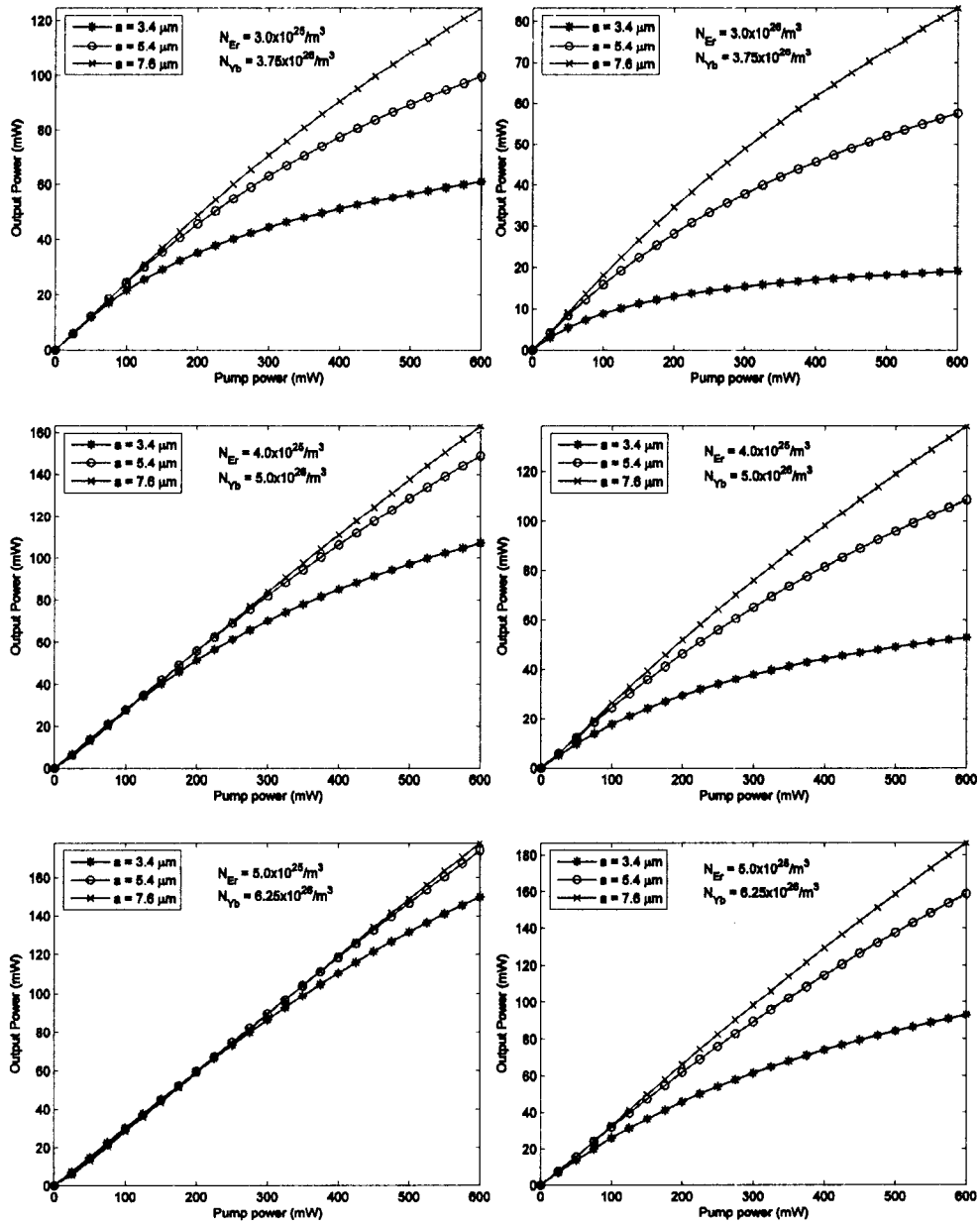

Fig. 37. Output powers as functions of pump powers (signal propagation loss α = 0.25 m^{-1}.) Left column: DFB CPCF lasers. Right column: DFB TPCF lasers.

5.3. Conclusion and discussion

In summary, we incorporate a model for Er/Yb co-doped medium into couple wave equations. Combining the transfer matrix method, we simulate the Er/Yb co-doped DFB PCF lasers with a discrete phase shift π in the middle. There is an optimal coupling

constant which can provide maximal output power. Observing the output variation as a function of the position of the phase shift, we found that the maximal output power is not obtained when the phase shift is located in the center of the grating. Furthermore, Er doped lasers are analyzed. CPCF lasers are found having lower threshold than TPCF with the same doped region and lattice constant. It's obvious that the Er/Yb co-doped PCF laser has much higher output power and slope efficiency than the corresponding Er doped PCF laser.

In conclusion, due to the extra interstitial air region, CPCF could have better confinement than TPCF. The DFB laser using CPCF is good candidate for low threshold applications. Although the linewidth is not included, this modeling is still valuable for design work. In most practical fabrication process, the PCF is made by stacking method [70], the center rod doped with active material could easily be stacked with other pure glass or plastic tubes to form a preform. The distribution of the active atoms is easier to control in CPCF following the designed region shown in this chapter.

SUMMARY AND CONCLUSION

In summary, a 2D FDFD method combined with PML technique has been proposed to analyze the dispersion and loss properties of PCFs. The FDFD method discretizes the Maxwell's equations into an eigen-value problem. The PML forms the open boundaries of the computation region. By incorporating PML, the 2D FDFD method can deal with almost all the linear propagation problems of a PCF whose cross-section is invariant in the propagation direction.

To implement the method to analyze a real PCF, it is found that the permittivity averaging technique is very important for achieving high accuracy. A proper permittivity averaging technique should take 3D Yee's cells into account other than 2D Yee's cells at the interface between two different materials. Wit this averaging technique, the propagation constant and loss can be obtained with accuracies in the orders of $\sim 10^{-6}$ and $\sim 10^{-3}$, respectively, for a moderately fine mesh. These accuracies are good enough to do further analysis such as group velocity dispersion.

Since this method is based on solving eigen-value problem, a batch of eigen-values for a given wavelength can be easily obtained in a single run. The eigen-values are the propagation constants of the confined modes and the corresponding eigen-vectors are the field distributions. Also, because of this feature, the dispersive and lossy materials can easily be analyzed using the FDFD method without any modification on the algorithm.

Although the PML is the best technique up to date to absorb the outgoing wave, it still cannot totally eliminate the reflection at the zero-boundaries as evidenced by the obtained spurious modes. The spurious modes are formed between the zero-boundaries and the air holes, and have much higher losses than the confined modes.

The drawback of this method is that the computation becomes rigorous when a very large computation region is dealt with, e.g. when the loss is investigated as a function of number of air-hole rings. Although the symmetry property of the PCF can be utilized to reduce the computation region to a quarter or even smaller region, and sparse matrix technique can relieve the memory consumption, this shortcoming still cannot be overcome.

However, for a fiber with rotational symmetry, the problem can be really simplified from 2D to 1D. Bragg fiber is such an example. Under cylindrical coordinates, not only the derivative in the propagation (z) direction, but also in the azimuthal (φ) direction can be represented using analytical expressions other than the differences. These analytical expressions obviously improved the accuracy of the algorithm. Furthermore, the computation region is reduced from a 2D region to a straight line. This reduces the dimension of matrices involved in the algorithm from $N^2 \times N^2$ to $N \times N$, which will greatly relieve the computation burden. These merits have been proven using several examples in chapter 3. To analyze the loss property of Bragg fibers, the PML technique is employed again in the cylindrical coordinates. Other than the anisotropic PML implemented in the 2D FDFD method described in chapter 2, a complex coordinate stretching method [74, 78] is used for this 1D FDFD method. The advantage of this complex coordinate stretching method is that the formula of the algorithm can be kept general for both the closed and open boundary conditions. The loss due to the finite number of Bragg layers is analyzed without additional algorithm complexity by doing the finite differences directly in complex coordinates.

A second, the Galerin method is also proposed to analyze the properties of Bragg fibers. In this method, the mode fields are expanded using orthogonal Laguerre-Gauss functions. Substituting the mode fields into Helmholtz wave equations for transverse fields under cylindrical coordinates, we obtained an eigen-value equation in matrix form again. The eigen-value is the normalized propagation constant, and the eigen-vector is the coefficients before Laguerre-Gauss functions. This method is accurate and stable which has been proven by couple of examples in chapter 3. However, this method cannot do the loss analysis like the PWM for the 2D PCFs. Moreover, only TE and TM modes are analyzed, the formula for hybrid modes is not developed yet. This work will be finished in the future.

It is found that the FDFD method is also suitable for PBG analysis by modifying the eigen-value equation. In chapter 4, a FDFD method is developed to analyze the band gap structures of photonic crystals. The eigen-value problem for band gap analysis has the eigen-value which is the wave number in vacuum (k_0), and the eigen-vector which is the filed distribution same as for PCF analysis. According to Bloch theorem, for band gap analysis, the periodic boundaries should be adopted instead of using PML technique to form open boundaries. The comparison with PWM method given in chapter 4 shows that the FDFD method can provide complete and accurate information about the band structures of a photonic crystal. Furthermore, the formula has been given in a generalized coordinate which makes various lattice geometries that can be analyzed in the same manner. Another advantage not mentioned in chapter 4 is that the FDFD method can deal with a unit cell with arbitrary shape while keeping high accuracy.

In chapter 5, a theoretical model of DFB PCF lasers has been presented. The output characteristics of Er-doped and Er/Yb co-doped DFB PCF lasers are modeled and simulated in order to find suitable PCF geometry to achieve low threshold and high output power. In this model, the properties of PCFs are analyzed by the FDFD method; the coupled mode theory is used to analyze Bragg grating; the coupled mode equations are solved by transfer matrix method; and Er atom is modeled as a three-level medium while energy transfer between Yb and Er atoms is considered for Er/Yb co-doped fiber.

When comparing the output characteristics of DFB PCF lasers with different lattice constants, it is found that CPCF laser has a lower threshold than TPCF for the same lattice constant. Under high pumping power, both CPCF and TPCF lasers have comparable output power. Therefore, both of them are suitable in high-power applications. However, the TPCF laser with a larger mode area is more useful for high-power operation. Simulation results for Er/Yb co-doped DFB PCF lasers have shown much higher output power and efficiency than Er doped lasers. Furthermore, it is found that the two outputs of a DFB PCF laser are identical when the phase shift is located in the middle of the grating. The output power is a function of the position of the phase shift, and could be increased by 46% when the phase shift moves away from the center to an optimum position. The non-uniform intensity distribution within the grating has also been shown with an intensity peak located at the position of the phase shift. These new DFB PCF lasers are still under investigation and will be commercially available in the near future. They will find their applications in communications, spectroscopy, and sensing fields.

REFERENCES

1. J. D. Joannopoulos, R. D. Meade, and J. N. Winn, *Photonic crystals: molding the flow of light* (Princeton University Press, Princeton, N.J., 1995).
2. E. Yablonovitch, "Inhibited spontaneous emission in solid-state physics and electronics," Physical Review Letters **58**, 2059-2062 (1987).
3. J. C. Knight, T. A. Birks, D. M. Atkin, and P. S. J. Russell, "Pure silica single-mode fiber with hexagonal photonic crystal cladding," in *Optical fiber communication*. San Jose, California, Feb. 1996.
4. J. C. Knight, T. A. Birks, P. S. J. Russell, and D. M. Atkin, "All-silica single-mode optical fiber with photonic crystal cladding," Optics Letters **21**, 1547-1549 (1996).
5. T. A. Birks, J. C. Knight, and P. S. J. Russell, "Endlessly single-mode photonic crystal fiber," Optics Letters **22**, 961-963 (1997).
6. A. Ferrando, E. Silvestre, J. Miret, and P. Andres, "Nearly zero ultra-flattened dispersion in photonic crystal fibers," Optics Letters **25**, 790-792 (2000).
7. W. Reeves, J. Knight, P. Russell, and P. Roberts, "Demonstration of ultra-flattened dispersion in photonic crystal fibers," OPTICS EXPRESS **10**, 609-613 (2002).
8. J. Ranka, R. Windeler, and A. Stentz, "Visible continuum generation in air silica microstructured optical fibers with anomalous dispersion at 800nm," Optics Letters **25**, 25-27 (2000).
9. S. Coen, A. Chan, R. Leonhardt, J. Harvey, J. Knight, W. Wadsworth, and P. Russell, "White-light supercontinuum generation with 60-ps pump pulses in a photonic crystal fiber," OPTICS LETTERS **26**, 1356-1358 (2001).
10. J. C. Knight, J. Broeng, T. A. Birks, and P. S. J. Russell, "Photonic band gap guidance in optical fibers," Science **282**, 1476-1478 (1998).
11. Y. Fink, D. J. Ripin, S. Fan, C. Chen, J. D. Joannopoulos, and E. L. Thomas, "Guiding optical light in air using an all-dielectric structure," J. Lightwave Technol. **17**, 2039-2041 (1999).
12. R. F. Cregan, B. J. Mangan, J. C. Knight, T. A. Birks, P. S. J. Russell, P. J. Roberts, and D. C. Allan, "Single-mode photonic band gap guidance of light in air," Science **285**, 1537-1539 (1999).
13. J. C. Knight, "Photonic crystal fibres," Nature **424**, 847-851 (2003).
14. Z. Zhu and T. G. Brown, "Analysis of the space filling modes of photonic crystal fibers," Optics Express **8**, 547-554 (2001).
15. A. Ferrando, E. Silvestre, J. J. Miret, P. Andres, and M. V. Andres, "Vector description of higher-order modes in photonic crystal fibers," Journal of the Optical Society of America A **17**, 1333-1340 (2000).
16. A. Ferrando, E. Silvestre, J. J. Miret, P. Andres, and M. V. Andres, "Full-vector analysis of a realistic photonic crystal fiber," Optics Letters **24**, 276-278 (1999).
17. J. Broeng, S. E. Barkou, T. Söndergaard, and A. Bjarklev, "Analysis of air-guiding photonic bandgap fibers," Optics Letters **25**, 96-98 (2000).
18. A. Weisshaar, J. Li, R. L. Gallawa, and I. C. Goyal, "Vector and quasi-vector solutions for optical waveguide modes using efficient Galerkin's method with Hermite-Gauss basis functions," Journal of Lightwave Technology **13**, 1795-1800 (1995).
19. W. Zhi, R. Guobin, L. Shuqin, and J. Shuisheng, "Supercell lattice method for photonic crystal fibers," Optics Express **11**, 980-991 (2003).
20. T. M. Monro, D. J. Richardson, N. G. R. Broderick, and P. J. Bennett, "Holey optical fibers: An efficient modal model," Journal of Lightwave Technology **17**, 1093-1102 (1999).
21. D. Mogilevtsev, T. A. Birks, and P. S. J. Russell, "Group-velocity dispersion in photonic crystal fibers," Optics Letters **23**, 1662-1664 (1998).
22. A. Cucinotta, G. Pelosi, S. Selleri, L. Vincetti, and M. Zoboli, "Perfectly matched anisotropic layers for optical waveguide analysis through the finite-element beam-propagation method," Microwave and Optical Technology Letters **23**, 67-69 (1999).
23. K. Saitoh and M. Koshiba, "Full-vectorial finite element beam propagation method with perfectly matched layers for anisotropic optical waveguides," Journal of Lightwave Technology **19**, 405-413 (2001).

24. K. Saitoh and M. Koshiba, "Full-vectorial imaginary-distance beam propagation method based on a finite element scheme: Application to photonic crystal fibers," IEEE Journal of Quantum Electronics **38**, 927-933 (2002).
25. M. Koshiba, Y. Tsuji, and M. Hikari, "Finite element beam propagation method with perfectly matched layer boundary conditions," IEEE Transactions on Magnetics **35**, 1482-1485 (1999).
26. F. Brechet, J. Marcou, D. Pagnoux, and P. Roy, "Complete analysis of the characteristics of propagation into photonic crystal fibers by the finite element method," Optical Fiber Technology **6**, 181-191 (2000).
27. G. Themistos, B. M. A. Rahman, A. Hadjicharalambous, and K. T. V. Grattan, "Loss/gain characterization of optical waveguides," Journal of Lightwave Technology **13**, 1760-1765 (1995).
28. K. Saitoh, M. Koshiba, T. Hasegawa, and E. Sasaoka, "Chromatic dispersion control in photonic crystal fibers: application to ultra-flattened dispersion," Optics Express **11**, 843-852 (2003).
29. M. Koshiba and Y. Tsuji, "Curvilinear hybrid edge/nodal elements with triangular shape for guided-wave problems," Journal of Lightwave Technology **18**, 737-743 (2000).
30. S. Guenneau, S. Lasquellec, A. Nicolet, and F. Zolla, "Design of photonic crystal fibers using finite elements," The International Journal of Computation and Mathematics in Electrical & Electronics Engineering COMPEL **21**, 534-539 (2002).
31. S. Guenneau, A. Nicolet, F. Zolla, and S. Lasquellec, "Numerical and theoretical study of photonic crystal fibers," Progress in Electromagnetics Research **41**, 271-305 (2003).
32. D. H. Choi and W. J. R. Hoeffer, "The finite-difference-time-domain method and its application to eigen-value problems," IEEE Transactions on Microwave Theory and Techniques **34**, 1464-1470 (1986).
33. A. Asi and L. Shafai, "Dispersion analysis of anisotropic inhomogeneous waveguides using compact 2D-FDTD," Electronics Letters **28**, 1451-1452 (1992).
34. A. C. Cangellaris, "Numerical stability and numerical dispersion of a compact 2D/FDTD method used for the dispersion analysis of waveguides," IEEE Microwave and Guided Wave Letters **3**, 3-5 (1993).
35. F. Zepparelli, P. Mezzanotte, F. Alimenti, L. Roselli, R. Sorrentino, G. Tartarini, and P. Bassi, "Rigorous analysis of 3D optical and optoelectronic devices by the compct-2D-FDTD method," Optical and Quantum Electronics **31**, 827-841 (1999).
36. S. Xiao, R. Vahldieck, and H. Jin, "Full-wave analysis of guided wave structures using a novel 2-D FDTD," IEEE Microwave and Guided wave letters **2**, 165-167 (1992).
37. N. Kaneda, B. Houshmand, and T. Itoh, "FDTD analysis of dielectric resonators with curved surfaces," IEEE Transactions on Microwave Theory and Techniques **45**, 1645-1649 (1997).
38. K. Bierwirth, N. Schulz, and F. Arndt, "Finite-difference analysis of rectangular dielectric waveguide structures," IEEE Transactions on Microwave Theory and Techniques **34**, 1104-1114 (1986).
39. P. Lüsse, P. Stuwe, J. Schüle, and H.-G. Unger, "Analysis of vectorial mode fields in optical waveguides by a new finite difference method," Journal of Lightwave Technology **12**, 487-494 (1994).
40. Z. Zhu and T. Brown, "Full-vectorial finite-difference analysis of microstructured optical fibers," Optics Express **10**, 853-864 (2002).
41. T. P. White, B. T. Kuhlmey, R. C. McPhedran, D. Maystre, G. Renversez, C. M. de Sterke, and L. C. Botten, "Multipole method for microstructured optical fibers. I. Formulation," Journal of the Optical Society of America B **19**, 2322-2330 (2002).
42. D. Marcuse, "Solution of the vector wave equation for general dielectric waveguides by the Galerkin method," IEEE Journal of Quantum Electronics **28**, 459-465 (1992).
43. S. Guo, F. Wu, K. Ikram, and S. Albin, "Analysis of circular fibers with an arbitrary index profile by the Galerkin method," Optics Letters **29**, 32-34 (2004).
44. S. Guo, S. Albin, and R. Rogowski, "Comparative analysis of Bragg fibers," Optics Express **12**, 198-207 (2004).
45. K. S. Yee, "Numerical solution of initial boundary value problems involving Maxwell's equations in isotropic media," IEEE Transactions on Antennas and Propagation **14**, 302-307 (1966).
46. N. A. Issa and L. Poladian, "Vector wave expansion method for leaky modes of microstructured optical fibers," Journal of Lightwave Technology **21**, 1005-1012 (2003).
47. P. Yeh, A. Yariv, and E. Marom, "Theory of Bragg fiber," J. Opt. Soc. Am. **68**, 1196-1201 (1978).

48. M. Ibanescu, Y. F. S. Fan, E. L. Thomas, and J. D. Joannopoulos, "An all dielectric coaxial waveguide," Science **289**, 415-419 (2000).
49. T. Kawanishi and M. Izutsu, "Coaxial periodic optical waveguide," Optics Express **7**, 10-22 (2000).
50. G. Ouyang, Y. Xu, and A. Yariv, "Comparative study of air-core and coaxial Bragg fibers: single-mode transmission and dispersion characteristics," Optics Express **9**, 733-747 (2001).
51. Y. Xu, R. K. Lee, and A. Yariv, "Asymptotic analysis of Bragg fibers," OPTICS LETTERS **25**, 1756-1758 (2000).
52. Y. Xu, G. Ouyang, R. K. Lee, and A. Yariv, "Asymptotic matrix theory of Bragg fibers," Journal of Lightwave Technology **20**, 428-440 (2002).
53. W. C. Chew, "Waves and fields in inhomogeneous media," (2002).
54. G. Ouyang, Y. Xu, and A. Yariv, "Theoretical study on dispersion compensation in air-core Bragg fibers," Optics Express **10**, 899-908 (2002).
55. J. Knight, T. Birks, R. Cregan, P. Russell, and J. de Sandro, "Large mode area photonic crystal fibre," ELECTRONICS LETTERS **34**, 1347-1348 (1998).
56. W. J. Wadsworth, J. C. Knight, W. H. Reeves, P. S. J. Russell, and J. Arriaga, "Yb3+-doped photonic crystal fibre laser," Electronics Letters **36**, 1452-1454 (2000).
57. K. Furusawa, T. M. Monro, P. Petropoulos, and D. J. Richardson, "Modelocked laser based on ytterbium doped holey fibre," Electronics Letters **37**, 560-561 (2001).
58. K. Furusawa, A. Malinowski, J. H. V. Price, T. M. Monro, J. K. Sahu, J. Nilsson, and D. J. Richardson, "Cladding pumped Ytterbium-doped fiber laser with holey inner and outer cladding," Optics Express **9**, 714-720 (2001).
59. H. Lim, F. Ö. Llday, and F. W. Wise, "Femtosecond ytterbium fiber laser with photonic crystal fiber for dispersion control," Optics Express **10**, 1497-1502 (2002).
60. J. Limpert, T. Schreiber, S. Nolte, H. Zellmer, A. Tünnermann, R. Iliew, F. Lederer, J. Broeng, G. Vienne, A. Petersson, and C. Jakobsen, "High-power air-clad large-mode-area photonic crystal fiber laser," Optics Express **11**, 818-823 (2003).
61. J. Canning, N. Groothoff, E. Buckley, T. Ryan, K. Lyytikainen, and J. Digweed, "All-fibre photonic crystal distributed Bragg reflector (PC-DBR) fibre laser," Optics Express **11**, 1995-2000 (2003).
62. N. Groothoff, J. Canning, T. Ryan, K. Lyytikainen, and H. Inglis, "Distributed feedback photonic crystal fibre (DFB-PCF) laser," Optics Express **13**, 2924-2930 (2005).
63. T. Søndergaard, "Photonic crystal distributed feedback fiber lasers with Bragg gratings," Journal of Lightwave Technology **18**, 589-597 (2000).
64. S. Guo, F. Wu, S. Albin, and R. S. Rogowski, "Photonic band gap analysis using finite-difference frequency-domain method," Optics Express **12**, 1741-1746 (2004).
65. C. Yu and H. Chang, "Compact finite-diference frequency-domain method for the analysis of two-dimensional photonic crystals," Optics Express **12**, 1397-1408 (2004).
66. H. Y. D. Yang, "Finite difference analysis of 2D photonic crystals," IEEE Transactions on Microwave Theory and Techniques **44**, 2688-2695 (1996).
67. H. Kogelnik and C. V. Shank, "Coupled-wave theory of distributed feedback lasers," Journal of Applied Physics **43**, 2327-2335 (1972).
68. M. Yamada and K. Sakuda, "Analysis of almost-periodic distributed feedback slab waveguide via a fundamental matrix approach," Applied optics **26**, 3474-3478 (1987).
69. J. Broeng, D. Mogilevstev, S. Barkou, and A. Bjarklev, "Photonic crystal fibers: A new class of optical waveguides," Opitcal Fiber Technology **5**, 305-330 (1999).
70. P. Russell, "Photonic crystal fibers," Science **299**, 358-362 (2003).
71. A. Bjarklev, J. Broeng, and A. Bjarklev, *Photonic crystal fibres* (Kluwer Academic, Boston, 2003).
72. J. P. Berenger, "A perfectly matched layer for the absorption of electromagnetic waves," Journal of Computational Physics **114**, 185-200 (1994).
73. E. A. Marengo, C. M. Rappaport, and E. L. Miller, "Optimum PML ABC conductivity profile in FDFD," IEEE Transactions on Magnetics **35**, 1506-1509 (1999).
74. F. L. Teixeira and W. C. Chew, "Systematic Derivation of Anisotropic PML Absorbing Media in Cylindrical and Spherical Coordinates," IEEE Microwave and Guided wave letters **7**, 371-373 (1997).
75. F. L. Teixeira and W. C. Chew, "Unified analysis of perfectly matched layers using differential forms," Microwave and Optical Technology Letters **20**, 124-126 (1999).

76. T. Tischler and W. Heinrich, "Accuracy limitations of perfectly matched layers in 3D finite-difference frequency domain method," IEEE Transactions on Microwave Theory and Techniques **50**, 1885-1888 (2002).
77. U. Pekel and R. Mittra, "An application of the perfectly matched layer (PML) concept to the finite element method frequency domain analysis of scattering problems," IEEE Microwave and Guided wave letters **5**, 258-260 (1995).
78. W. C. Chew, J. M. Jin, and E. Michielssen, "Complex coordinate stretching as a generalized absorbing boundary condition," Microwave and Optical Technology Letters **15**, 363-369 (1997).
79. S. D. Gedney, "An anisotropic perfectly matched layer-absorbing medium for the truncation of FDTD lattices," IEEE Trans. Antennas Propagat. **44**, 1630-1639 (1996).
80. P. R. McIssac, "Symmetry induced modal characteristics of uniform waveguides-I:Symmary of Results," IEEE Transactions on Microwave Theory and Techniques **23**, 421-429 (1975).
81. G. W. Milton, *The theory of composites* (Cambridge University Press, Cambridge, UK, 2002).
82. R. Guobin, W. Zhi, L. Shuqin, L. Yan, and J. Shuisheng, "Full-vectorial analysis of complex refractive-index photonic crystal fibers," Optics Express **12**, 1126-1135 (2004).
83. S. G. Johnson, M. Ibanescu, M. Skorobogatiy, O. Weisberg, T. D. Engeness, M. Soljacic, S. A. Jacobs, J. D. Joannopoulos, and Y. Fink, "Low-loss asymptotically single-mode propagation in large-core OmniGuide fibers," Optics Express **9**, 748-779 (2001).
84. B. Temelkuran, S. D. Hart, G. Benoit, J. D. Joannopoulos, and Y. Fink, "Wavelength-scalable hollow optical fibres with large photonic bandgaps for CO_2 laser transmission," Nature **420**, 650-653 (2002).
85. J. P. Meunier, J. Pigeon, and J. N. Massot, "A general approach to the numerical determination of modal propagation constants and field distributions of optical fibres," Optical and Quantum Electronics **13**, 71-83 (1981).
86. P. K. Mishra, I. C. Goyal, A. K. Ghatak, and E. K. Sharma, "Matrix method for determining propagation characteristics of absorbing waveguides," Journal of Modern Optics **31**, 1041-1044 (1984).
87. H. Etzkorn and T. Heun, "Highly accurate numerical method for determination of propagation characteristics of dispersion-flattened fibres," Optical and Quantum Electronics **18**, 1-3 (1986).
88. A. Sharma and S. Banarjee, "Chromatic dispersion in single mode fibers with arbitrary index profiles: a simple method for exact numerical evaluation," Journal of Lightwave Technology **7**, 1919-1923 (1989).
89. A. W. Snyder and J. D. Love, *Optical wavguide theory* (Chapman Hall, New York, 1983).
90. G. Arfken, *Mathematical methods for physicists* (Academic Press, Orlando, FL, 1985).
91. L. Shen, S. He, and S. Xiao, "A finite-difference eigenvalue algorithm for calculating the band structure of a photonic crystal," Comp. Phys. Comm. **143**, 213-221 (2002).
92. C.-C. Su and C. H. Chen, "Calculation of propagation constants and cutoff frequencies of radially inhomogeneous optical fibers," IEEE Trans. Microwave Theory & Techniques **MTT-34**, 328-332 (1986).
93. G. R. Hadley, "Transparent boundary condition for the beam propagation method," IEEE Journal of Quantum Electronics **28**, 363-370 (1992).
94. S. Selleri, L. Vincetti, A. Cucinotta, and M. Zoboli, "Complex FEM Modal Solver of Optical Waveguides with PML Boundary Conditions," Optical and Quantum Electronics **33**, 359-371 (2001).
95. S. Guo, F. Wu, S. Albin, H. Tai, and R. Rogowski, "Loss and dispersion analysis of microstructured fibers by finite-difference method," OPTICS EXPRESS **12**, 3341-3352 (2004).
96. H. Rogier and D. D. Zutter, "Berengre and leaky modes in optical fibers terminated with a perfectly matched layer," J. Lightwave Technol. **20**, 1141-1148 (2002).
97. Y. Chen, R. Mittra, and P. Harmsz, "Finite difference time domain algorithm for solving Maxwell's equations in rotaionally symmetric geometries," IEEE Trans. Microwave Theory & Techniques **44**, 832-839 (1996).
98. D. W. Prather and S. Shi, "Formulation and application of the finite-difference time-domain method for the analysis of axially symmetric diffractive optical elements," J. Opt. Soc. Am. A **16**, 1131-1142 (1999).
99. D. E. Aspnes, "Local-field effects and effective-medium theory: A microscopic perspective," Am. J. Phys. **50**, 704-709 (1982).

100. H. Ikuno, "Guided modes of the Graded-index optical fiber with a parabolic-index core," in *Optical Waveguide Sciences, H. Huang (ed.) & A. W. Snyder (ed.)*, Martinus Nijhoff Publishers, The Hague, 1983, pp. 195-201.
101. M. Bassett and A. Argyros, "Elimination of polarization degeneracy in round waveguides," Opt. Express **10**, 1342-1346 (2002).
102. S. John, "Strong localization of photons in certain disordered dielectric superlattices," Physical Review Letters **58**, 2486-2489 (1987).
103. K. M. Ho, C. T. Chan, and C. M. Soukoulis, "Existence of a photonic gap in periodic dielectric structures," Physical Review Letters **65**, 3152-3155 (1990).
104. R. D. Meade, A. M. Rappe, K. D. Brommer, and J. D. Joannopoulos, "Accurate theoretical analysis of photonic band-gap materials," Physical Review B **48**, 8434-8437 (1993).
105. K. M. Leung and Y. F. Liu, "Full vector wave calculation of photonic band structures in FCC dielectric media," Physical Review Letters **65**, 2646-2649 (1990).
106. M. Qiu and S. He, "A nonorthogonal finite-difference time-domain method for computing the band structure of a two-dimensional photonic crystal with dielectric and metallic inclusions," Journal of Applied Physics **87**, 8268-8275 (2000).
107. C. T. Chan, Y. L. Yu, and K. M. Ho, "Order-N spectral method for electromagnetic waves," Physical Review B **51**, 16635-16642 (1995).
108. J. Arriaga, A. J. Ward, and J. B. Pendry, "Order-N photonic band structures for metals and other dispersive materials," Physical Review B **59**, 1874-1877 (1999).
109. A. J. Ward and J. B. Pendry, "Refraction and geometry in Maxwell's equations," Journal of Modern Optics **43**, 773-793 (1996).
110. A. J. Ward, http://www.sst.ph.ic.ac.uk/photonics/ONYX/orderN.html (10/10/2005).
111. S. Guo and S. Albin, "Simple plane wave implementation for photonic crystal calculations," Opt. Express **11**, 167-175 (2003).
112. S. Guo and S. Albin, "Numerical techniques for excitation and analysis of defect modes in photonic crystals," Optics Express **11**, 1080-1089 (2003).
113. M. Achtenhagen, R. J. Beeson, F. Pan, B. Nyman, and A. Hardy, "Gain and noise in Ytterbium-sensitized Erbium-doped fiber amplifiers: measurements and simulations," Journal of Lightwave Technology **19**, 1521-1526 (2001).
114. F. D. Pasquale, "Modeling of highly-efficient grating-feedback and Fabry-Perot Er^{3+}-Yb^{3+} co-doped fiber lasers," IEEE Journal of Quantum Electronics **32**, 326-332 (1996).
115. H. Soda, Y. Kotaki, H. Sudo, H. Ishikawa, S. Yamakoshi, and H. Imai, "Stability in single longitudinal mode operation in GaInAsP/InP phase-adjusted DFB lasers," IEEE Journal of Quantum Electronics **23**, 804-814 (1987).
116. W. H. Loh, B. N. Samson, and J. P. d. Sandro, "Intensity profile in a distributed feedback fiber laser charaterized by a green fluorescence scanning technique," Applied Physics Letters **69**, 3773-3775 (1996).
117. P. Zhou and G. S. Lee, "Chirped grating $\lambda/4$–shifted distributed feedback laser with uniform longitudinal field distribution," Electronics Letters **26**, 1660-1661 (1990).
118. P. Zhou and G. S. Lee, "Mode selection and spatial hole burning suppression of a chirped grating distributed feedback laser," Applied Physics Letters **56**, 1400-1402 (1990).

VITA

Feng Wu
ECE department, KH 231
Old Dominion University
Norfolk, VA 23529

Education:

- B. S. in Electrical Engineering, Northern Jiaotong University, Beijing 100044, China 1993
- M. S. in Electrical Engineering, Northern Jiaotong University, Beijing 100044, China, 1996
- Ph. D. in Electrical Engineering, Old Dominion University, USA, 2005

His main research interests are in theory and experiments on fiber optics, fiber fabrication, photonic devices, micro-optics, and electromagnetics. He has published several journal and conference papers related to fiber optics and photonics.

Selected journal publications from the dissertation:

1. F. Wu, S. Guo, K. Ikram, S. Albin, H. Tai, and R. S. Rogowski , "Numerical analysis of Bragg fibers using a compact 1D finite-difference frequency-domain method," Optics Communications 249, 165-174 (2005).
2. S. Guo, F. Wu, S. Albin, H. Tai, and R. S. Rogowski, "Loss and dispersion analysis of microstructured fibers by finite-difference method," Optics Express 12, 3341-3352 (2004).
3. S. Guo, F. Wu, S. Albin, and R. S. Rogowski, "Photonic band gap analysis using finite-difference frequency-domain method," Optics Express 12, 1741-1746 (2004).
4. S. Guo, F. Wu, K. Ikram, and S. Albin, "Analysis of circular fibers with an arbitrary index profile by the Galerkin method," Optics Letters 29, 32-34 (2004).